# Chapter One

# IR-VUV Photoionization Spectroscopy

## 1.1 Introduction

Vibrational spectroscopy provides one of the most definitive means of identifying the molecular species. The structures of hydrogen-bonded clusters and their intermolecular interactions may be readily studied with vibrational spectroscopy; because the stretching vibrational frequencies of N–H and O–H groups sensitively reflect the local intermolecular interactions due to microsolvation.[1–3] Recently, vibrational spectroscopy has also been used to derive information on the dynamics of molecular recognition.[4, 5]

Various vibrational spectroscopic techniques have been developed and used to study unstable molecules and clusters in the gas phase. The IR spectroscopy of clusters studied with direct IR absorption methods have been carried out using a Fourier-transform infrared (FTIR) spectrometry,[6, 7] a diode laser absorption spectrometer,[8] and a cavity ring-down laser absorption spectrometer.[9] Since clusters are usually generated with a distribution of sizes, without mass selection or a mass-specific measurement, observed vibrational spectra typically suffer from severe overlap among various clusters. Measurements performed direct IR absorption techniques with such techniques intrinsically lack size-selectivity, and thus are only applicable to small-sized clusters of which spectra have less overlap. Therefore, a methodology with size-selectivity is essentially important for IR spectral study of clusters.

The IR spectral studies of free radicals, that are typically highly reactive and short-lived,

also face similar problems. Since the radical of interest is generated typically from photolysis of a precursor that has a structure similar to the radical, the IR absorption spectrum of the radical obtained with direct IR absorption methods, such as matrix isolation [10] and time-resolved FTIR spectroscopy,[11] are often overlapped with the IR spectra of the precursor molecule or byproducts, making assignments challenging. Moreover, FTIR cannot be easily applied to jet-cooled radicals due to its low number density. A spectral technique with mass selection is highly desirable for IR spectrum of free radicals.

The photoionization technique with mass spectrometry is sensitive and the observed spectrum is mass-selective. IR spectra of mass selected species may be recorded using IR-depletion resonant two-photon ionization (IR-R2PI)[12–19] that was first demonstrated by Page, Shen, and Lee for the benzene monomer and dimer.[12] In this method, IR light is used to excite the vibrational modes of the ground state neutral molecule. The ions are prepared by the absorption of two UV photons involving a 1+1 resonance-enhanced mechanism. IR transitions are detected by monitoring the depletion of the two-photon ionization signal while scanning the IR frequency. Numerous systems involving aromatic rings have been investigated with this method because the aromatic moiety often gives a bound intermediate electronic state in the UV region which is usually long-lived and well characterized.[5, 12–16, 18, 20–22] This technique has also been applied to solvated clusters[13–15] and hydrogen-bonded molecular assemblies[5, 20–22] for the measurement of the IR spectrum in the N–H and O–H stretching regions. The highly reliable information on geometrical structures of clusters or molecular assemblies in their neutral ground state were obtained by recording their IR spectra and combining this with their quantum chemical calculations. Recent studies show the importance of X–H …π (X=N, O) hydrogen bonding interactions in molecular recognition.[18–21] Despite wide applications of this method, the IR-R2PI technique is limited only to some selected types of molecules because a long-lived intermediate electronic state accessible via UV excitation is

required. Molecules and their clusters such as alkyl halides, alcohols, amines, and ketones have dissociative electronic states in the UV region are unsuitable for this technique.

The ionization energies of a large number of molecules and their clusters are typically in the vacuum-ultraviolet (VUV) region.[23] The developments of VUV lasers[24 – 27] and synchrotron VUV light[28, 29] have induced revolutionary progress on molecular dynamics and VUV spectroscopy.[30–33] Unlike R2PI, direct VUV photon ionization eliminates the need of a suitable chromophore for electronic transition in UV or visible region to an intermediate state, making it applicable to most molecules. The VUV light source together with the tunable IR laser also allows the development of new methodology to investigate the vibrational spectrum of selected molecules. Recently, a combination of IR excitation and VUV photoionization with mass detection has been employed to investigate the vibrational spectrum of size-selected neutral molecules,[34–38] clusters,[39–42] and cations,[43–45] as discussed in recent review articles.[46, 47]

Although the frequency of VUV light from synchrotron radiation is easy to tune in full range, VUV lasers have narrower optical bandwidths. Moreover, the mismatch of the repetition rates of a typical IR laser (in the range of 1–10 kHz) and the pseudo-continuum VUV synchrotron radiation (in the MHz range) is an inefficient combination for IR-VUV study.[34, 48] As a result, the IR-VUV scheme using repetition rate matching IR and VUV lasers is considerably important.

In this thesis work, we employed the vacuum-ultraviolet-ionization detected-infrared predissociation and infrared-vacuum-ultraviolet-photoionization techniques to study the vibrational spectrum of size-selected neutral clusters and free radicals. A brief survey of the development of these techniques is given below.

## A. 1.2 Vacuum-Ultraviolet-Ionization Detected-Infrared Predissociation Spectroscopy (VUV-ID-IRPDS)

Mikami and his coworkers have shown that the VUV-ID-IRPDS detection scheme is a sensitive technique for IR spectroscopy of size-selected neutral clusters, as demonstrated in their studies of ammonia clusters and formamide (FA)–water clusters.[39, 40] The excitation scheme of VUV-ID-IRPDS is shown in Figure 1-1(a). In this scheme, VUV photon energy is set to be higher than the ionization threshold of the cluster under investigation to cause soft ionization typically without extensive fragmentation. The tunable IR light pulse is introduced prior to the VUV light pulse to dissociate the clusters. When the frequency of IR light matches the vibrational transition of the cluster, the vibrational dissociation induces depopulation of certain neutral clusters, which results to variations in ion signals in the TOF spectra. The IR spectra of clusters are obtained by tuning the IR laser wavelength and probing the intensities of ion signals induced by the VUV light and detected with TOF mass spectrometry. Bernstein and his coworkers termed this spectroscopic method as NRIFD-IR (nonresonant ionization and fragmentation detected infrared) spectroscopy,[41] but Mikami and his coworkers termed it as VUV-ID-IRPDS. They have employed this technique to investigate IR spectra of neutral clusters of various protic solvent molecules such as alcohols and organic acids by monitoring the changes in signal intensities of their fragment ions generated in the ionization process.[41, 45, 49, 50] However, because the predissociation mechanism might be complicated and the observed action spectrum does not necessarily reflect the IR spectrum, careful processing of the observed spectra is necessary to derive reliable IR spectra of each cluster, as demonstrated for methanol clusters.[42]

This ion-depletion method is suitable for IR spectroscopy of weakly bond clusters but unsuitable for neutral molecules and clusters which do not dissociate upon vibrational

excitation.

### 1.3 IR-VUV Photoionization Spectroscopy (IR-VUV-PI)

The two color IR-VUV photoionization detection scheme was first developed by Ng and his coworkers.[51] They have performed the IR-VUV-PI technique for IR spectra of neutral molecules such as trichloroethane, ammonia, and propyne.[51–53] Figure 1-1(b) shows the excitation scheme, in which the VUV photon energy is set to be slightly less than the ionization threshold of the species of interest and the IR laser frequency is tuned to excite the rovibrational levels of the molecules. When the IR frequency matches an IR transition, the molecule of interest is ionized with the 1+1 IR-VUV photoionization scheme, hence, the enhanced intensity of the ion signal may be observed. The IR-VUV-photoionization (IR-VUV-PI) spectrum is obtained by scanning the frequency of the IR light while probing the enhanced intensity of the ion signal upon additional IR irradiation. This excitation scheme provides a good measure of the IR spectra for the neutral molecules, radicals, and clusters which do not dissociate by vibrational excitation. Since the ion background due to direct photoionization is negligible in the IR-VUV-PI measurement, the nearly ‘background-free’ feature results in a high sensitivity for IR-VUV-PI measurements. Ng and coworkers have also developed a spectral method of using the IR-VUV scheme with the pulsed field ionization-photoelectron technique (PFI-PE). The vibrational levels of neutral and cationic molecules and the state-selected and state-to-state photoionization cross sections of several polyatomic molecules are obtained by IR-VUV-PIE and IR-VUV-PFI-PE measurements.[47, 51–57]

Technically, the lifetime of the excited intermediate state should be long enough to make two-color photoionization measurements. The IR-VUV photoionization scheme involves first

preparing the neutral molecule in an excited rovibrational state with the IR excitation prior to VUV photoionization. The radiative lifetimes of most vibrationally excited states are expected to be longer than 1 μs, while the intramolecular vibrational energy redistribution (IVR) lifetimes are expected to be shorter than 1 ns. However, it is well known that the IVR lifetime is generally long for many small molecules and longer than 0.1 μs for low lying rovibrational states due to lower density of states. The advantage of having a long lifetime for rovibrationally excited states makes the 1+1 IR-VUV photoionization feasible.

IR-VUV photoionization technique has a significant advantage over the IR-R2PI scheme, which essentially needs a well-characterized and long-lived intermediate electronic state, and thus the technique is generally applicable to all molecules. The IR-VUV-PI technique also has some unique advantages over other spectral techniques.[58] First, it can yield a larger Franck–Condon factor (FCF) for the formation of the ion of interest. Since the photoionization process usually begins with a molecule in its ground vibrational state, the intensity of the photoion signal observed in photoion spectrum and the intensity of an excited ion vibrational band observed in the photoelectron spectrum are proportional to the FCF between the ground state of the neutral and the excited vibrational state of the ion. The FCF is negligible if the removal of the photoelectron only has a small effect on the bonding property of the atoms comprising the vibrational motion. On the contrary, the FCF is significant appreciable if the ejection of a photoelectron would strongly perturb the vibrational motion. However, excited vibrational states of ions which are difficult to be excited directly by single-photon VUV ionization due to small FCF may be examined using a two-color IR-VUV photoionization scheme. By preparing the neutral molecule in a suitable vibrational state using IR laser prior to ionizing molecule with VUV ionization, the photoionization transition might be shifted to a region which gives a larger FCF for the formation of the excited state of ions of interest. Second, the IR-VUV-PI technique can yield accurate ionization energy through reduction of the hot

bands effect. In determination of the ionization energy of a molecule, the thermal excitations of rotational and low-frequency vibrational modes usually interfere the measurements and limit the precision of measured *IE* values. The (1+1) IR-VUV photoionization is a double resonance technique which produces additional state selectivity. For some cases, the double resonance made by obtaining a specific rovibrational state by IR excitation prior to VUV photoionization might be an ideal method to eliminate the hot band problem in *IE* measurements. Moreover, when the geometries of the neutral molecule and its ion are similar, the FCF for producing the ground state ion might be small, resulting in difficulties in obtaining a reliable *IE* value from the photoion spectrum. This problem may become less severe by increasing the FCF for the formation of the ground state ion using the IR-VUV photoionization scheme. Thus, this method will enhance the accuracy in the measurements of *IE*. Furthermore, the (1+1) IR-VUV scheme is governed by optical selection rules that might be different from those for single-photon photoionization and IR-R2PI schemes which are governed by the selection rules of one and three photons excitations, respectively. Some vibrational states of ions that cannot be examined by single-photon photoionization and IR-R2PI may be studied with the IR-VUV photoionization method.

By using the broadly tunable infrared optical parametric oscillator laser and vacuum ultraviolet laser systems we employs VUV-ID-IRPD and IR-VUV-PI techniques to obtain IR spectra of methanol clusters and $CH_3S$ radical, respectively. Chapter 2 describes the experimental setups. Chapter 3 presents the VUV-ID-IRPD study of methanol clusters. Chapter 4 reports IR spectrum of mass-selected $CH_3S$ radicals in the range 2790–3270 $cm^{-1}$, investigated with IR-VUV photoionization method.

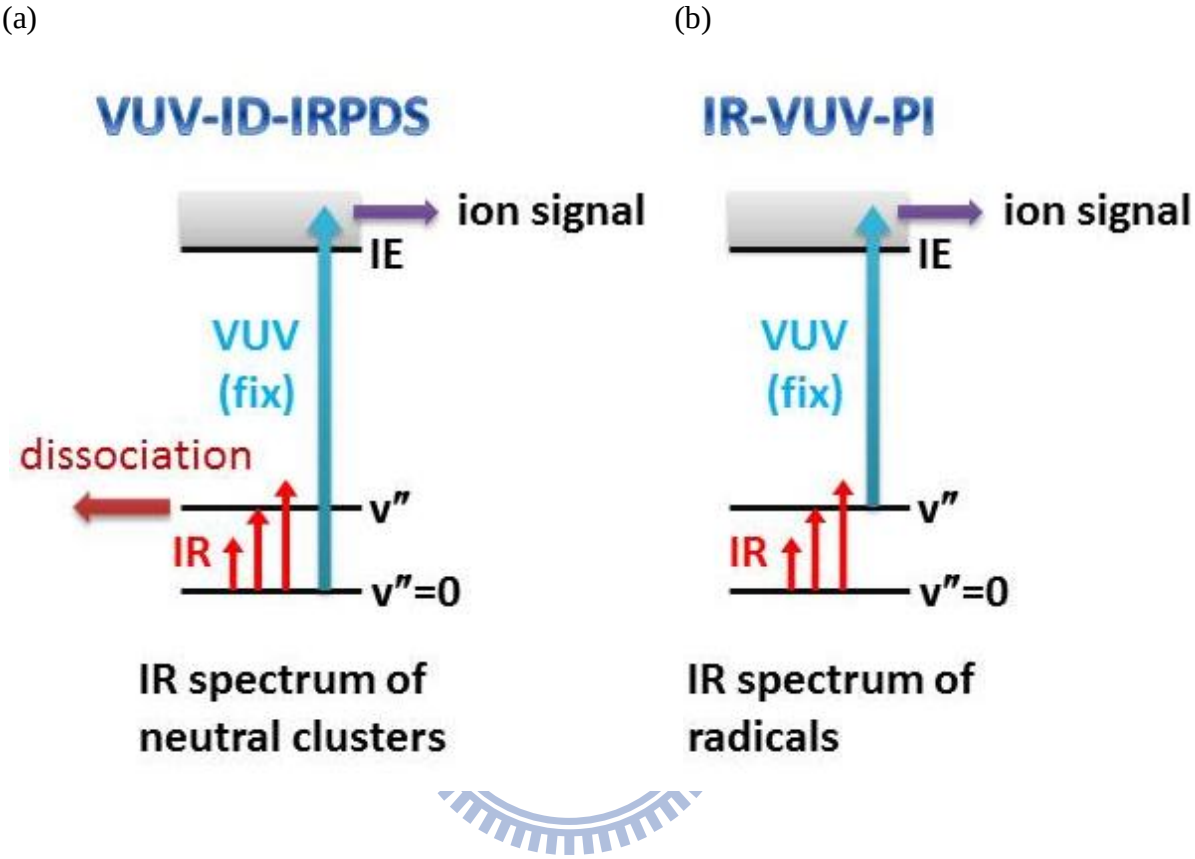


Figure 1-1 Two excitation schemes for IR-VUV ionization. (a) VUV-ionization detected-IR predissociation spectroscopy (VUV-ID-IRPDS). (b) IR-VUV photoionization spectroscopy (IR-VUV-PI).

**References**

[1] T. S. Zwier, Annu. Rev. Phys. Chem. **47**, 205 (1996).

[2] J. J. Scherer, J. B. Paul, A. O'Keefe, and R. J. Saykally, Chem. Rev. **97**, 25 (1997).

[3] W. H. Robertson and M. A. Johnson, Annu. Rev. Phys. Chem. **54**, 173 (2003).

[4] T. Scharge, C. Cézard, P. Zielke, A. Schütz, C. Emmeluth, and M. A. Suhm, Phys. Chem. Chem. Phys**. 9**, 4521 (2007).

[5] E. Gloaguen, F. Pagliarulo, V. Brenner, W. Chin, F. Piuzzi, B. Tardivel, and M. Mons, Phys. Chem. Chem. Phys**. 9**, 4491 (2007).

[6] T. Häber, U. Schmitt, and Martin A. Suhm, Phys. Chem. Chem. Phys. **1**, 5573 (1999).

[7] S. Coussan, A. Loutellier, J.P. Perchard, S. Racine, A. Perernans, A. Tadjeddine, and W.Q. Zheng, Chem. Phys. **223,** 279 (1997).

[8] G. Winnewisser, T. Drascher, T. Giesen, I. Pak, F. Schmülling, and R. Schieder, Spectrochim. Acta, Part A **55**, 2121 (1999).

[9] J. B. Paul, C. P. Collier, and R. J. Saykally , J. Phys. Chem. A **101**, 5211 (1997).

[10] M. Bahou and Y.-P. Lee, J. Chem. Phys. **133**, 164316 (2010).

[11] L.-K. Chu and Yuan-Pern Lee, J. Chem. Phys. **133**, 184303 (2010).

[12] P. H. Page, Y.-R. Shen, and Y. T. Lee, J. Chem. Phys. **88,** 4621 (1988).

[13] R. N. Pribble and T. S. Zwier, Science **265**, 75 (1994).

[14] T. Ebata, A. Fujii, and N. Mikami, Int. Rev. Phys. Chem. **17**, 331 (1998).

[15] T. S. Zwier, Annu. Rev. Phys. Chem. **47**, 205 (1996).

[16] B. Brutschy, Chem. Rev. **100**, 3891 (2000).

[17] L. Feng, Jie. Wei, and H. Reidter, J. Phys. Chem. A **108**, 7903 (2004).

[18] E. C. Stanca-Kaposta, D. P. Gamblin, J. Screen, B. Liu, L. C. Snoek, B. G. Davis, and J. P. Simons, Phys. Chem. Chem. Phys. **9**, 4444 (2007).

[19] M. Gerhards and C. Unterberg, Appl. Phys. A **72**, 273 (2001).

[20] H. Fricke, G. Schäfer, T. Schrader, and M. Gerhards, Phys. Chem. Chem. Phys.**9**, 4592 (2007).

[21] K. Bartl, A. Funk, and M. Gerhards, J. Chem. Phys. **129**, 234306 (2008).

[22] R. Brause, H. Fricke, M. Gerhards, R. Weinkauf, K. Kleinermanns, Chem. Phys. **327**, 43 (2006).

[23] S. G. Lias, J. E. Bartmess, J. F. Liebman, J. L. Holmes, R. D. Levin, and W. G. Mallard, J.

Phys. Chem. Ref. Data **17**, Suppl. 1 (1988).

[24] E. Cromwell, T. Trickl, Y. T. Lee, and A. H. Kung, Rev. Sci. Instrum. **60**, 2888 (1989).

[25] A. H. Kung, Y. T. Lee, in: C.Y. Ng (Ed.), Vacuum Ultraviolet Photoionization and Photodissociation of Molecules and Clusters, World Scientific, Singapore, 1991, p. 487.

[26] J. W. Hepburn, in: C. Y. Ng (Ed.), Vacuum Ultraviolet Photoionization and Photodissociation of Molecules and Clusters, World Scientific, Singapore, 1991, p. 435.

[27] U. Hollenstein, H. Palm, and F. Merkt, Rev. Sci. Instrum. **71,** 4023 (2000).

[28] P. Heimann, M. Koike, C.-W. Hsu, M. Evans, K. T. Lu, C. Y. Ng, A. Suits, and Y. T. Lee, Rev. Sci. Instrum. **68**, 1945 (1997).

[29] G. K. Jarvis, Y. song, and C. Y. Ng, J. Chem. Phys. **111**, 1937 (1999).

[30] I. Poweis, T. Baer, and C. Y. Ng (Eds.), High resolution laser photoionization and photoelectron studies, Adv. Ser. Phys. Chem., vol. 10A , World Scientific, Singapore, 1995, p. 600.

[31] C. Y. Ng, Annu. Rev. Phys. Chem. **53**, 101 (2002).

[32] X. Hong, L. Zhang, T. Zhang, and F. Qi, J. Phys. Chem. A **113**, 5397 (2009).

[33] F. Battin-Leclerc, O. Herbinet, P.-A. Glaude, R. Fournet, Z. Zhou, L. Deng, H. Guo, M. Xie, and F. Qi, Angew. Chem. Int. Ed. **49**, 3169 (2010).

[34] X.-M. Qian, A. H. Kung, T. Zhang, K.-C. Lau, and C. Y. Ng, Phy. Rev. Lett. **91**, 233001 (2003).

[35] P. Wang, X. Xing, K.-C. Lau, H. K. Woo, and C. Y. Ng, J. Chem. Phys. **121**, 7049 (2004).

[36] X. Xing, B. Reed, M. K. Bahng, P. Wang, H. K. Woo, S. J. Baek, C. S. Lam, and C. Y. Ng, Chin. J. Chem. Phys. **21**, 193 (2008).

[37] H. K. Woo, P. Wang, K.-C. Lau, X. Xing, C. Chang, and C. Y. Ng, J. Chem. Phys. **119**, 9333 (2003).

[38] M.-K. Bahng, X. Xing, S. J. Baek, and C. Y. Ng, J. Chem. Phys. **123**, 084311 (2005).

[39] Y. Matsuda, M. Mori, M. Hachiya, A. Fujii, and N. Mikami, Chem. Phys. Lett. **422**, 378 (2006).

[40] D. Sakai, Y. Matsuda, M. Hachiya, and M. Mori, J. Phys. Chem. A **112**, 6840 (2008).

[41] H. B. Fu, Y. J. Hu, and E. R. Bernstein, J. Chem. Phys. **124**, 024302 (2006).

[42] H.-L. Han, C. Camacho, H. A. Witek, and Y.-P. Lee, J. Chem. Phys. **134**, 144309 (2011).

[43] X. Xing, B. Reed, M.-K. Bahng, and C. Y. Ng, J. Phys. Chem. A **112**, 2572 (2008).

[44] X. Xing, M.-K. Bahng, B. Reed, C. S. Lam, K.-C. Lau, and C. Y. Ng, J. Chem. Phys. **128**, 094311 (2008).

[45] Y. J. Hu, H. B. Fu, and E. R. Bernstein, J. Chem. Phys. **125**, 154305 (2006).

[46] Y. Matsuda, N. Mikami, and A. Fujii, Phys. Chem. Chem. Phys. **11**, 1279 (2009).

[47] C. Y. Ng, Spectroscopy and Dynamics of Neutrals and Ions by high-resolution infrared-vacuum ultraviolet photoionization and photoelectron methods, in Frontiers of Molecular Spectroscopy, edited by Jaan Laane (Elsvier Science and Technology, 2009) Chap. 19, p. 659.

[48] X. -M. Qian, T. Zhang, C. Y. Ng, A. H. Kung, and M. Ahmed, Rev. Sci. Instrum. **74**, 2784 (2003).

[49] Y. J. Hu, H. B. Fu, and E. R. Bernstein, J. Chem. Phys. **125**, 154306 (2006).

[50] Y. J. Hu, H. B. Fu, and E. R. Bernstein, J. Chem. Phys. **125**, 184308 (2006).

[51] H. K. Woo, P. Wang, K.-C. Lau, X. Xing, C. Chang, and C. Y. Ng, J. Chem. Phys. **119**, 9333 (2003).

[52] M.-K. Bahng, X. Xing, S. J. Baek, and C. Y. Ng, J. Chem. Phys. **123**, 84311 (2005).

[53] X. Xing, B. Reed, K. C. Lau, S. J. Baek, M. K. Bahng, and C. Y. Ng, J. Chem. Phys **127**, 044313 (2007).

[54] X. -M. Qian, A. H. Kung, T. Zhang, K. C. Lau, and C. Y. Ng, Phy. Rev. Lett. **422**, 378 (2006).

[55] H. K. Woo, P. Wang, K.-C. Lau, X. Xing, and C. Y. Ng, J. Chem. Phys. **120**, 1756, (2004).

[56] M.-K. Bahng, X. Xing, S. J. Baek, X. Qian, and C. Y. Ng, J. Phys. Chem. A **110**, 8488 (2006).

[57] X. Xing, M.-K. Bahng, B. Reed, C. S. Lam, K.-C. Lau, and C. Y. Ng, J. Chem. Phys. **128**, 094311 (2008).

[58] C. Y. Ng, J. Electron Spectrosc. Rel. Phenom. **142**, 179 (2005).

# Chapter Two

# IR-VUV Photoionization Experiments

## 2.1 Introduction

My experiments involving IR-ID-IRPD and IR-VUV PI for vibrational spectral investigation of size-selected neutral clusters and molecules are described herein.

### B. 2.1.1 VUV-Ionization Detected-IR Predissociation (VUV-ID-IRPD)

The excitation scheme for VUV-ID-IRPDS is described in Figure 1-1(a). According to this scheme, with the energy of VUV photons set slightly greater than the threshold for ionization of the cluster of interest, the neutral cluster might be softly ionized without fragmentation, IR depletion of ion signal which is correlated to the cluster of interest occurs when the cluster absorb IR light.

The arrangement of equipment for this experiment is illustrated in Figure 2-1. In my experiments, I used VUV laser light at wavelength 118 nm. The produced cluster ions were detected with a linear time-of-flight (TOF) mass spectrometer. If the photoionization efficiencies of pertinent clusters of varied size were similar, the observed distribution of the signal from ions of the parent mass channel might have represented the relative population of the neutral parent clusters. The pulse of tunable IR light was introduced several hundred ns to several μs before the VUV light pulse to predissociate the clusters. Figure 2-1(a) depicts the

alignment of IR and UV laser beams at the position of the ionization region. When the frequency of IR light matched that of a vibrational transition of a cluster, the vibrational predissociation induced a depopulation of neutral clusters; in a varied intensity of the ion signal that was induced with VUV light. On monitoring the intensity of each ion signal while scanning the wavenumber of the IR laser, I recorded the variation of the relative population of each ion, called the action spectrum. On processing the action spectra according to photoionization efficiencies and the mechanism of the production and loss of each cluster, I obtained the IR spectrum of a size-selected cluster.

### 2.1.2 IR-VUV Photoionization (IR-VUV PI)

The excitation scheme to generate IR-VUV-PI spectra is described in Figure 1-1(b). According to this excitation scheme, the VUV photon energy was set less than the ionization threshold of the molecule, and the frequency of the tunable IR laser was tuned to excite the vibrational bands of the molecules. The molecule cation of interest was formed only if it absorbed both IR and VUV radiation with the 1+1 IR-VUV photoionization.

The experiment of IR-VUV-PI in Figure 2-2 is similar to that of VUV-ID-IRPDS, except that the coherent VUV light is generated through resonance-enhanced four-wave difference-frequency mixing in a cell containing gaseous Kr and Ar, to obtain the tunable VUV light. The tunable IR light pulse was introduced 30–100 ns before the VUV light pulse The IR-VUV-PI signal was governed mostly by the Franck-Condon factors of the vibrationally excited states and the transition dipolar moment of the excited vibrational modes of the molecules. On monitoring the ion signal while scanning the frequency of the IR laser, I hence recorded the IR absorption spectrum of a neutral molecule via (1+1) IR-VUV multiphoton ionization.

## 2.2 The Basic Concepts and Details of Construction of Experiments

The photoionization apparatus depicted in Figure 2-1 and Figure 2-2 consisted of a pulsed VUV laser, a pulsed IR laser, a photolysis laser, a pulsed molecular-beam source and a time-of-flight (TOF) mass spectrometer to detect ions. In the following sections, the basic concepts and details of construction of the VUV laser, the OPO/OPA IR laser, the TOF mass spectrometer, and the system for data acquisition are introduced.

### 2.2.1 Light Sources

**Coherent VUV Laser Radiation**

#### 2.2.1.1 VUV Radiation at 118 nm From Nonresonant Third-Harmonic Generation

**(1) Theory**

Theories and experiments of third-harmonic generation in noble gases are described elsewhere.[1–5] In summary, when an incident beam is focused into a cell containing a nonlinear medium for frequency conversion, a third-harmonic beam is generated collinearly. Figure 2-3(a) illustrates a schematic diagram for third-harmonic generation, such that $\omega_1 = \omega_2 = \omega_3 = \omega$ and $\omega_{VUV} = \omega_1 + \omega_2 + \omega_3 = 3\omega$. When a Gaussian beam of frequency ω with intensity less than $10^{14}$ W cm$^{-2}$ is focused into an atomic medium, the power $P_{VUV}$ of the generated third-harmonic output is expressed as

$$P_{VUV} \propto N^2 \left|\chi^{(3)}\right|^2 P_\omega^3 F(b\Delta k) \qquad (1)$$

in which N is the number density of the nonlinear medium, $P_\omega$ is the power of an incident beam, $\chi^{(3)}$ is the third-order susceptibility induced with an intense field in a medium through a nonlinear optical effect, and $F(b\Delta k)$ is the geometric phase-matching factor that is a function of a product of the confocal parameter b and the wavevector mismatch $\Delta k$. In Eq. (1), $\chi^{(3)}$ that governs the efficiency of frequency conversion with a given pump intensity is expressed as

$$\chi^{(3)}(\omega_{VUV}=3\omega)=\frac{6N}{h^3}\sum_{a,b,c}\frac{\mu_{ga}\mu_{ab}\mu_{bc}\mu_{cg}}{(\omega_{ag}-\omega)(\omega_{bg}-2\omega)(\omega_{cg}-3\omega)} \tag{2}$$

in which $\mu_{ij}$ denotes an electric-dipole matrix element for the transition between an electronically excited state '*i*' and electronic ground state '*j*', $|i\rangle \leftarrow |j\rangle$. $\omega_{ig}$ is the complex transition frequency given by $\omega_{ig}=\Omega_{ig}+i\Gamma_{ig}$ in which $\Omega_{ig}$ is the frequency difference between unperturbed states '*i*' and '*j*', $\Gamma_{ig}$ is the damping parameter and $\omega$ is the frequency of incident light. Under a tightly focused condition, phase-matching factor $F(b\Delta k)$ is defined as[1]

$$\begin{aligned} F(b\Delta k) &= \pi^2(b\Delta k)^2\exp(b\Delta k/2) \qquad (\Delta k<0) \\ &= 0 \qquad\qquad\qquad\qquad\quad (\Delta k\geq 0) \end{aligned} \tag{3}$$

In Eq. (3), $\Delta k = k_{3\omega}-3k_\omega = \frac{2\pi n_{\lambda_{3\omega}}}{\lambda_{3\omega}}-\frac{2\pi n_{\lambda_\omega}}{\lambda_\omega}$, and *b* is the confocal parameter, defined as

$$b=2\pi w_0^2/\lambda=2\pi w_0^2 n/\lambda_0 \tag{4}$$

in which $w_0=\left(f\lambda/\pi w_1\right)$ is the radius of the beam waist, $f$ is the focal length, $w_1$ is the spot size on the lens, $\lambda$ is the wave length in the nonlinear medium, *n* is the index of refraction and $\lambda_0$ is the vacuum wavelength. Under a tightly focused condition, *b* << length *L* of the gas cell;

i.e., the entire focal region is contained within the cell. According to Eq. (3), $F(b\Delta k)$ is non-zero only when $\Delta k$ is negative, i.e., the refractive index at the third harmonic wavelength is less than one third the refractive index at the fundamental frequency. This third harmonic generation scheme is hence applicable only when the condition $\Delta k < 0$ for negative dispersion is satisfied. Negative dispersion is also essential to compensate for the phase slip that occurs between fundamental and harmonic beams at the focal point. Because regions of negative dispersion occur on the small-wavelength side of resonant spectral lines, the negative dispersion is obtained on allowing the third-harmonic frequency to be greater than, but near, the frequency of a transition; third-harmonic generation is therefore possible only in specific intervals of wave length for a given gas. In this work, the 5*p*-5*d* transition of Xe at 119.2 nm is the dominant transition.

To generate intense VUV light, $P_\omega$, $F(b\Delta k)$ and $N$ must be optimized at a given wavelength. $\left|\chi^{(3)}\right|^2$, determined by the wavenumber of incident laser light and the gas to generate the third harmonic, is essentially a constant. The dependence of power and number density on $\chi^{(3)}$ has been demonstrated by Kung[6] and Shi et al.[7] The upper limit of $P_\omega$ determined by the an irradiance of a monochromatic light is approximately $10^{12}$ W cm$^{-2}$ at the focal point.[8] According to Eq. (3), function $F(b\Delta k)$ is a maximum when $b\Delta k = -4$. In a fixed optical system, confocal parameter $b$ is fixed; $F(b\Delta k)$ becomes optimized on adjusting $\Delta k$. Because $\Delta k$ is the product of the wavevector mismatch per atom and the number density of the gas, the optimized condition can be achieved on adjusting the pressure of the non-linear medium or by adding a positively dispersive buffer gas in some proportion to a negatively dispersive third-harmonic medium. Optimization of $\Delta k$ through adjustment of the pressure of the third-harmonic gas is easier; the efficiency of conversion is small, but, when a positively dispersive gas is used to adjust $\Delta k$, $N$ increases, whereas the positively dispersive gas

compensates the excess negative dispersion. Even though this method is more complicated, it has the advantage that both $F(b\Delta k)$ and $N$ are optimized.

For third-harmonic generation with Xe, conversion efficiencies ≈ $10^{-5}$–$10^{-6}$ providing an intense coherent VUV output are typically obtained with a commercial ns pulsed dye laser having peak power 0.1–4 MW.[9] The VUV energy does not increase with monotonically increasing pressure of Xe and power of UV light. At increased Xe pressure, the absorption by dimers ($Xe_2$ and XeAr) begins to diminish the effective VUV power. As the laser power or the confocal parameter is increased, breakdown might occur, which could greatly diminish or eliminate the VUV power.

Table 2-1 summarizes the optimum pressures and conversion efficiencies for third-harmonic generation at several wavelengths in the range 118–129 nm with ns laser pulses.[4] For example, to obtain the greatest efficiency of energy conversion for the generation of radiation at 118.2 nm in a mixture of Xe (negatively dispersive gas) and Ar (positively dispersive gas) with input light at 354.7 nm, the Ar pressure was adjusted to achieve the phase-matching condition $n_{Xe}(\omega) + n_{Ar}(\omega) = n_{Xe}(3\omega) + n_{Ar}(3\omega)$. Figure 2-4 shows the dependence of VUV output power on the pressure of Ar in an unfocused geometry.[9] The pressure of Xe was fixed at 71 Torr. The maximum third harmonic power was obtained at a ratio Ar : Xe =10.25:1.

**(2) Experiment**

The experimental apparatus used to generate VUV at 118 nm is shown in Figure 2-1. The output of a Nd:YAG laser (Spectra Physics, GCR-230, 10 Hz, ~25 mJ $pulse^{-1}$) at 355 nm was focused onto a gas cell containing a mixture of Xe and Ar (1:10) to yield radiation at 118 nm. The pressure of the mixture was adjusted, to about 80 Torr to attain the maximum power of

VUV radiation. The gas cell was attached directly to the ion-source chamber of the time-of-flight mass spectrometer. The UV beam (wavelength 355 nm) was aligned with two S1UV prisms and two dichroic mirrors, and focused into the frequency-conversion cell with a S1UV lens ($f$ = 50 cm). The frequency-conversion cell is cylindrical and composed of a stainless steel pipe of length 300 mm, diameter 38.1 mm and wall thickness 1.65 mm. The front of the frequency-conversion cell was equipped with a S1UV entrance window. A convex lens ($MgF_2$, $f$ = 150 mm) was mounted at the end of the gas cell to separate the UV (355 nm) and VUV (118 nm) light according to the difference in the refraction index $n$ of the lens; $n$ (118 nm) ≅ 1.679 and $n$ (355 nm) ≅ 1.380.[10] To minimize the multiphoton ionization effects due to the intense beam at 355 nm, the UV and VUV beams were separated ~5 mm horizontally in the ionization region. After passing the photoionization region, the intensity of the VUV beam was measured with a photoelectric detector (copper) for spectrum normalization; the VUV photons struck the surface of the copper plate, creating photoelectrons, which were collected with a surrounding electrode, thus generating a current.

#### 2.2.1.2 Tunable VUV Radiation Generated With Resonant Four-Wave Mixing

**(1) Theory**

Tunable coherent light in the VUV wavelength region, between 200 and 70 nm, is generated with two-photon resonance four-wave sum- or difference-frequency mixing, with various gas media such as noble gases (Ne, Ar, Kr, Xe)[11–15] and metal vapor (Sr, Mg, Hg).[16– 18] In review articles Hilbig *et al.*[19], Jamroz and Stoicheff[17] and Yamanouchi and Tsuchiya[20] presented a comprehensive overview of four-wave sum and difference techniques. In the resonant four-wave mixing process schematically illustrated in Figure 2-3(b), the interaction

of two intense laser beams with the nonlinear medium gives rise to the generation of light with higher or lower frequencies when focused into the nonlinear medium. For two-photon resonant four-wave sum- and difference-frequency mixing is the wavenumber of laser light locked to the two-photon resonance level of the nonlinear medium and $\omega_2$ is the second tunable laser light, which is varied to attain frequency tunability such that $\omega_{VUV} = 2\omega_1 \pm \omega_2$, $\omega_1$. According to Eq. (1), when one of the following conditions $\omega = \omega_{ag}$ (one-photon resonance), or $2\omega = \omega_{bg}$ (two-photon resonance), or $3\omega = \omega_{cg}$ (three-photon resonance) is satisfied, the denominators of the Eq. (1) tend to be zero so that the value of the susceptibility becomes enhanced. Resonance four-wave mixing is known to improve the efficiency of VUV generation by a factor $10^2$–$10^4$ relative to those of THG.[19] In the Kr cell, with 4*p*–5*p*[5/2, 2] transition at 212.6 nm, efficiencies $10^{-4}$ have been achieved for input power of a few hundred kilowatts.[21]

According to conditions that the fundamental linearly polarized beams at $\omega_1$ and $\omega_2$ are the lowest order Gaussian modes that propagate concentrically along axis *z* with identical waist locations and identical confocal beam parameters, the driving power of the generated VUV light is given by

$$P_{VUV} \propto N^2 \left|\chi^{(3)}\right|^2 P_{\omega 1}^2 P_{\omega 2} F(b\Delta k) \tag{5}$$

in which $P_{\omega 1}$ and $P_{\omega 2}$ are the power of incident laser beams at wavenumbers $\omega_1$ and $\omega_2$, respectively, $\Delta k$ is the wavevector mismatch, defined as $\Delta k = k_{VUV} - (2k_1 + k_2)$ or $\Delta k = k_{VUV} - (2k_1 - k_2)$ for a sum or difference frequency scheme, respectively. In the tight focusing limit in which *b* is much less than length *L* of a cell, *b*/*L*≅0; the entire focal region is contained within the cell, i.e. $b \le f \le L - b$. For the sum frequency scheme, in the case *f*/*L*=0.5, the phase-matching factor $F_{sum}(b\Delta k)$ is given by[2]

$$F_{sum}(b\Delta k) = \pi^2 (b\Delta k)^2 \exp(b\Delta k/2) \qquad (\Delta k < 0)$$
$$= 0 \qquad (\Delta k \geq 0) \tag{6}$$

For a difference-frequency scheme, in the tight focusing limit and when $k' = k_{VUV} - \Delta k = k'' = 2k_1 + k_2$, the phase-matching factor $F_{diff}(b\Delta k)$ is given by

$$F_{diff}(b\Delta k) = \pi^2 \exp(-b|\Delta k|) \tag{7}$$

Figure 2-5 shows plots of phase-matching factors $F(b\Delta k)$ as a function of $b\Delta k$ for $b/L$ =0 and 0.1, $f/L$ =0.5, in the sum- and difference-frequency schemes. According to Eq. (6), the four-wave sum frequency mixing has a limited tunability for the VUV radiation because of narrow phase-matching conditions; the maximum of $F_{sum}(b\Delta k)$ occurs at $b\Delta k = -4$ as shown in Figure 2-5(a). The four-wave difference mixing can be generated for both negative and positive dispersion as shown in Figure 2-5(b); the maximum of $F_{diff}(b\Delta k)$ occurs at $\Delta k = 0$. Difference-frequency mixing hence provides the most efficient tunable VUV output; the intensity is maximized at the phase-matched condition, but the phase slip due to focusing might be compensated to some extent by the wave-vector mismatch $\Delta k$ introduced by the dispersion of the nonlinear medium at frequencies $\omega_1$, $\omega_2$, and $\omega_{VUV}$. The optimum value of $\Delta k$, $\Delta k_{OPT}$, is defined as the value that cancels the total phase slip that occurs in the generation region. In the tight-focusing condition, $\Delta k_{OPT}$ is given by

$$\Delta k_{OPT} \cong \begin{cases} -2.2/b, & \text{for } 2\omega_1 + \omega_2 \rightarrow \omega_{VUV} \\ 0, & \text{for } 2\omega_1 - \omega_2 \rightarrow \omega_{VUV} \end{cases} \tag{8}$$

The maximum conditions for phase-matching factors under tight-focusing conditions are $b\Delta k_{OPT} = -2.2$ for the sum- frequency scheme, and $b\Delta k_{OPT} = 0$ for the difference-frequency scheme. Parameter $b\Delta k$ is adjusted to $b\Delta k_{OPT}$ on modifying $b$ or $\Delta k$. The value of $b$ is directly altered on varying the tightness of the focus, and $b/L$ must remain less than 0.1 to

match the requirement of the tight-focusing condition. Optimization through adjustment of $b$ is valid only if the nonlinear medium can tolerate the great power density caused by tight focusing. The value of $\Delta k$ is controlled on varying the pressure of the gas or on adding a positively dispersive buffer gas (such as Ar) into the cell[2, 22]. Optimizing $\Delta k$ by adding a buffer is considered to be an easier method to attain $b\Delta k_{\mathrm{OPT}}$.

Figure 2-6 shows diagrams of the energy levels of relevant atomic non-linear media such as Hg, Kr, Xe, Ar to generate coherent VUV light. The wavelength regions in the sum- and difference-frequency schemes are also shown. Figure 2-7 shows the broad tunability of the VUV light in the range 127–180 nm generated with difference-frequency conversion in Kr, in which $\omega_1$ (at 216.6 nm) is resonant with Kr two-photon transition 4*p*-5*p* [5/2, 2], $\omega_2$ is in the range 219–737 nm produced with various laser dyes (Ref. 14). The VUV output power is plotted in arbitrary units. For ease of recording, the pressure of the Kr gas was adjusted for optimum VUV output; the tuning curves are not displayed on the same scale. There are several significant dips in the VUV output power in some tuning curves; these dips occur when $\omega_2$ coincides with an autoionizing Rydberg state enhancing the two-photon resonant four-wave mixing.[20] For use of the 4*p*–5*p* [1/2, 0] two-photon resonance at 212.55 nm ($\omega_1$), and with gaseous Ar added for phase-matching, the greatest efficiency 0.05 of conversion was achieved.[23] The optimum phase matching occurs for pressure ratio $P_{Ar}/P_{Kr}$ = 3.0. The measured enhancement factor, which is the ratio of the optimum intensity obtainable with the phase-matched mixture to the optimum intensity obtained with Kr alone, is 100.

**(2) Experiment**

Figure 2-8 shows a schematic diagram of the experiment to generate tunable VUV light,

with resonance-enhanced four-wave difference-frequency mixing ($\omega_{VUV} = 2\omega_1 - \omega_2$) in a Kr gas cell for transition Kr $4P^6\,(^1S_0) \rightarrow 4P^5(^2P^0{}_{3/2})5P\,(^2[1/2]_0)$ at 94,092.86 $cm^{-1}$ ($= 2\omega_1$).[24] A gas cell containing Kr and Ar in a mixture (1:3 at total pressure 50 Torr) was used to generate VUV light. UV frequency $\omega_1$ was fixed at 47,046.43 $cm^{-1}$ (= 212.556 nm) to match the two-photon resonance of Kr 4P→5P transition. Light at this wavelength 212.556 nm (horizontally polarized) was generated from vertically polarized output at 425.112 nm of a dye laser (Scanmate, Lambda Physik, bandwidth = 0.70 $cm^{-1}$) passing a β-barium borate crystal (BBO, type 1, Castech, crystal no: 2-43203-0001), creating frequency doubling. The dye laser was pumped with vertical polarized output of a Nd:YAG laser (GCR-230, Spectra Physics, 125 mJ, 355 nm, 10 Hz). The BBO crystal was mounted on a motorized rotary stage (SGSP-60YAW, Sigma Koki) to facilitate the angle adjustment. The BBO crystal was placed approximately 2.5 m from the output port of the dye laser so that the beam diverged and smoothed to diminish the maximum intensity to become less than the damage threshold of the BBO crystal. This process allows us to maximize the energy into the crystal (beam size about 3 × 3 $mm^2$) and to maximize the output energy. The range of angle adjustment is small for BBO at a specific wavelength. Table 2-2 lists data for the BBO crystal. A prism (Pellin-Broca) was placed after the BBO crystal to separate the UV and fundamental beams, and was set near the Brewster angle for UV light to diminish the reflection losses. The visible wavenumber $\omega_2$ in the range 12,820–33,333 $cm^{-1}$ (~300–780 nm) was generated with a second dye laser (Scanmate 2E, Lambda Physik, bandwidth = 0.19 $cm^{-1}$) that was pumped with the same Nd:YAG laser of output at third harmonic 355 nm or second harmonic 532 nm. The visible light passed a telescope (+250 mm, –100 mm) according to the alignment of two S1UV prisms to expand the beam size to 5 × 5 $mm^2$. A half-wave plate placed behind the telescope served to rotate the polarization of $\omega_2$ from vertical to horizontal. The visible light was aligned to merge with the

UV beam via a dichroic mirror (CVI, LWP-45-R210-TP308-PW-1025-UV) and a high reflection mirror. Both UV and visible beams were focused into a gas cell containing Kr and Ar in a mixture (1:3 at total pressure 50 Torr) with a lens ($MgF_2$, $f$ = 200 mm) mounted on a 3D stage (with micrometer). The VUV wavenumber was tuned by scanning the wavenumber of $\omega_2$ . The resulting VUV ( $\omega_{VUV} = 2\omega_1 - \omega_2$ ) light, in the range 60,759–81,272 $cm^{-1}$ (~7.53–10.08 eV), was separated from the UV and visible fundamental light with a convex lens ($MgF_2$, $f$ = 150 mm); this lens, mounted at the end of the gas cell, has refractive indices $n$ (125–150 nm) ≅ 1.588–1.484, $n$ (212.6 nm) ≅ 1.410, and $n$ (350–500 nm) ≅ 1.393–1.381.[10] Because the $MgF_2$ lens are only transparent for the wavelength greater than 115 nm (wave number < 87000 $cm^{-1}$), VUV generated through resonance-enhanced sum-frequency mixing was blocked.

An optical delay line, consisting of two quartz prisms placed between the dye laser and the BBO crystal, served to adjust the timing between beams of wavenumbers $\omega_1$ and $\omega_2$ to ensure their overlap at the same time.

The wavelength of the dye lasers was calibrated with a wavemeter (WA5500, Burleigh, 190–680 nm, accuracy= 0.2 $cm^{-1}$) and two optogalvanic cells (OG); the VUV wavelength was thereby calibrated. To ensure that the UV frequency was fixed at 47,046.43 $cm^{-1}$, a homemade Kr optogalvanic cell was used to confirm the wavenumber of $\omega_1$. The change in the electric conductivity of a discharge plasma produced on illuminating the discharge with the radiation that is resonant with an atomic or molecular transition in the discharge. When the wavelength of the incident laser and the absorption are perfectly resonant, the maximum optogalvanic signal is obtained. Because the absorption wavelength is known, observing the obtained optogalvanic signal enables the measurement of the absolute wavelength of the incident laser with great precision. Figure 2-9 shows a scheme for construction of the optogalvanic cell and its operating circuit. The core of the galvatron was a pair (ϕ6 × 6 mm) of cylindrical Cu

electrodes placed at the center of a glass cylinder (ϕ25 × 120 mm) that was sealed with two $CaF_2$ windows and contained gaseous Kr (pressure approximately 3 Torr). A 150-V discharge across the galvatron electrodes produced satisfactorily cool, dense and stationary plasma. A laser beam was coincidentally directed along the axis of the discharge region. A ballast resistor (40 kΩ) not only prevented uncontrolled growth of current after the discharge was struck but also provided a simple method of measuring the discharge current. The voltage decrease across the ballast resistor was fed to the oscilloscope through a capacitor (0.047 μF at 1 kV). The AC component of the voltage decrease passed the capacitor, while the large DC component of the voltage decrease was isolated. A Fe-Ne optogalvanic cell (Hamamatsu Photonics) served to calibrate the wavelength of beam with wavenumber $\omega_2$. The accuracy of the calibration is estimated to be better than 0.2 $cm^{-1}$ for the fundamental outputs of the dye lasers. The estimated accuracy for the VUV radiation is better than 1 $cm^{-1}$. Figure 2-10(a) shows an example of the optogalvanic spectrum recorded when the wavelength of the dye laser was scanned from 510.3 to 514.2 nm with a step size 0.025 nm. The absorption maxima were fitted with a Gaussian function to locate the center of peaks. Figure 2-10(b) shows a stick diagram of the vacuum wavelengths of intense transitions for lines of atomic Ne and Fe.[25] Figure 2-11 shows the wavelength shifts of the fundamental output ($\omega_2$ beam) of the dye laser measured simultaneously with an optogalvanic cell and a wavemeter. The wavelength shift is 1.786 ± 0.018 nm.

#### 2.2.1.3 IR Optical Parametric Oscillator/Amplifier (OPO/OPA) Laser System

The IR radiation used in the two-photon IR-VUV experiment was generated with a KTP/KTA-OPO/OPA system (Laser Vision). The IR-OPO/OPA system is a multi-stage nonlinear device designed to convert the output of a Nd:YAG laser system at a fixed-frequency

into a laser tunable to radiation in the mid-infrared range. The tunable IR output from the use of a single set of nonlinear crystals spanned from 712 to 880 nm, and from 1.35 to 5.0 μm.

Figure 2-12 shows the layout of the IR-OPO/OPA system. The OPO/OPA system was pumped with an injection-seeded Nd:YAG laser (PL8000, Continuun, 10 Hz). The output (1064 nm, ~400 mJ, pulse width 8 ns, horizontally polarized) of the Nd:YAG laser was divided into two separate beam lines with a beamsplitter. The frequency of one beam was doubled in a KTP crystal to provide the pump light (532 nm, vertically polarized) for the OPO, while the second beam was directed through a delay before recombination with the idler output from the OPO stage. The combined beams were then directed into an OPA stage pumped at 1064 nm for difference-frequency mixing. A half-wave plate in a rotation stage before the harmonic generator (KTP crystal) enabled a continuous variation of the efficiency of conversion; the intensity of light generated at 532 nm became thereby adjustable. A reflector at 532 nm following the doubling crystal removed the residual light at 1064 nm and directed the light at 532 nm to the OPO. The OPO stage consists of a grating (1800 grooves/mm, near grazing incidence) and a tuning mirror in combination, a reflector, two angle-tuned KTP crystals (the second to compensate the displacement of the beam), a prism, an aluminium mirror and an end mirror. The 532-nm beam was coupled into the cavity through a reflector located between the KTP crystals and the prism; this beam passed the crystals twice with reflection at the end mirror of the cavity.

The OPO stage has two configurations for operation in the broad and the narrow band modes. In the broad-band configuration, the tuning mirror was blocked and an aluminum mirror reflected light off the prism back towards the crystal. The prism with a high reflection index was set at an angle of 20 degrees respect to the incidence beam. Since the broad-band configuration has no frequency-selection optics, the output bandwidth is approximately 1.5 $cm^{-1}$ (FWHM). In the narrow-band configuration, the aluminum mirror is blocked, and a

combination of grating and tuning mirror and prism beam expansion are used to reduce the output bandwidth to roughly 0.2 $cm^{-1}$ (FWHM). The grating was placed at a grazing incidence angle of 5 degrees. The tuning mirror, which was mounted on a rotation stage, was set to reflect the first order diffraction of the resonated signal wave. The end mirror of the OPO transmitted most of the idler and a portion of the signal generated by the first pass of the pump at 532 nm through the crystals. This output passed first through a variable half-wave plate waveplate to rotate the polarization of the idler from vertical to the horizontal as required by the OPA stage. A silicon polarizer transmitted the idler wave and reflected the signal wave present in the OPO output. A 1064-nm high reflector following the silicon polarizer combined the idler from the oscillator with the 1064-nm pump beam for amplification and difference frequency generation in the KTA OPA crystals. Behind the OPA stage is a dichroic mirror, which allows the co-propagating signal and idler waves to pass through the dichroic mirror while the residual 1064 nm pump beam is removed. A Brewster plate polarizer placed behind the dichroic mirror was used to isolate either vertically polarized idler (2.1–5 μm) or the horizontally polarized signal wave (1.35–2.1 μm) from the OPA output. Figure 2-13 shows a plotted graph comparing the output power of the OPO/OPA system in 2000–8000 $cm^{-1}$ and the output power of a Raman shifter system in 2000–10000 $cm^{-1}$. Signal wave from OPO output was aligned using two Al mirrors into a wavemeter (Burleigh WA4500, 400–110 nm, accuracy = ±0.02 $cm^{-1}$ at 700 nm) for wavelength calibration. Etalon B inside the wavemeter has parallel mirrors, with 5.01 mm spacing, which produces concentric circular interference fringes when illuminated with a diverging monochromatic light. A linear CCD array placed at the vertical center of the fringe was used to detect the fringe pattern. Figure 2-14 shows the spectrum of etalon B with NIR output at 12293 $cm^{-1}$ from OPO cavity. The spectrum was taken when the seeder of pumping YAG laser was turned on.

A home-made photoacoustic cell is filled with a reference gas, such as $CH_4$, $C_2H_2$, and

$H_2O$, and is sealed with $CaF_2$ window on both sides. A microphone (Hosiden, KUC1223) was need as detector. The photoacoustic cell was used to calibrate the frequency of IR output from OPA stage in the range of 2900–3700 $cm^{-1}$; the spectrum was synchronized with frequency scanning of OPO/OPA system. Photoacoustic spectroscopy has been widely used as a highly sensitive technique for trace gas measurement. The theory of photoacoustic effect in gases has been described in the previous paper.[26] The physical processes occurring after optical excitation of molecules by IR laser can be divided into three steps. First, the molecule absorbs photons via rovibrational transitions, and then the molecule in the excited state was deactivated by collisional relaxation, in which the energy is transformed into translational energy, and then releases local heat. Second, the acoustic wave is generated due to localized transient heating and expansion. Finally, the acoustic signal is detected in the photoacoustic cell with a microphone. Figure 2-15(a) shows a scheme diagram for setup used to record the photoacoustic spectrum. A little portion of the IR laser radiation was extracted with a sapphire window to the photoacoustic cell. The photoacoustic signal was amplified and filtered with a voltage amplifier (Stanford research, SR560). The input signal was AC coupled and the filter frequency was set in the range of 10–100 K Hz. The output signal is fed into a Standford Research SR250 gated integrator (gate width ~2 μs, sensitivity 10 mV), and the gated signal obtained by the boxcar integrator was then fed into a personal computer through SR 245 interface. By scanning the frequency of IR laser and monitoring the increase of photoacoustic signal, photoacoustic spectrum of reference gases was obtained. By comparing the IR spectrum taken from FTIR with photoacoustic spectrum, the wavelength of OPO/OPA system can be calibrated. Figure 2-15(b) shows FTIR spectrum (resolution = 0.5 $cm^{-1}$) and photoacoustic spectrum (broadband mode, resolution = 1.5 $cm^{-1}$) of $CH_4$ (2900–3200 $cm^{-1}$), $C_2H_2$ (3200–3350 $cm^{-1}$), and $H_2O$ (3500–3700 $cm^{-1}$). The photoacoustic spectrum wasn't normalized by IR intensity.

In the front of the $CaF_2$ entrance window of vacuum chamber, a parabolic silver-coated mirror ($f$ = 20 cm) was used to introduce and focus the tunable IR laser beam into the molecular beam upstream from its intersection with the VUV beam. The intensity of the IR laser varies with wavelength; in the spectral range of 2700–3700 $cm^{-1}$ the energy is typically 1–5 mJ before entering the ionization chamber and the fluence at the ionization region is about 1–5 mJ $mm^{-2}$.

#### 2.2.1.4 Photolysis Laser

The free radicals were produced on photolysis of the precursor molecule either with a KrF or ArF excimer laser (EX100H, Gam Laser) at 248 or 193 nm. The output energy of excimer laser is 100 mJ $pulse^{-1}$ at 248 nm and 60 mJ $pulse^{-1}$ at 193 nm. The photolysis beam was loosely focused with a S1UV lens ($f$ = 30 cm) to a point about 2 mm downstream from the orifice of the nozzle. Typically, 50 mJ $pulse^{-1}$ of laser energy with a beam size ~2 × 4 $mm^2$ was employed.

### 2.2.2 Time-of-Flight (TOF) Spectrometer

The IR-VUV photoionization apparatus is equipped with a TOF mass spectrometer for ion detector. Figure 2-16 shows a TOF setup of the apparatus, which consists of a supersonic jet system, a time of flight tube, and a MCP detector. Following is going to describe details for each component.

#### 2.2.2.1 Supersonic Jet System

The supersonic molecular beam technique[27] has been widely used in photoelectron, laser induced fluorescence (LIF), resonance-enhanced multiphoton ionization (REMPI), and photofragment yield measurements to cool the neutral gaseous sample to reduce the thermal rotational and vibrational temperatures.[28] The use of a skimmed molecular beam generated by a pulsed supersonic expansion brings two main advantages: First, it permits an efficient cooling of the translational, vibrational, and rotational motion of the molecules and hence ensures that only the lowest rotational levels of the vibronic state are populated. Second, the short duration time of the gas pulses (~200 μs or 30 μs) enables great reducing the gas load in the chamber, thus the pumping requirements, without reducing the gas density at the place of the detection.

In our system, the molecular beam source chamber and photoionization chamber are divided by a metal shield in the time-of-flight (TOF) spectrometer (R. M. Jordan Company). Both source chamber and photoionization chamber are evacuated by turbo molecular pumps (STP-600, Seiki Seiko, and V-551, Varian); the pressure of the source chamber and photoionization chamber are $1.2\times10^{-7}$ and $8\times10^{-8}$ Torr, respectively, without gas input and $1.0\times10^{-6}$ and $7\times10^{-7}$ Torr, respectively, under typical operating conditions.

The probe gas sample was introduced into the photoionization chamber using a pulsed supersonic expansion through a solenoid valve (General Valve Series 9 or Evan Lavie valve,[29] nozzle orifice diameter of 0.5 mm or 1 mm, operated at 10 Hz). Generally, pulse duration of General Valve and Evan Lavie valve was 200 μs and 30 μs, respectively, at stagnation pressure of 3 atm. Low temperature molecular beam were formed during the adiabatic expansion through the nozzle. The pulsed molecular beam was further collimated by a skimmer before entering the photoionization chamber. The orifice diameter of the skimmer (Beam Dynamics, Model 1) is 1 mm and the pulsed valve is located about 20 mm in front of skimmer. The jet-cooled beam passes through a skimmer to enter the ionization region of the TOF mass

spectrometer, which was 13 cm downstream from the skimmer.

#### 2.2.2.2 Linear Time-of-Flight Tube (TOF)

The linear time of flight tube is a perpendicular setup commonly employed in mass spectrometry and molecular spectroscopy. This configuration has the advantage of having almost no Doppler shift and minimized effects of initial molecular beam velocity. The total length of the TOF tube is about 100 cm. Three electrodes are installed at the center of the ionization region where photoionization occurs. These three electrodes were used to provide kinetic energy to ions to be extracted and accelerated into TOF tube before being detected with a MCP detector. The three electrodes, from bottom to top, are repeller plate, extraction grid, and ground grid; they were separated by a distance of 1 cm. The voltages applied on these electrodes are $V_{A1}$, $V_{A2}$, and zero, respectively. Typically, a DC field ≈ 200 V $cm^{-1}$ ($=\frac{(V_{A1} - V_{A2})}{1\,cm}$) is maintained between the repeller plate ($V_{A1}$) and extraction grid ($V_{A2}$). Two sets of steering plates (X, Y) installed inside TOF tube were used to correct the flight path of ions. Moreover, a cold trap surrounding the flight tube filled with liquid nitrogen was used to freeze the residual sample molecules in the flight tube to reduce the interference from background signal.

#### 2.2.2.3 Microchannel Plate (MCP) Detector Assembly

A MCP detector assembly was placed on the top of a linear TOF tube for ion detection. This assembly comprises of seven components: Four electrode plates, two MCP plates, and an

anode pad, as shown in the inset of Figure 2-16. The bottom plate is a ground potential input grid, which has zero voltage as the field-free voltage to ensure field-free over the flight length and to eliminate possible ion beam divergence before entering the accelerating plate. The second plate is the hollow electrode plate, with a potential ($V_{D1}$ = 0–2300 V, typically at –1450 V) to provide kinetic energy for ions and suppress electrons to enter the MCP. The voltage applied on the third and fourth plates (both are hollow) are 54.5 % and 9.1 % of $V_{D1}$, respectively. Electrons generated by MCP hit the anode pad and then create an electric current. A double-stage 18 mm chevron microchannel plate (MCP, Burle Electro-Optics) was used in this experiment setup. This MCP has an output impedance of 50 Ω and provides high gain ($1\times10^7$ with $V_{D1}$ at –2400V) with sub-nanosecond rise time.

#### 2.2.2.4 The Total Flight Time

When molecules were ionized, the ions were extracted and accelerated by the electric field between the repel plate ($V_{A1}$) and the extraction grid ($V_{A2}$) and between the extraction grid and the ground grid (GND). Ions with an equal charge would have the same kinetic energy, which is:

$$\frac{1}{2}m_1v_1^2 = \frac{1}{2}m_2v_2^2, \tag{9}$$

in which $m$ is the mass, v is the velocity, and indeces 1, 2 indicate two ions with the same charge. After flying through the field-free tube, ions with different m/z values would have different arrival time to MCP. The flight time t for a singlly charged ion with mass $m$ and kinetic energy KE ($=\frac{1}{2}mv^2$) to fly over the field-free tube with length L is given by $t = L\sqrt{m/(2KE)}$. The flight time is proportional to the square of the mass. The mass $m$ can be determined by measuring the time of flight when the energy of ion is set to a fixed value. The total flight time

is given by the flight time in regions of $d_1$, $d_2$, L and $d_4$, shown in Figure 2-16, that is, $t = t_1 + t_2 + t_3 + t_4$. The following analysis gives the definition of each period.[30]

The flight time $t_1$ indicates the period that the ion travels from the ionization point the extraction grid. The flight distance is s ($=\frac{1}{2}at^2$), in which $a$ is the acceleration. Because the distance between repel plate ($V_{A1}$) and extraction grid ($V_{A2}$) is $d_1$, and the voltage difference between them is $V_P$ ($= V_{A1} - V_{A2}$), the electric field is $V_p/d_1$. For an ion with charge $q$, the electric field is $\frac{ma}{q}$. Hence, $\frac{V_P}{d_1} = \frac{ma}{q}$ , and, $a = \frac{V_P q}{m d_1}$. The flight time $t_1$ can be derived from the following equation,

$$t_1 = \sqrt{\frac{2s}{a}} = \left(\frac{2smd_1}{V_P q}\right)^{\frac{1}{2}} = (2m)^{1/2}\left(\frac{sd_1}{V_P q}\right)^{1/2}. \quad (10)$$

Consequently, the velocity of ion at extraction grid is $v_1 = \left(\frac{2sV_P q}{md_1}\right)^{1/2}$.

The flight time $t_2$ indicates the period that the ion travels from the extraction grid to the ground grid (GND) with a distance $d_2$. Because of conservation of momentum, $q\frac{V_{A2}}{d_2}t_2 = m(v_2 - v_1)$, in which $v_2$ is the velocity of ion at ground grid. $v_2$ may be derived by the conservation of kinetic energy, as expressed in the following,

$$KE = q \cdot \frac{V_P}{d_1} \cdot s + q \cdot V_{A2} = \frac{1}{2}mv_2^2 \quad (11)$$

in which $v_2 = \left(\frac{2q}{m}\left(\frac{V_P}{d_1} + V_{A2}\right)\right)^{1/2}$. The flight time $t_2$ is given by

$$t_2 = \left(\frac{2m}{q}\right)^{1/2} \cdot \left(\frac{d_2}{V_{A2}}\right)\left[\left(\frac{s \cdot V_P}{d_1} + V_{A2}\right)^{1/2} - \left(\frac{s \cdot V_P}{d_1}\right)^{1/2}\right]. \quad (12)$$

The time $t_3$ required by the ion of mass $m$ to fly over a field-free tube with length L, is expressed as

$$t_3 = \frac{L}{v_2} = L \cdot \left[\frac{2q}{m}\left(\frac{V_P \cdot s}{d_1} + V_{A2}\right)\right]^{-1/2}. \quad (13)$$

The flight time $t_4$ is the period that the ion travels from the ground grid of the MCP

detector to the first MCP with a distance of $d_4$. The voltage difference between them is $U_1$=0.545 $V_{D1}$. The velocity of ion at the first MCP is $v_3$, which can be derived by the assumption of the conservation of kinetic energy, $\frac{1}{2}mv_3^2 = q \cdot \frac{V_P}{d_1} \cdot s + q \cdot V_{A2} + q \cdot U_1$, $v_3 = \left[\frac{2}{m}\left(q \cdot \frac{V_P}{d_1} \cdot s + q \cdot V_{A2} + q \cdot U_1\right)\right]^{1/2}$. Because of the conservation of momentum, $q\frac{U_1}{d_4}t_4 = m(v_3 - v_2)$, the flight time $t_4$ is expressed as

$$t_4 = \frac{md_4}{qU_1}\left(\frac{2}{m}\right)^{1/2}\left[(K + qU_1)^{1/2} - K^{1/2}\right], \quad (14)$$

in which, $K = q \cdot \frac{V_P}{d_1} \cdot s + q \cdot V_{A2}$ (15)

For example, in this experiment setup, with $d_1$ = $d_2$ = 1 cm, L = 1 m, $d_4$ = 2.9 cm, the flight time t for $CH_3SH$ with m/z = 48 appears at 14.0 μs, when $V_{A1}$, $V_{A2}$, and $V_{D1}$ were set at 1700, 1500, and 1450 V, respectively.

### 2.2.3 Data Acquisition

The output signal from the MCP was amplified with a fast amplifier (EG&G ORTEC, Model 9306, bandwidth 1 GHz, rise time of 350 ps and a non-inverting gain of 100) before feeding the signal into a digitizer. The input of this amplifier is ac-coupled with a 50 Ω input impedance and is protected to a maximum of ± 1 V. The ac-coupled output signal provided a linear output range from 0 to –1.75 V and a maximum output of –2 V into a 50-Ω load. The TOF mass spectrum was recorded with a 14-bit digitizer (GaGe Instruments, Model CS8327, 100 MS/s) and was also displayed on a digital oscilloscope. The signals from the photoacoustic cell and the power sensor were recorded with two boxcar gated integrators (SR250, Standford Research). The gated signal obtained by both boxcar integrators were sent to a personal computer through a SR 245 interface.

During the experiment, an 8-channel digital pulse generator (Berkeley Necleonics Corporation, model BNC 575) was used to control the timing of various optical and mechanical components of the apparatus, such as opening the pulse valve, firing lasers, and triggering boxcar integrators and the GaGe board. A typical timing sequence in an IR-VUV photoionization measurement is shown in Figure 2-17. The flash lamp of the Nd:YAG laser which was used to generate 355-nm beam was fired ~41 μs before the pulsed valve. The delay between IR and UV lights was typically set at 200 to 3000 ns for VUV-ID-IRPDS experiments and at 10 to 100 ns for IR-VUV-PI experiments.

A program for data acquisition and instrument control were written in Labview (National Instruments) language.

Table 2-1 Optimum pressures and conversion efficiencies for third-harmonic generation. (From Ref. 4)

| Wavelength (nm) | medium | Single medium | | mixture with argon | | |
|---|---|---|---|---|---|---|
| | | Pressure (Torr) | Relative efficiency | % medium | Pressure (Torr) | Relative efficiency |
| 118.2 | Xe | 2.2 | 5.7 | 8.0 | 178.0 | 100.0 |
| 121.5 | Kr | 14.0 | 1.0 | 28.0 | 350.0 | 9.3 |
| 122.8 | Kr | 3.0 | 1.1 | 8.0 | 100.0 | 2.2 |
| 122.9 | Kr | 2.5 | 0.4 | 6.0 | 100.0 | 2.4 |
| 123.2 | Kr | 1.0 | 0.7 | 4.0 | 34.0 | 0.7 |
| 127.1 | Xe | 25.0 | 7.9 | 50.0 | 84.0 | 13.2 |
| 127.6 | Xe | 14.0 | 6.1 | 25.0 | 152.0 | 21.4 |
| 128.2 | Xe | 5.5 | 3.1 | 12.0 | 257.0 | 32.3 |
| 128.9 | Xe | 2.0 | 0.6 | 4.0 | 200.0 | 9.6 |

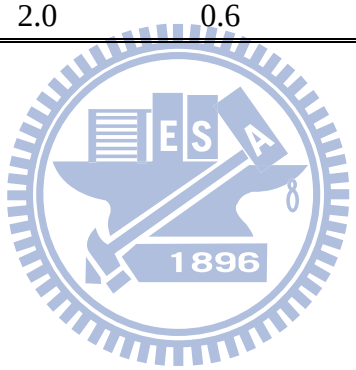

Table 2-2 Data sheet for type 1 BBO crystal used for doubling the 425.112 nm light.

| Items | Parameter |
|---|---|
| Dimension | 5x5x9 $mm^3$ |
| Coating | S1,S2:antireflection coating at 425/212.5 |
| Dimension Tolerance | ΔW(+0.1, -0.1), ΔH(+0.1, -0.1), ΔT(+0.5, -0.1) (mm) |
| Surface Quality | 10/5 Scratch/Dig |
| Flatness | λ /8 at 633 nm |
| Wavefront Disortion | λ/6 at 633 nm |
| Parallelism | ≦20” |
| Perpendicularity | ≦5’ |
| Clear Aperture | ≧90% |
| Chamfer width | ≦0.2 mm x 45∘ |
| Chip | ≦0.1 mm |

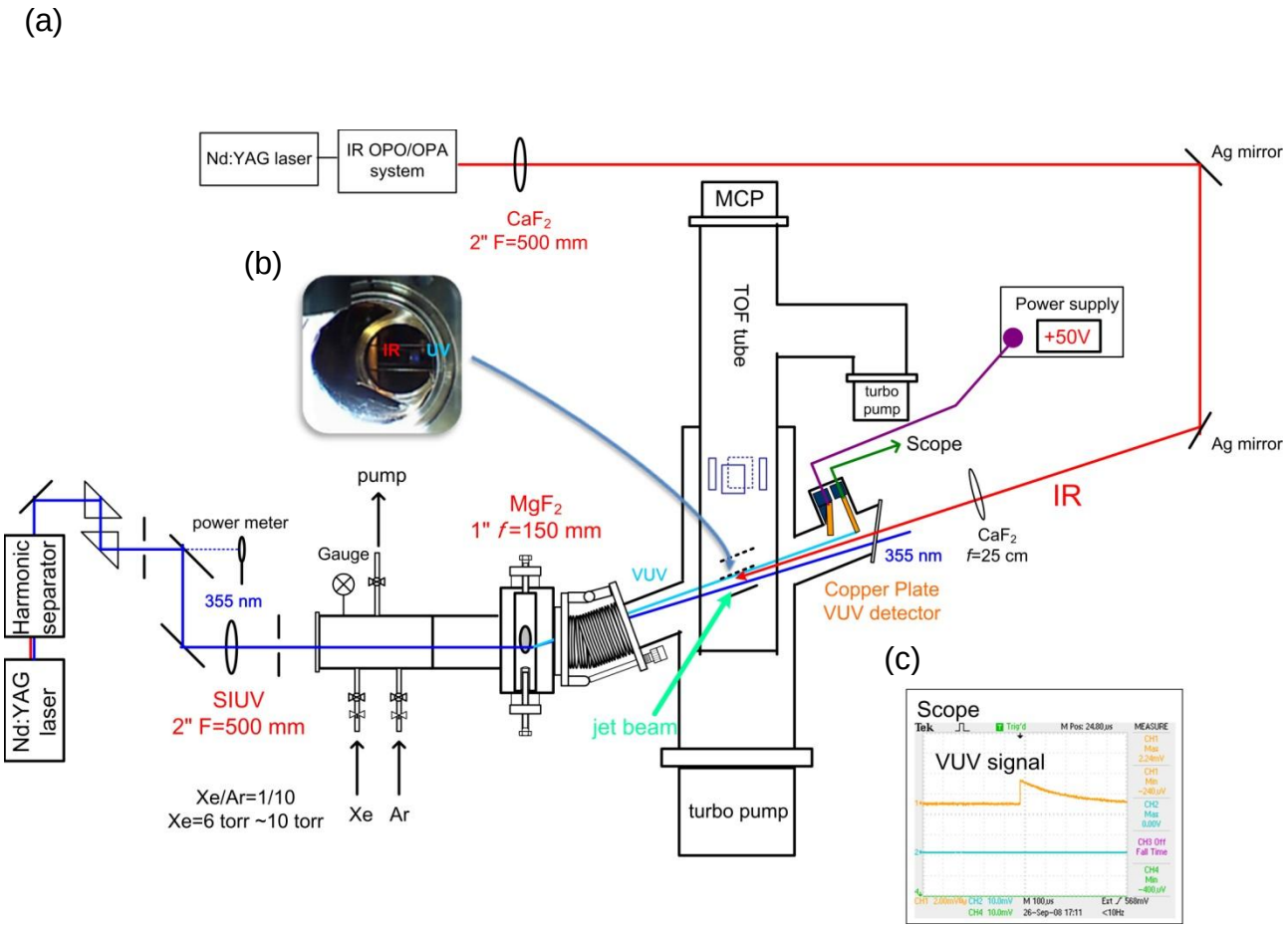


Figure 2-1 (a) A schematic diagram of the experimental apparatus of VUV-ID-IRPDS using 118 nm light as the VUV source. (b) Picture of the alignment of IR and UV laser beams at the position of ionization region. The distance between two beams is about 3 mm, when the delay time between IR and VUV lights was set to be 30 ns. (c) The intensity of VUV light measured with a copper photoelectric detector.

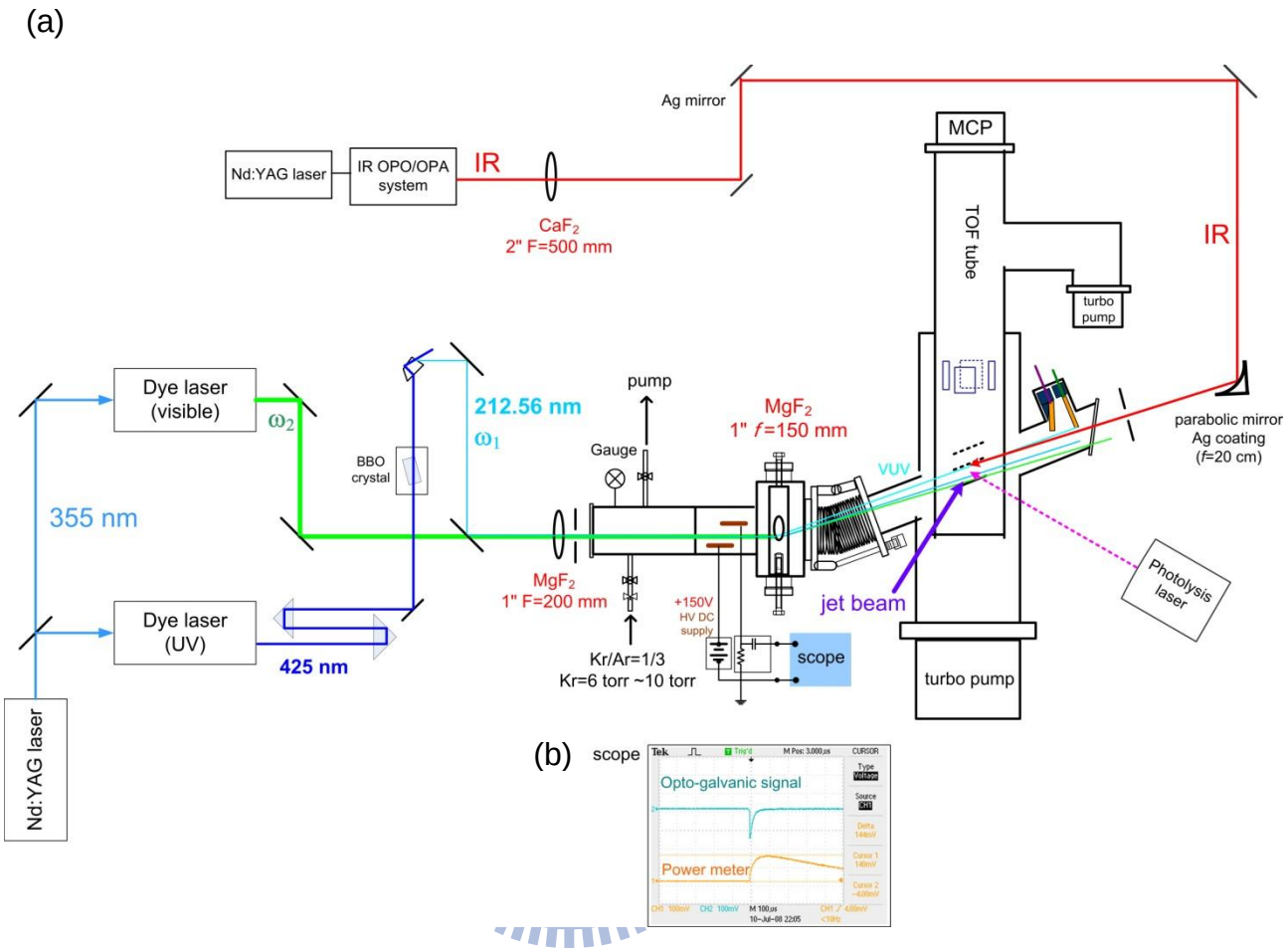


Figure 2-2 (a) The schematic diagram of the experimental apparatus of IR-VUV-PI using a tunable VUV light. (b) The observed optogalvanic signal. When the frequency of UV light is resonant with the two-photon Kr transition, maximum optogalvanic signal is obtained.

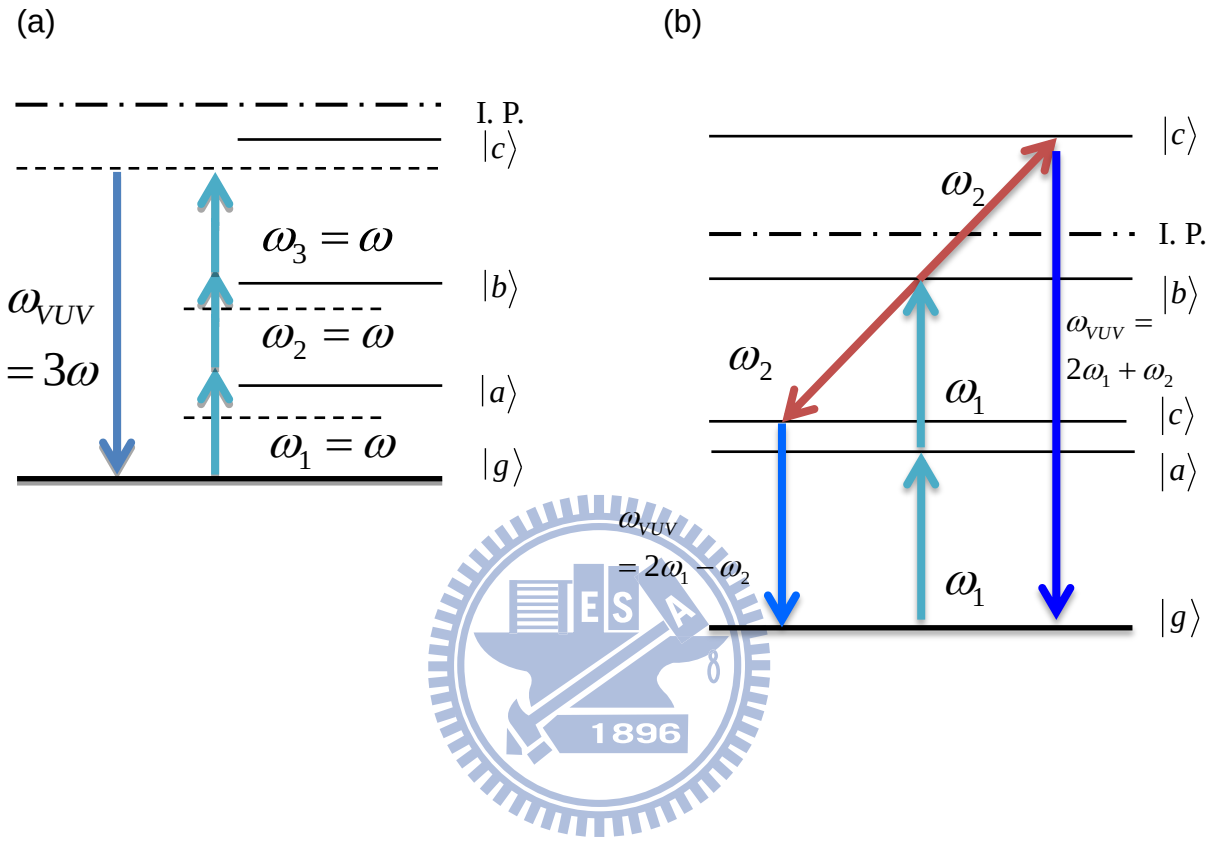


Figure 2-3 Schematic diagrams of (a) a nonresonant third harmonic generation process at the fundamental laser frequency ω, where $\omega_1 = \omega_2 = \omega_3 = \omega$ and $\omega_{VUV} = 3\omega$ and (b) a four-level system indicating the relevant energy levels for both four-wave sum frequency at $2\omega_1 + \omega_2$, and four-wave difference mixing at $2\omega_1 - \omega_2$. The real levels are labeled $|a\rangle$, $|b\rangle$, $|c\rangle$, and $|g\rangle$, I. P. = ionization potential and imaginary levels are present as solid line and dashed line, respectively. Real levels are labeled $|a\rangle$, $|b\rangle$, $|c\rangle$, and $|g\rangle$. I. P. = ionization potential.

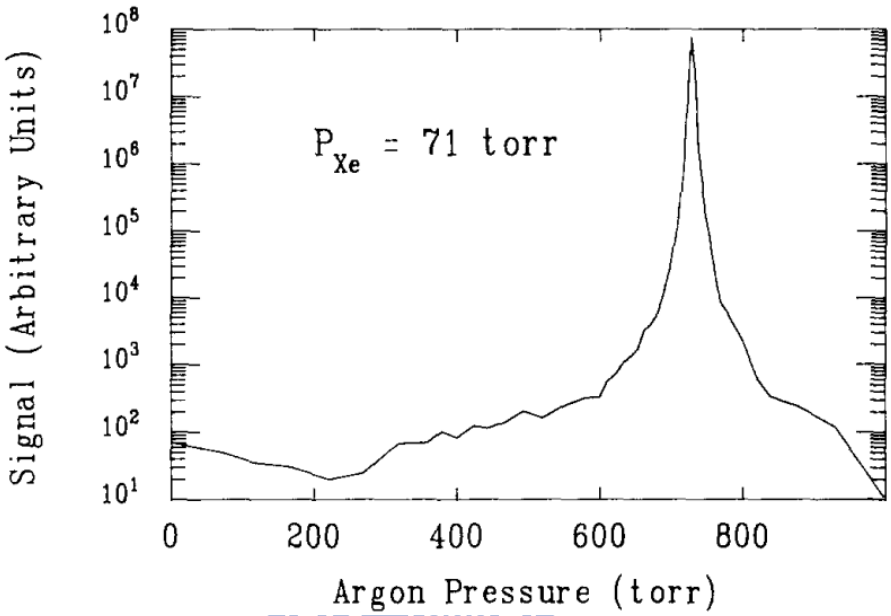


Figure 2-4 The 118.2-nm output power as a function of the pressure of added Ar in the tripling cell. The input 354.7-nm beam is in unfocused geometry. (From Ref. 9)

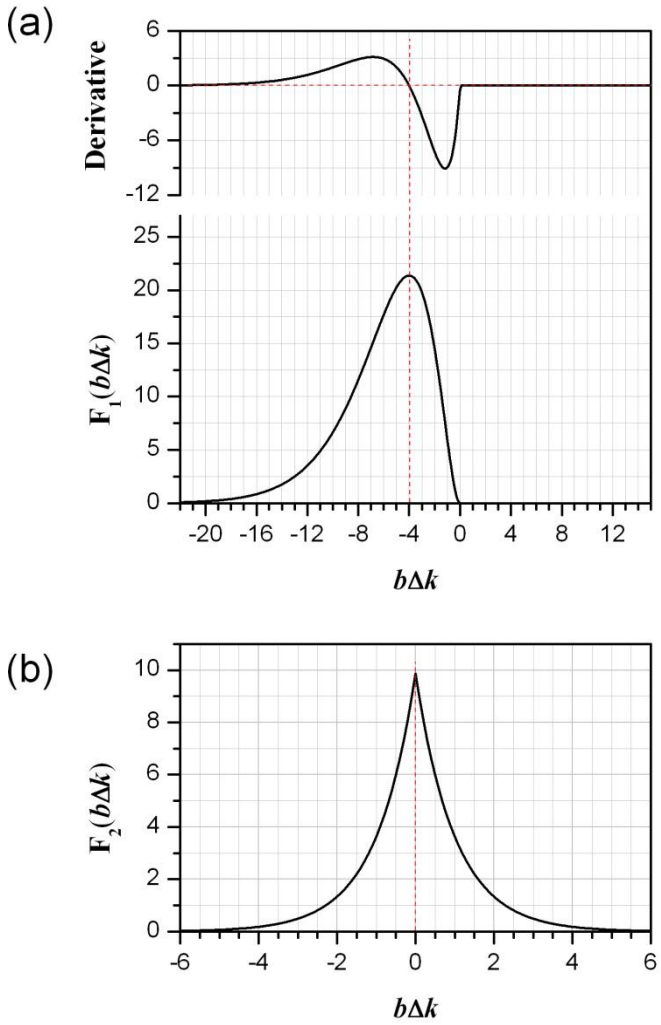


Figure 2-5 The phase-matching factors versus $F_i$ $b\Delta k$ in the case of tight focusing, for $b$/L=0 and $f$/L=0.5. (a) $F_{sum}(b\Delta k)$ versus $b\Delta k$. The upper trace is the derivative of $F_{sum}(b\Delta k)$. (b) $F_{diff}(b\Delta k)$ versus $b\Delta k$. $F_{sum}(b\Delta k)$ and $F_{diff}(b\Delta k)$ are the phase-matching factor in sum- and difference-frequency schemes.

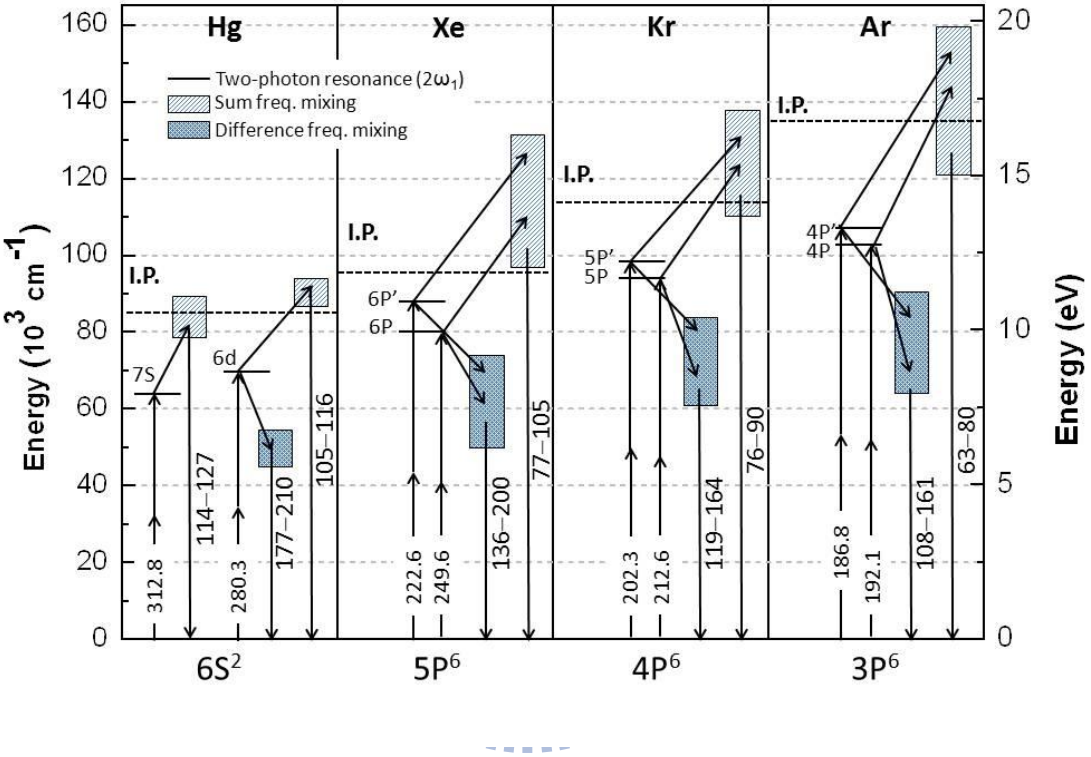


Figure 2-6 Energy level diagrams of relevant atomic levels of nonlinear media of Hg, Xe, Kr, and Ar for the generation of coherent VUV light via two-photon resonance four-wave sum and difference frequency mixing. The wavelength regions are indicated in nm. I.P. denotes the ionization limit of a non-linear medium.

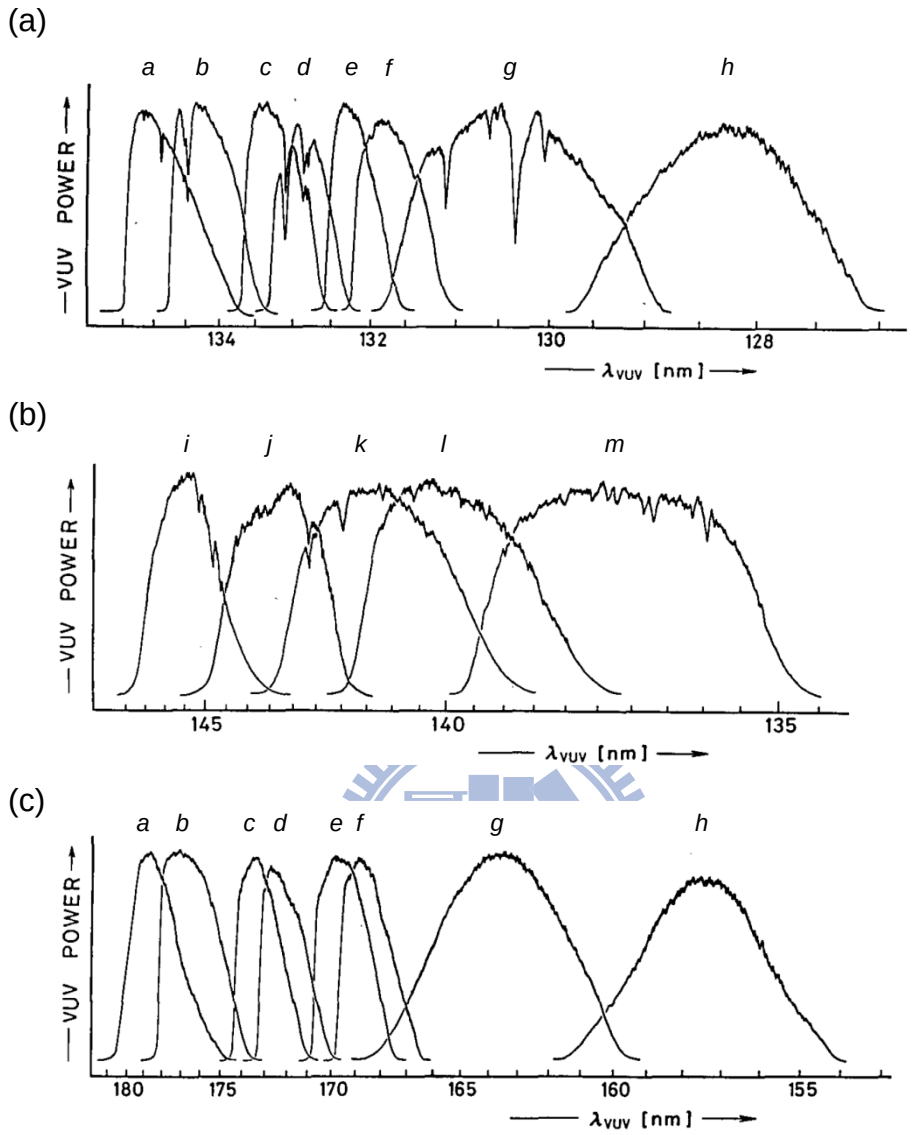


Figure 2-7 Wavelength dependence of the power of the VUV light produced by the difference frequency conversion ($\omega_{VUV} = 2\omega_1 - \omega_2$) in Kr. $\omega_1$ is fixed at 216.6 nm which is resonant with the two-photon Kr transition 4*p*-5*p* [5/2, 2]. (a) $\omega_2$ is in the range 540–737 nm produced by the fundamental output of the following laser dyes: *a*, Fluorescine 27; *b*, Rhodamine 6G; *c*, Rhodamine 610; *d*, Rhodamine 620; *e*, Rhodamine 640; *f*, Sulforhodamine; *g*, DCM; and *h*, Pyridin 1. (b) $\omega_2$ is in the range 416–550 nm produced by the fundamental output of the following laser dyes: *i*, Stilbene 420; *j*, Coumarin 440; *k*, Coumarin 460; *l*, Coumarin 480; *m*, Coumarin 500. (c) $\omega_2$ is in the range 272–360 nm produced by the second harmonic generation of with the same laser dyes as listed in (a). The VUV power is plotted in arbitrary units. The tuning curves are not displayed on the same scale. (From Ref. 14)

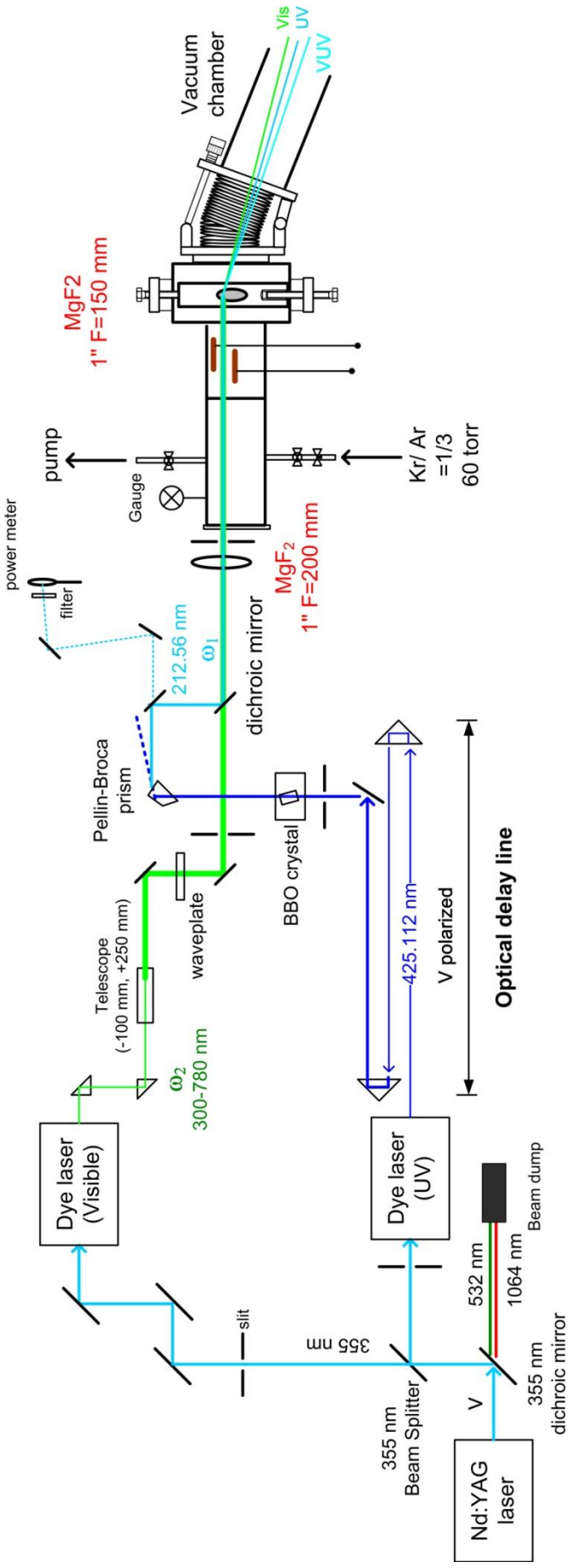


Figure 2-8 A detailed schematic diagram for generation tunable VUV light by resonance enhanced four-wave difference frequency mixing ($\omega_{VUV} = 2\omega_1 - \omega_2$) in a Kr/Ar gas cell via the Kr 4P→5P transition at 94,092.86 $cm^{-1}$ (= $2\omega_1$). $\omega_1$ (212.556 nm) is generated by doubling of the laser output from a Stilbene 420 dye (425.112 nm).

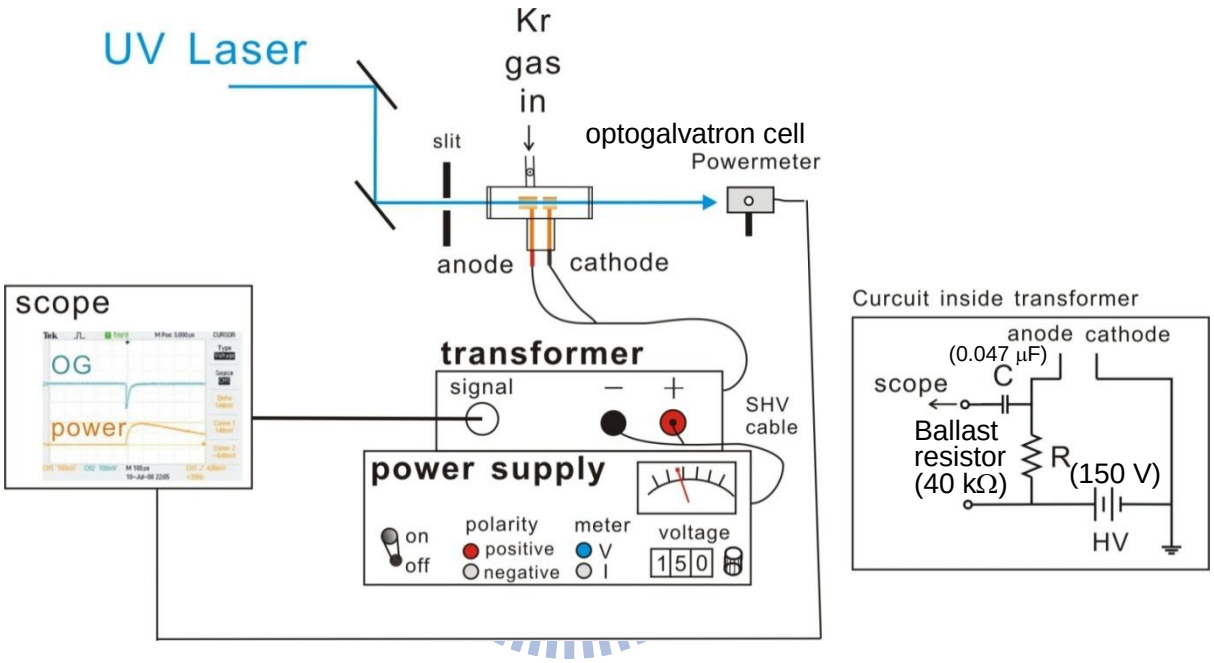


Figure 2-9 A schematic diagram for measurements of the optogalvanic spectra.

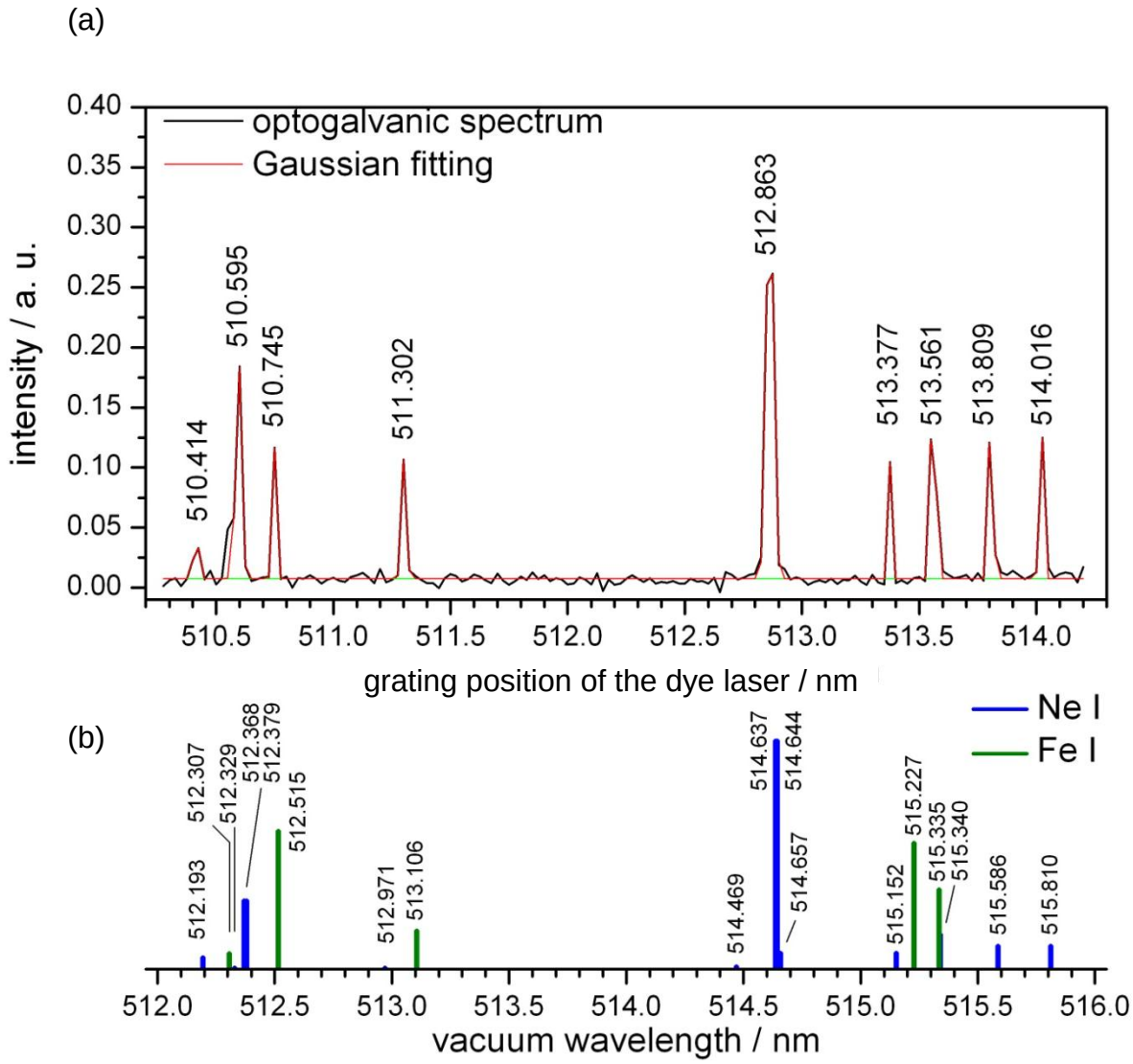


Figure 2-10 (a) The optogalvanic spectrum recorded with a Fe-Ne cell when scanning the grating position of the dye laser ($\omega_2$) from 510.3 to 514.2 nm with a scan step of 0.025 nm. (b) Stick diagram of vacuum wavelength of transition lines of Ne and Fe atoms (from Ref. 25); only intense transitions are plotted.

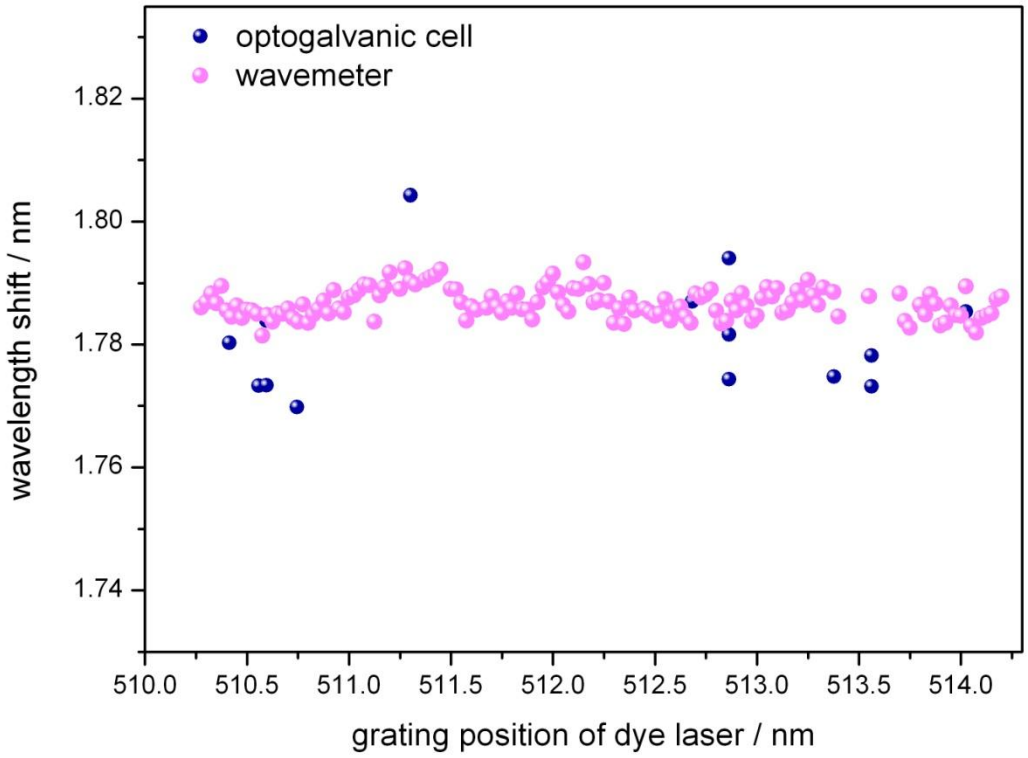


Figure 2-11 Comparison of derivation from the true wavelength for the wavelength read out of a dye laser calibrated with an optogalvanic cell and a wavemeter.

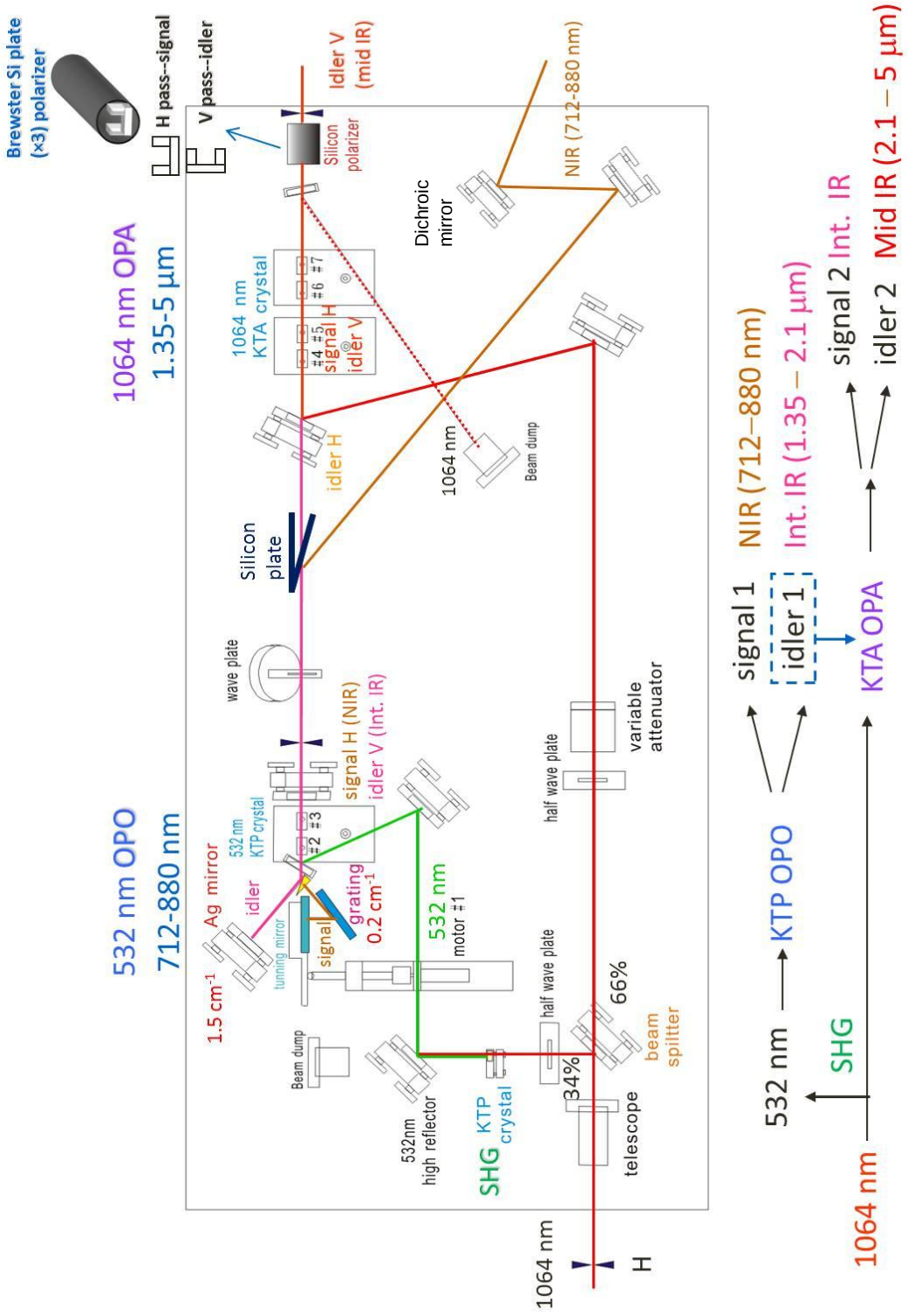


Figure 2-12 Layout of the IR-OPO/OPA laser system (Laser Vision).

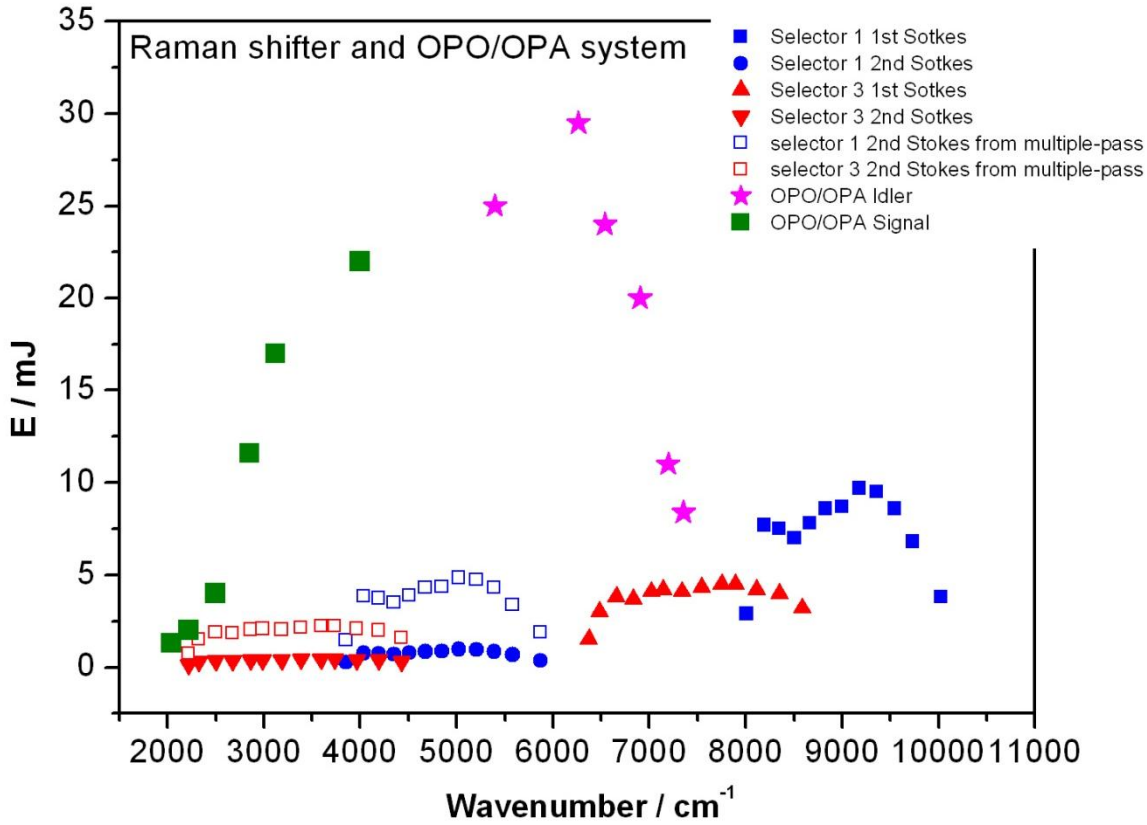


Figure 2-13 Output energy of the IR OPO/OPA system and the $H_2$ Raman shifter system in our lab.

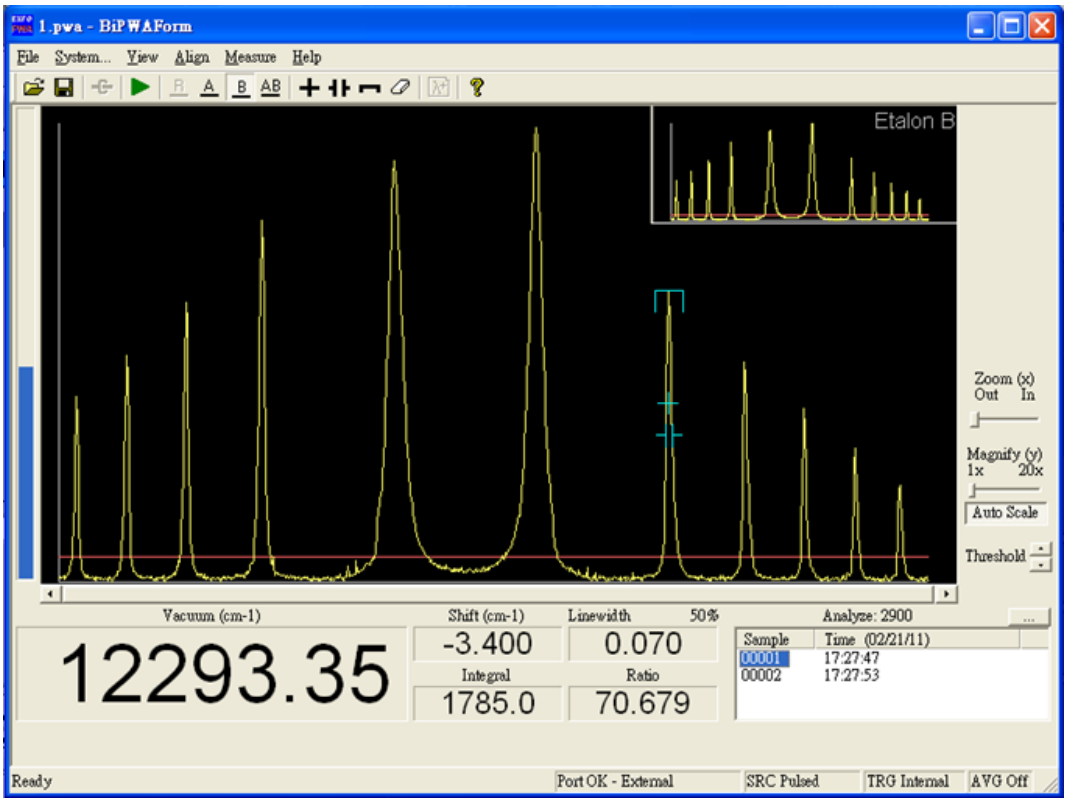


Figure 2-14 The interference spectrum of etalon B with NIR output from OPO cavity. The frequency of NIR was set at 12293 $cm^{-1}$.The spectrum was taken when the seeder of pumping YAG laser was turned on.

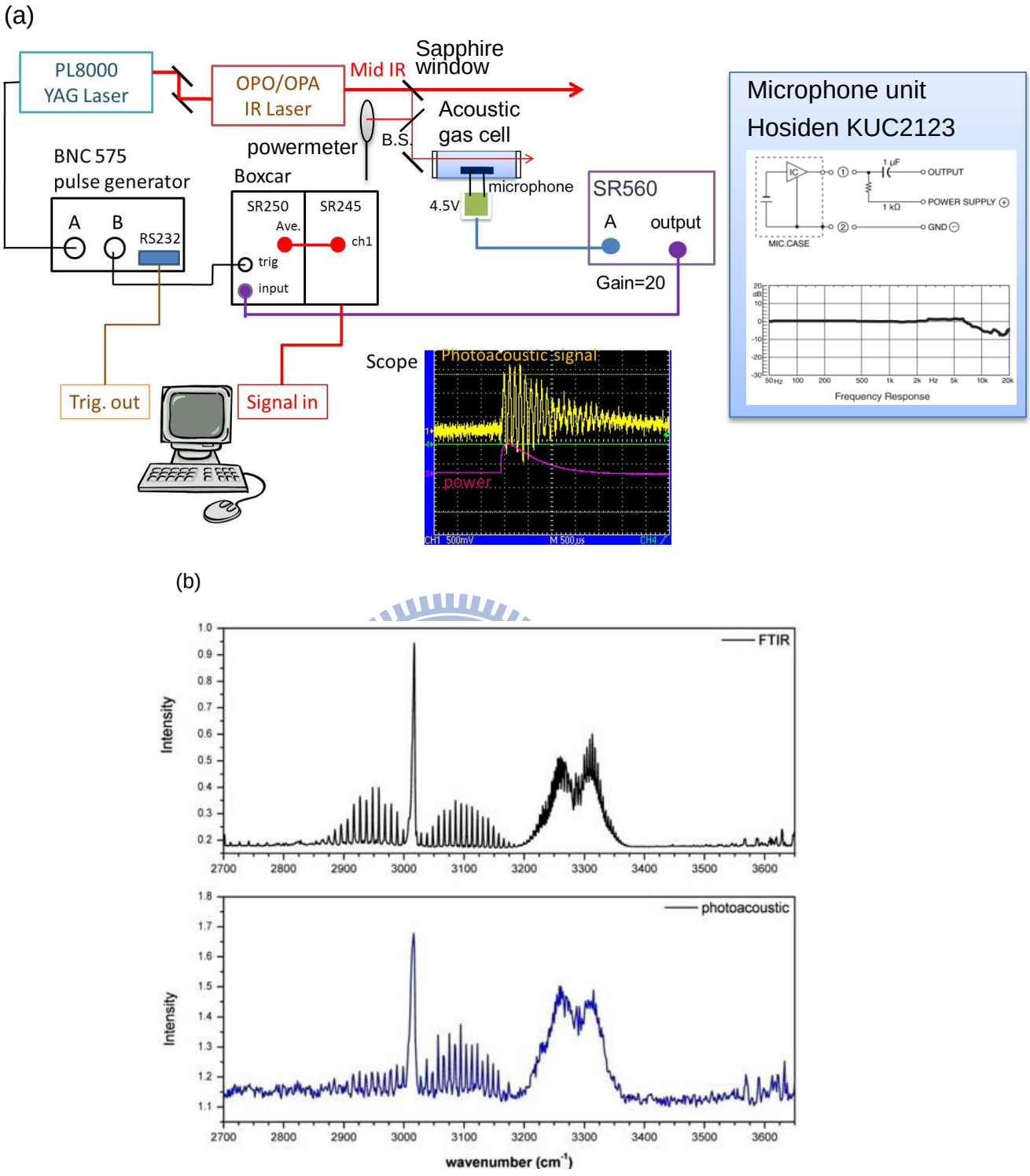


Figure 2-15 (a) A schematic diagram for measurements of a photoacoustic spectrum. B.S. is a 50:50 beam splitter. (b) FTIR spectrum (resolution = 0.5 $cm^{-1}$) and photoacoustic spectrum (broadband mode, resolution = 1.5 $cm^{-1}$) of $CH_4$ (2900–3200 $cm^{-1}$), $C_2H_2$ (3200–3350 $cm^{-1}$), and $H_2O$ (3500–3700 $cm^{-1}$). The photoacoustic spectrum wasn't normalized with IR intensity.

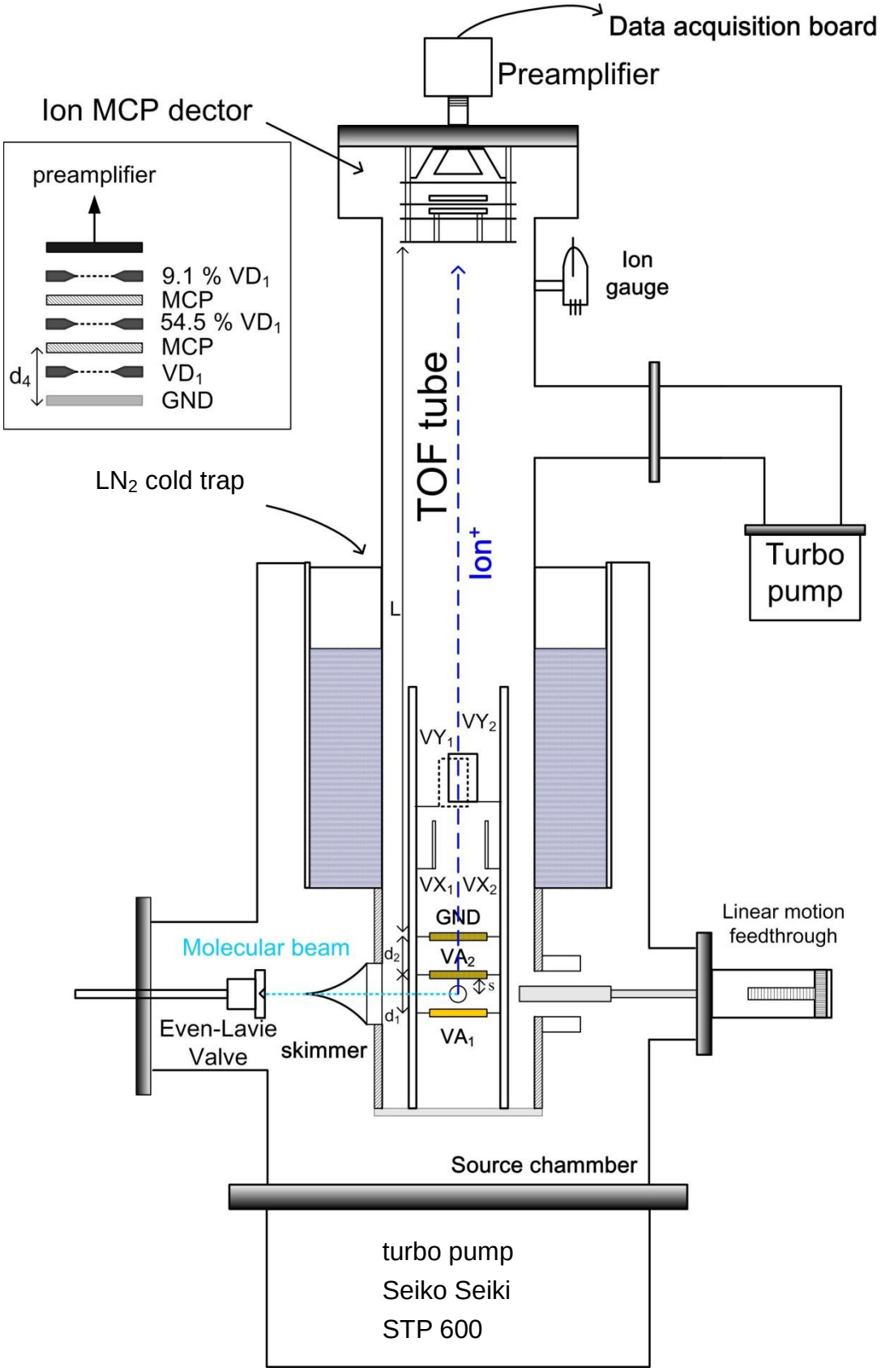


Figure 2-16 A schematic diagram of the time-of-flight spectrometer (TOF).

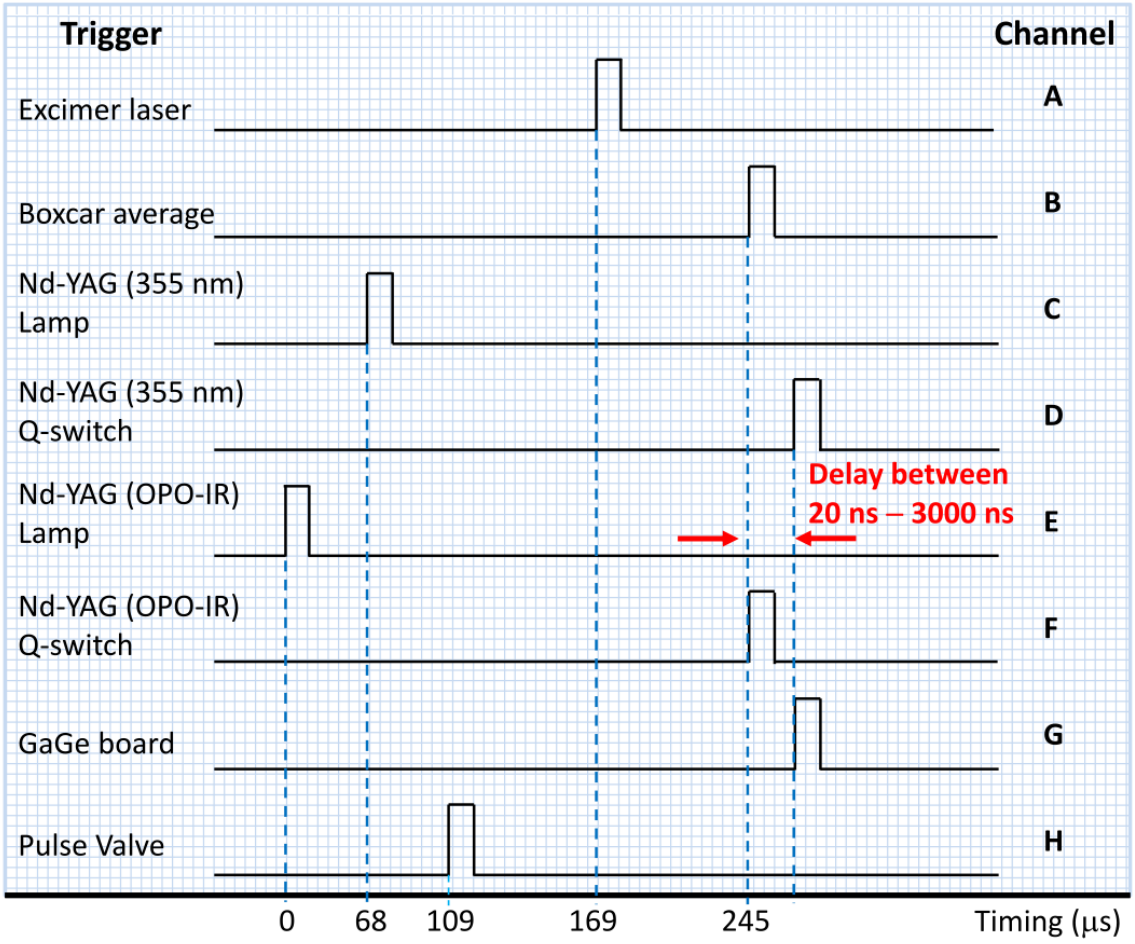


Figure 2-17 Typical timing sequence in the IR-VUV photoionization measurement. The time axis is not to scale and each device is triggered by the rise-edge.

**References**


[1] J. F. Ward and G. H. C. New, Phys. Rev. **185**, 57 (1969).

[2] G. C. Bjorklund, IEEE J. Quantum Electron. **QE-11**, 287 (1975).

[3] R. Mahon, T. J. McIlrath, V. P. Myerscough, and D. W. Koopman, IEEE J. Quantum Electron. **QE-15**, 444 (1979).

[4] S. E. Van Bramer and M. V. Johnston, Applied Spectroscopy **46**, 255 (1992).

[5] Y. R. Shen," The principle of nonlinear optics" (Wiley Classics Library Ed., John Wiley & Sons, New York, 2003).

[6] A. H. Kung, J. F. Young, and S. E. Harris, Appl. Phys. Lett. **22**, 301 (1973)

[7] Y. J. Shi, S. Consta, A. K. Das, B. Mallik, D. Lacey, and R. H. Lipson, J. Chem. Phys. **116**, 6990 (2002).

[8] L. J. Zych and J. F. Young, IEEE J. Quantum Electron. **QE-14**, 147 (1978).

[9] M. P. McCann, C. H. Chen, and M. G. Payne, J. Chem. Phys. **89**, 5429 (1988).

[10] M. W. Williams and E. T. Arakawa, Appl. Opt. **18**, 1477 (1979).

[11] R. Wallenstein, In Frontiers of Laser Spectroscopy of gases, edited by A. C. P. Alves, J. M. Brown, and J. M. Hollas, NATO Advanced Study Institute Series C **234**, 53 (1988).

[12] R. G. Tonkyn, J. W. Winniczek, and M. G. White, Chem. Phys. Lett. **164**, 137 (1989).

[13] H. H. Fielding and T. P. Softley, Chem. Phys. Lett. **185**, 199 (1991).

[14] G. Hilber, A. Lago, and R. Wallenstein, J. Opt. Soc. Am. B **4**, 1753 (1987).

[15] W. Kong, D. Rodgers and J. W. Hepburn, Chem. Phys. Lett. **203**, 497 (1993).

[16] R. T. Hodgson, P. P. Sorokin, and J. J. Wynnc, Phys. Rev. Lett. **32**, 343 (1974).

[17] W. Jamroz and B. P. Stoicheff, Progress in Optics **20**, 327 (1983).

[18] C. R. Vidal, In Tunable Lasers, Topics in Applied Physics, edited by L. F. Mollenauer and J . C. White, Springer, Heidelberg, 57 (1988).

[19] R. Hilig, G. Hilber, A. Lago, B. Woff, and R. Wallenstein, In Short Wavelength Coherent Radiation: Generation and Applications, edited by R. G. Lerner, AIP, New York, 382 (1986).

[20] K. Yamanouchi and S. Tsuchiya, J. Phys. B: At Mol. Opt. Phys. **28**, 133 (1995).

[21] R. Hilbig and R. Wallenstein, IEEE J. Quantum Electron. **QE-19**, 194 (1983).

[22] A. Lago, G.Hilber, and R. Wallenstein, Phys. Rev. A **36**, 3827 (1987).

[23] J. P. Marangos, N. Shen, H. Ma, M. H. R. Hutchinson, and J. P. Connerade, J. Opt. Soc. Am. B **7**, 1254 (1990).

[24] F. Brandi, W. Hogervorst, and W. Ubachs, J. Phys. B: At. Mol. Opt. Phys. **35**, 1071 (2002).

[25] Yu. Ralchenko, A.E. Kramida, J. Reader, and NIST ASD Team (2010). NIST Atomic Spectra Database (ver. 4.0.1), [Online]. Available: http://physics.nist.gov/asd. National Institute of Standards and Technology, Gaithersburg, MD.

[26] A. Miklós, P. Hess, and Z. Bozóki, Rev. Sci. Instrum. **72**, 1937 (2001).

[27] R. E. Smalley, B. L. Ramakrishna, D. H. Levy, and L. Wharton, J. Chem. Phys. **61**, 4363 (1974).

[28] C. Y. Ng, Anna. Rev. Phys. Chem. **53**, 101 (2002).

[29] U. Even, J. Jortner, D. Noy, N. Lavie, and C. Cossart-Magos, J. Chem. Phys. **112**, 8068 (2000).

[30] Makoto Kato, Akinori Mogami, and Motohiro Naito, Rev. Sci. Instrum. **59**, 1947 (1988).

# Chapter Three

# Infrared absorption of methanol clusters $(CH_3OH)_n$ with $n$ = 2–6 recorded with a time-of-flight mass spectrometer using IR depletion and VUV ionization

## 3.1 Introduction

Methanol is the simplest stable organic molecule having a hydrogen bond to form clusters. The investigations of hydrogen bonding in methanol clusters have attracted much attention; reviews on the infrared (IR) spectra and hydrogen-bond dynamics of methanol clusters are available.[1, 2] Vibrational spectra provide an important means to analyze the structures of hydrogen-bonded clusters and their intermolecular interactions; the vibrational wavenumbers associated with the OH-stretching mode reflect sensitively the local intermolecular interactions due to microsolvation.[3–5]

Numerous experiments of vibrational spectra of methanol clusters in the gaseous phase were performed to derive information about the structures and dynamics of intermolecular interactions. Direct IR absorption using a Fourier-transform infrared (FTIR) spectrometer[6–8] or a cavity-ring down laser absorption spectrometer,[9, 10] microwave spectra,[11, 12] and spontaneous Raman spectra[7, 13] of methanol clusters in supersonic jet expansion and IR absorption spectra of methanol clusters isolated in inert-gas matrices[14–17] are reported. Because clusters are typically generated with a distribution of sizes, without mass selection or a mass-specific measurement, spectra of larger clusters typically suffer from severe overlap

among various clusters.

Based on conventional IR photodissociation experiments,[18] several techniques were employed to provide mass selectivity. Huisken *et al*. and Buck *et al*. measured vibrational predissociation spectra in the OH-stretching region of $(CH_3OH)_n$ for $n \leq 9$ with a molecular-beam depletion method; in order to implement size selection they scattered the cluster beam with a beam of gaseous helium before ionizing the cluster beam with electron impact.[19–25] Zwier group recorded IR spectra of benzene-$(CH_3OH)_n$ clusters with $n$ = 1–6 in the OH- stretching[26] and with $n$ = 1–5 in the CH-stretching[27] regions by tuning the IR laser while using resonant enhanced multi-photon ionization (REMPI), in which the excitation of a suitable electronic state of a size-selected species is achieved at a specific wavelength, to detect the clusters. This method is applicable to molecules having an electronic state in the UV or visible region for REMPI (e.g. benzene) and is unsuitable for $(CH_3OH)_n$ clusters. Similarly, the IR-UV double-resonance[3, 28–30] and stimulated Raman-UV techniques[31–34] are difficult to apply for methanol clusters because the clusters of interest must have a chromophore in the UV or visible region for measurements of an electronic transition to detect the population transfer due to vibrational excitation.

The ionization energies of a large number of molecules and their clusters are typically in the vacuum-ultraviolet (VUV) region. Unlike REMPI, direct VUV ionization requires no intermediate state to absorb in the UV and visible region. Furthermore, VUV ionization with its photon energy near the ionization threshold of the cluster under investigation typically causes soft ionization without extensive fragmentation.[35–37] A combination of vibrational excitation and VUV photoionization with mass detection enables measurements of vibrational spectra of size-selected neutral clusters, as discussed in a recent review.[38] Ng and coworkers employed IR-VUV photoionization spectroscopy and IR-VUV pulsed field

ionization-photoelectron spectra to investigate the vibrational spectra of neutral molecules and cations.[39–43] Predissociation with IR laser emission might also result in variation of the population of the ion signal induced by VUV light,[44, 45] which Bernstein *et al*. termed nonresonant ionization and fragmentation detected infrared spectroscopy (NRIFD-IR) and applied to clusters of alcohols and organic acids.[46–49]

Bernstein and coworkers employed the VUV-ID-IRPDS method to investigate the IR spectra of jet-cooled $(CH_3OH)_n$ with $n \leq 8$ in regions 2500–4500 $cm^{-1}$ and 5000–7500 $cm^{-1}$.[46, 48] Their results demonstrate that the methanol dimer has IR absorption features corresponding to free and bonded OH-stretching modes, whereas clusters with $n \geq 3$ display only features of hydrogen bonded OH stretch, indicating that clusters with $n \geq 3$ have a cyclic structure. As this cyclic binding network do not involve directly the CH-stretching modes, the spectra in the CH-stretching region do not alter much with cluster size of modes, but the spectra that these authors reported reflect only the alteration of intensity of protonated methanol clusters ions upon IR laser irradiation at various wavenumbers, not the absorption spectra of $(CH_3OH)_n$.

We applied VUV photoionization and a time-of-flight (TOF) mass spectrometer to detect methanol clusters, and employed IR laser radiation, tuned through the 2650–3750 $cm^{-1}$ region, to photodissociate methanol clusters in a pulsed supersonic jet. By careful processing of action spectra according to photoionization efficiencies and the production and loss mechanism of each cluster, we derived IR spectra for the size-selected cluster.

## 3.2 Experiments

The principles of IR-VUV photoionization and the experimental setup of the 118 nm VUV laser/linear TOF mass spectrometer are similar to those reported previously.[46, 46, 49] A gaseous mixture of methanol and helium was supersonically expanded into a vacuum chamber through

a pulsed valve (Parker, General Valve Series 9 or Evan Lavie valve). Methanol clusters were formed during the adiabatic expansion through the nozzle. After passing through a skimmer (Beam Dynamics, Model 1, 1.0 mm diameter) the jet-cooled beam was introduced into the ionization region of the TOF mass spectrometer, which was 15 cm downstream from the nozzle. The pressures in the source and ionization chambers were $8\times10^{-5}$ and $7\times10^{-7}$ Torr, respectively, under typical operating conditions. Neutral clusters in a supersonic jet, softly ionized with little fragmentation by laser light at 118 nm, are detected with a linear TOF mass spectrometer. By monitoring the variation in intensity of each cluster ion while scanning the wavenumber of the IR laser, introduced before the VUV laser pulse, we derived the action spectra for each size-selected cluster.

The VUV laser emission at 118 nm serves as the ionization source. This emission was generated by frequency-tripling the 355 nm output of a Nd:YAG laser (Spectra Physics, GCR-230, 10 Hz, ~21 mJ pulse$^{-1}$) in a gas cell containing a mixture of Xe and Ar (1:10 at 80 Torr), which was attached directly to the ion source chamber of the time-of-flight mass system. A convex $MgF_2$ lens ($f$ = 15 cm) was mounted at the end of the gas cell to separate UV (355 nm) and VUV (118 nm) light through the difference in refraction index $n$ of the lens, $n$ (118 nm) ≅ 1.679 and $n$ (355 nm) ≅ 1.380.[50, 51] To minimize the multiphoton effects due to the intense 355 nm beam, the UV and VUV beams were spatially separated by ~5 mm in the horizontal plane near the ionization region.

The product ions were extracted perpendicularly with potential at 200 V and accelerated into a field-free tube of length 1 m. The accelerator and repeller plates of the ion optics were biased at 1500 V and 1700 V, respectively. Ions were subsequently detected with an 18 mm Chevron microchannel plate (MCP, Burle Electro-Optics). After amplification of the signal with a fast amplifier (EG&G ORTEC, Model 9306, bandwidth 1GHz), the TOF mass spectrum was recorded with a 14-bit digitizer (GaGe Instruments, Model CS8327, 100MS/s)

and also displayed on a digital oscilloscope. The tunable IR laser emission, generated from an OPO/OPA system (Laser Vision, resolution 1.8 $cm^{-1}$ with the broadband mode) pumped by the 1064 nm output of an injection-seeded Nd:YAG laser (Continuum, Powerlite 8000, 10 Hz, 360 mJ $pulse^{-1}$), was introduced into the ionization region and focused in a region of the molecular beam upstream from its intersection with the VUV beam. The distance between IR and VUV beam is typically 200 μm. The time delay between IR and VUV is about 200 ns. The intensity of the IR laser varies with wavelength; in the spectral range of 2700–3700 $cm^{-1}$ the energy before entering the ionization chamber typically increases from 1 mJ at 2700 $cm^{-1}$ to 4 mJ at 3200 $cm^{-1}$, then decreases slightly to 3.5 mJ near 3500 $cm^{-1}$. The fluence at the ionization region is about 1–4 mJ $mm^{-2}$ after mild focusing. In this paper, we use the average value, 2.5 mJ $mm^{-2}$ in this case, to indicate the fluence of the IR beam. For studies of power dependence, the average fluence varies from 1.0 to 4.0 mJ $mm^{-2}$.

The variation in intensity of each ion signal was monitored as the IR laser emission was tuned through the range 2650–3750 $cm^{-1}$. The energy of IR light was measured simultaneously as its frequency was tuned; observed action spectra were normalized with the variation in intensity of the IR laser. The wavelength of IR light was calibrated with the photoacoustic spectra of a reference gas ($CH_4$, $C_2H_2$, or $H_2O$) recorded simultaneously.

### 3.3 Computational Details

Vibrational frequencies for small methanol clusters $(CH_3OH)_n$ ($n$ = 1–3) have been computed using density functional theory (DFT) with the B3LYP exchange-correlation functional.[52, 53] Determination of anharmonic frequencies have been performed using second-order vibrational pertubation theory (VPT2)[54] and a full cubic and semidiagonal quartic force field obtained from numerical differentiation of analytical Hessian matrices[55, 56] as

implemented in the GAUSSIAN 09 quantum chemistry package.[57] The equilibrium geometries for all the species studied here have been optimized with very tight convergence criteria. Atomic natural orbitals (ANO1) basis sets of Almlöf *et al.*,[58] contracted as (8*s*6*p*4*d*)/[4*s*2*p*1*d*] for hydrogen and (13*s*8*p*6*d*4*f*)/[4*s*3*p*2*d*1*f*] for carbon and oxygen, has been adopted for the present work.

## 3.4 Results and Discussion

### 3.4.1 TOF Mass Spectrum of Methanol Clusters

A typical TOF mass spectrum of methanol clusters induced by VUV ionization at 118 nm (10.5 eV) is shown in Figure 3-1(a); assignments of mass peaks according to ratio of mass to charge are also indicated. Protonated methanol clusters $(CH_3OH)_nH^+$ ($n$ = 1–5) and dimeric ion $(CH_3OH)_2^+$ were observed. These protonated cluster ions are known to be generated from rapid proton-transfer reactions of an ionized molecule[59]

$$(CH_3OH)_n + h\nu \rightarrow (CH_3OH)_n^+ + e^- \rightarrow (CH_3OH)_{n-1}H^+ + CH_3O + e^- \quad (1)$$

The ionization energy (*IE*) of $CH_3OH$ and $(CH_3OH)_2$, and the appearance energies of $(CH_3OH)_{n-1}H^+$ from $(CH_3OH)_n$ ($n$ = 2–6) reported by Kostko *et al.* are 10.8, 9.8, 10.2, 10.1, 9.8, 9.8, 9.6 eV, respectively.[60] At 118 nm (10.5 eV), $CH_3OH$ cannot be ionized, whereas production of protonated cluster ions $(CH_3OH)_{n-1}H^+$ ($n$ = 2–6) are energetically accessible. The observation of $(CH_3OH)_2^+$ is also consistent with previous reports.[46] Possible fragments from these species are unobserved at $m/z$ = 15 ($CH_3^+$), 29 ($CHO^+$), or 31 ($CH_3O^+$/$CH_2OH^+$). Multiphoton processes involving 118 nm + 355 nm photons that cause the formation of $CH_3OH^+$ or its fragment ions are clearly negligible in our experiments. The $(CH_3OH)_3^+$ ion was observed following photoionization at 118 nm in a previous report when He served as a

carrier gas,[61] but was unobserved in our experiment. Cations corresponding to clusters $(CH_3OH)_n^+$ ($n \geq 4$) were unobserved, likely due to the instability of the ionized clusters and the efficient proton transfer that occurs upon photoionization. When Ar served as a carrier gas, $(CH_3OH)_3^+$ was also observed from ionization of methanol clusters adsorbed on the surface of large Ar clusters.[62] $(CH_3OH)_n^+$ ($n \leq 7$) were observed from ionization of $Ar_n(CH_3OH)_m$, the formation of these species is attributed to an indirect ionization of neutral heteroclusters via Penning ionization.[63]

Shi *et al.*[64] employed 118 nm VUV laser to ionize methanol clusters seeded in a He jet and detected daughter fragment ions produced from evaporative loss of methanol cluster ions in the acceleration region and the field-free drift tube; for the latter case the transit period of the daughter ions is greater than that of the parent ion. Using a similar experimental technique, Fu *et al*. demonstrated that the fraction of fragmentation of the parent ion $(CH_3OH)_nH^+$ ($2 \leq n \leq 7$) in the acceleration region is less than 8 %.[46] In our experiments, we found no evidence for further fragmentation of parent protonated ions upon ionization at 118 nm; the detected distribution of protonated cluster ions is hence correlated with the distribution of neutral clusters.

Figure 3-1(b) shows the TOF spectrum observed upon irradiating a beam of methanol clusters with the IR beam at 2950 $cm^{-1}$ 200 ns before irradiation of the VUV beam at 118 nm. All clusters $(CH_3OH)_n$ are expected to absorb infrared light at 2950 $cm^{-1}$. Differences between traces (a) and (b) of Figure 3-1 indicate that the intensities of mass peaks $(CH_3OH)_2^+$ and $(CH_3OH)_nH^+$ ($n$ = 1–5) in trace (a) decrease substantially, whereas signals due to $(CH_3OH)^+$ with $m/z$ = 32 and $(CH_3O)^+/CH_2OH^+$ with $m/z$ = 31 appear. The decrease in intensity of protonated methanol cluster ions with size $n$–1 indicates the destruction of the corresponding methanol clusters with size $n$ induced by IR photodissociation before ionization. The significant increase in intensity of $(CH_3OH)^+$ is due to the IR-VUV (1+1) ionization of

methanol monomer. In this case, methanol monomer is excited to vibrationally excited levels of the ground electronic state on absorbing an IR photon before being ionized by subsequent absorption of an VUV photon; the total energy of the IR + VUV photons, ~10.86 eV, exceeds the IE of $CH_3OH$, 10.8 ± 0.1 eV.[60]

Figure 3-1(c) shows the TOF spectrum observed upon irradiating a beam of methanol clusters with the IR laser beam at 3150 $cm^{-1}$ 200 ns before irradiation of the VUV beam at 118 nm. Only clusters $(CH_3OH)_n$ with $n \geq 4$ are expected to absorb infrared light at 3150 $cm^{-1}$. Differences between traces (a) and (c) of Figure 3-1 indicates that the intensities of $(CH_3OH)_nH^+$ ($n \geq 3$) in trace (a) decreases, that of $(CH_3OH)_2H^+$ increases due to increased number of $(CH_3OH)_3$ produced from dissociation of $(CH_3OH)_4$, whereas that of $(CH_3OH)H^+$ remains nearly constant.

On application of the IR excitation, we observed no additional daughter ion peak in the TOF spectrum, perhaps because no substantial energy was deposited into the remaining neutral clusters after predissociation induced by the IR light. The variation in concentration of neutral $(CH_3OH)_n$ clusters upon IR irradiation might hence be directly monitored through the variation in intensity of the $(CH_3OH)_{n-1}H^+$ signal.

### 3.4.2 Action Spectra as The IR Laser Is Turned

The initial TOF spectrum in the absence of IR irradiation in one set of experiment is shown in Figure 3-2(a) to indicate the initial distribution of clusters. In this TOF spectrum we control the stagnation pressure so that the largest protonated methanol cluster observed is $(CH_3OH)_4H^+$. On monitoring the intensity of each ion signal while scanning the wavelength of the IR laser, we recorded the variation of the relative population of each protonated methanol cluster $(CH_3OH)_nH^+$ ($n$ = 2–4), $(CH_3OH)_2^+$, and $CH_3OH^+$ as a function of IR wavenumber. For

$(CH_3OH)_2^+$ and $(CH_3OH)_nH^+$ ($n$ = 2–4) the observed signal was divided by the ion-signal level recorded with no IR excitation and then diminished by 1 to yield the fraction of variation; these spectra are indicated as $\Delta(CH_3OH)_2^+$ and $\Delta[(CH_3OH)_nH^+]$ and are shown in Figure 3-2(b) with ordinates indicating the fraction of variation; the negative signal indicates a decrease whereas the positive signal indicates an increase in population of these clusters when IR laser irradiation was employed. For $CH_3OH^+$, only the variation in intensity was plotted because the original signal was negligibly small in the absence of IR irradiation. These action spectra were recorded for various experimental conditions having a varied distribution of methanol clusters.

The signal of $CH_3OH^+$ shown in Figure 3-2 appears only when both IR and VUV laser irradiation was present, indicating that this signal is produced via IR-VUV (1+1) ionization of $CH_3OH$. The observed action spectrum in Figure 3-2 is expected to represent the IR spectrum of $CH_3OH$, if we assume that the ionization efficiencies for these vibrationally excited states are nearly identical at 118 nm. The features near 2845 $cm^{-1}$ are assigned as the symmetric CH-stretching band ($\nu_3$). The remaining complicated, unresolved features in the region 2900–3000 $cm^{-1}$ consist of several overtone bands ($2\nu_4$ at 2958 $cm^{-1}$ and $2\nu_5$ at 2916 $cm^{-1}$), the asymmetric CH-stretching bands ($\nu_2$ at 2995 and 3006 $cm^{-1}$ for E and $A_1$ symmetry and $\nu_9$ at 2952 and 2967 $cm^{-1}$ for E and $A_2$ symmetry), and combination bands (e.g. $\nu_4 + \nu_5$ at 2933 $cm^{-1}$).[65, 66]

Action spectra obtained from monitoring of $(CH_3OH)_3H^+$ and $(CH_3OH)_4H^+$ show only negative features in the 2700–3650 $cm^{-1}$ region, indicating a net decrease in concentration of $(CH_3OH)_4$ and $(CH_3OH)_5$ upon IR irradiation. In contrast, the spectrum of $(CH_3OH)_2H^+$ shows variation in concentration both ways; the efficiencies of formation of $(CH_3OH)_3$ from dissociation of $(CH_3OH)_4$ and destruction of $(CH_3OH)_3$ depends on the wavenumber of IR irradiation. Both $(CH_3OH)H^+$ and $(CH_3OH)_2^+$ are produced from $(CH_3OH)_2$; the intensities of both signals are expected to correlate with the population change of $(CH_3OH)_2$. The action

spectra obtained from monitoring of $(CH_3OH)H^+$ and $(CH_3OH)_2^+$, shown in Figure 3-2, have similar characteristic features for the CH-stretching region, but small differences in the OH-stretching region, 3400–3550 $cm^{-1}$, exist. According to Martrenchard *et al.*[67] and to Tsai *et al.*[68], the yield of $(CH_3OH)_2^+$ is much smaller than that of $(CH_3OH)H^+$ at 10.5 eV. Martrenchard *et al.* showed that, in their threshold photoelectron photoion coincidence (TPEPICO) experiments, no $(CH_3OH)H^+$ was observed below 10.1 eV; as soon as the $(CH_3OH)H^+$ appeared at 10.2 eV, the $(CH_3OH)_2^+$ peak decreased. One possible reason for the small discrepancy in the OH-stretching region of the action spectra obtained from monitoring of $(CH_3OH)H^+$ and $(CH_3OH)_2^+$ is that the yield of $(CH_3OH)_2^+$ relative to $(CH_3OH)H^+$ decreases as the total excitation energy increases.

### 3.4.3 IR Spectra of $(CH_3OH)_n$

As no daughter ion was observed, ion fragmentation is negligible; the intensity of $(CH_3OH)_{n-1}H^+$ thus correlats with the concentration of $(CH_3OH)_n$. Upon IR irradiation, dissociation of $(CH_3OH)_n$ to smaller clusters occurred; the variation of the concentration of $(CH_3OH)_n$ led to the variation of the intensity of $(CH_3OH)_{n-1}H^+$. We derived IR spectra of methanol clusters $(CH_3OH)_n$ from the action spectra by considering the dissociation mechanism and photoionization efficiencies.

A simplified scheme for dissociation and ionization of methanol clusters is shown in Figure 3-3. On absorption of an IR photon, methanol clusters $(CH_3OH)_n$ lose one methanol to become $(CH_3OH)_{n-1}$. Through employing an IR laser emission with small energy (< 8 mJ), multiphoton processes is expected to be unimportant. Following reaction (1), upon ionization at 118 nm, the ionized clusters $(CH_3OH)_n^+$ undergo proton transfer to eject $CH_3O$ and become protonated cluster ion $(CH_3OH)_{n-1}H^+$ with one less unit of methanol; some $(CH_3OH)_2^+$ survives.

As discussed previously, $CH_3OH$ does not ionize at 118 nm, but vibrationally excited $CH_3OH$, produced upon absorption of an IR photon, might ionize. Because the size of methanol clusters under investigation is small, the propagated error due to multiple dissociation steps is small.

The energies of the most stable structures for each cluster computed by Buck *et al.*[69] were used to derive the dissociation energy of clusters $(CH_3OH)_n$, $n$ = 2–6, to form $(CH_3OH)_{n-1}$ and $CH_3OH$; the dissociation energies are 0.278, 0.416, 0.674, 0.567, 0.532 eV, respectively, for $n$ = 2–6. According to the binding energies predicted by Hagemeister *et al*,[70] the dissociation energies for $n$ = 2–5 are 0.209, 0.426, 0.543, 0.382 eV, respectively. These reported dissociation energies deviate by ~30 %. The internal energy of $(CH_3OH)_n$ in a supersonic jet increases with $n$; values 0.223, 0.236, 0.311, 0.465, 0.647 eV for $n$ = 6–10 were derived from soft x-ray experiments.[71] The IR photons with wavenumbers 2800–3600 $cm^{-1}$ have energies 0.35–0.45 eV. Hence, with original internal energy and absorption of one photon of this IR light causes photodissociation of $(CH_3OH)_n$ to yield one methanol and $(CH_3OH)_{n-1}$, but unlikely to eliminate two or more methanol.

According to the scheme in Figure 3-3, we derived the IR spectrum of each methanol cluster by assuming that the size of the cluster only reduces by 1 upon absorption of the IR photon. Based on the PIE spectra of $(CH_3OH)_n$ reported by Kostko *et al.*[60] we assume that the efficiency for formation of $(CH_3OH)_nH^+$ ($n$ = 2–5) at 10.5 eV are the same because the employed energy of 10.5 eV is much greater than the threshold of the PIE spectra. However, for formation of $(CH_3OH)H^+$, because the PIE spectrum shows a small step from 10.2 to 10.8 eV before the efficiency increases rapidly with energy, we assume a smaller efficiency $\alpha$ relative to those for $(CH_3OH)_nH^+$ ($n$ = 2–5). Similarly, for formation of $(CH_3OH)_2^+$, an even smaller efficiency $\beta$ is assumed.

As shown in Figure 3-2, the largest cluster ion in the TOF spectrum is $(CH_3OH)_4H^+$, indicating that in that experiment the largest cluster detectable in the supersonic jet was

$(CH_3OH)_5$. The decrease in intensity of $(CH_3OH)_4H^+$ upon IR irradiation is due to only the dissociation of $(CH_3OH)_5$. The negative of the recorded action spectrum of $(CH_3OH)_4H^+$ thus represents the IR absorption spectrum of $(CH_3OH)_5$. The variation in concentration of $(CH_3OH)_{n-1}H^+$ ($n$ = 2–5) upon IR irradiation depends on the loss due to its dissociation and on the production of $(CH_3OH)_{n-1}H^+$ ($n$ = 2–5) due to dissociation of $(CH_3OH)_n$ ($n$ = 3–5). We use the observed initial peak height $a_n$ of $(CH_3OH)_{n-1}H^+$ ($n$ = 3–5) signals in the TOF spectrum recorded in the absence of IR irradiation to derive relative initial concentrations $c_n$ of $(CH_3OH)_n$ ($n$ = 3–5); $a_3/c_3 = a_4/c_4 = a_5/c_5$. For $(CH_3OH)_2$, because of its low efficiency in ionization at 10.5 eV discussed previously, the peak height $a_2$ of $(CH_3OH)H^+$ is represented by $\alpha c_2(a_3/c_3)$ and the peak height $a_2'$ of $(CH_3OH)_2^+$ by $\beta c_2(a_3/c_3)$, in which α and β are the efficiency for formation of $(CH_3OH)H^+$ and $(CH_3OH)_2^+$, respectively.

The absorption spectra, $A[(CH_3OH)_n]$, for each clusters are derived according to the following equations:

$$A[(CH_3OH)_5] = -\Delta[(CH_3OH)_4H^+], \quad (2)$$

$$A[(CH_3OH)_4] = -(\Delta[(CH_3OH)_3H^+] - A[(CH_3OH)_5] \times a_5/a_4), \quad (3)$$

$$A[(CH_3OH)_3] = -(\Delta[(CH_3OH)_2H^+] - A[(CH_3OH)_4] \times a_4/a_3), \quad (4)$$

$$A[(CH_3OH)_2] = -(\Delta[(CH_3OH)H^+] - A[(CH_3OH)_3] \times \alpha a_3/a_2), \quad (5)$$

or, alternatively, when the action spectrum of $(CH_3OH)_2$ is used,

$$A[(CH_3OH)_2] = -(\Delta[(CH_3OH)_2^+] - A[(CH_3OH)_3] \times \beta a_3/a_2'), \quad (6)$$

in which $\Delta[(CH_3OH)_nH^+]$ are action spectra showing fractional variations in intensity, $a_2'$, $a_2$–$a_5$ are peak intensities of $(CH_3OH)_2^+$, $(CH_3OH)_nH^+$ ($n$ = 1–4) signals in the TOF spectrum recorded in the absence of IR irradiation, respectively, and α and β are fitting parameters that reflect the ionization efficiency. The absorption spectra of $(CH_3OH)_n$ ($n$ = 2–5) were derived directly according to equations (2)–(4), as shown in Figure 3-4. As we expect no absorption of

$(CH_3OH)_2$ in the region 3100–3400 $cm^{-1}$, we varied α and β in equation (5) and (6), respectively, to obtain the best fit that shows a flat baseline the region 3100–3400 $cm^{-1}$. For the set of data presented in Figure 3-2, we employed α = 0.4 and β = 0.055 to yield two similar spectra of $(CH_3OH)_2$, as shown in Figure 3-4. The spectrum of $CH_3OH$ was obtained by directly monitoring $(CH_3OH)^+$.

In the PIE spectra of $(CH_3OH)_n$ reported by Kostko *et al*,[60] observed ion intensity ratio of $(CH_3OH)_2H^+$ to $(CH_3OH)H^+$ is about 2.16 at an ionization potential of 12.0 eV, whereas the ratio increases to 4.37 at an ionization potential of 10.5 eV. Assuming that the ionization efficiency of both $(CH_3OH)_3$ and $(CH_3OH)_2$ clusters at 12.0 eV are similar because the energy is much greater than the ionization threshold, we can estimate the ionization efficiency for formation of $(CH_3OH)H^+$ relative to that of $(CH_3OH)_2H^+$ to be 0.4–9. This value is in satisfactory agreement with the value of α = 0.40 employed in the analysis described in the preceding paragraph.

We performed several sets of experiments using various conditions (type of nozzle, concentration, and stagnation pressure) and obtained similar spectra for each specific methanol cluster. We also performed power dependence studies and some resultant spectra for $(CH_3OH)_4$ and $(CH_3OH)_5$ are shown in Figure 3-5. In this set of experiment, a mixture of $CH_3OH$/He = (3/100) at a stagnation pressure of 1670 Torr and a Evan Lavie valve were employed so that the dominant cluster is $(CH_3OH)_4$, with relatively small proportion of $(CH_3OH)_n$, $n \geq 5$. As the average fluence was increased from 2.5 to 4.0 mJ $mm^{-2}$, the FWHM (full width at half maximum) of the broad OH-stretching band increased from 190 to 224 $cm^{-1}$ for $(CH_3OH)_4$ and from 271 to 307 $cm^{-1}$ for $(CH_3OH)_5$. Similarly, the FWHM of the $\nu_3$ band near 2830 $cm^{-1}$ increased from 34 to 38 $cm^{-1}$ for $(CH_3OH)_4$ and from 33 to 44 $cm^{-1}$ for $(CH_3OH)_5$. Further decrease of the average fluence to 1 mJ $mm^{-2}$ resulted in poor signal-to-noise ratio, but the FWHM of the $\nu_3$ band remained ~34 $cm^{-1}$, whereas the FWHM

of the OH-stretching band decreased to 144 $cm^{-1}$. The power broadening in the CH-stretching region is less severe and becomes nearly negligible for average fluence less than 2.5 mJ $mm^{-2}$ because the energy employed in this region are 2–3 times smaller than that employed in the OH-stretching region.

One would expect that the spectrum of $(CH_3OH)_4$ derived from this set of experiment shown in Figure 3-5 is reliable because of little contamination from absorption of higher clusters. This spectrum is similar to that shown in Figure 3-4, indicating the validity of our model. For comparison, a spectrum of $(CH_3OH)_6$ is also listed in Figure 3-4. This spectrum was obtained from another set of experiment in which a mixture of $CH_3OH$/He = (1/100) at a stagnation pressure of 800 Torr was employed so that $(CH_3OH)_6$ was the largest cluster detectable in the supersonic jet, Spectra of $(CH_3OH)_n$, $n \leq 5$, obtained from this set of experiment are also similar to those shown in Figure 3-4.

### 3.4.4 Spectral Assignments and Comparisons

The OH-stretching region of methanol clusters is well studied. In our experiment the feature in this region shifts from 3683 $cm^{-1}$ for $CH_3OH$ to 3675 and 3576 $cm^{-1}$ for $(CH_3OH)_2$; broad features with maxima near 3473 $cm^{-1}$ for $(CH_3OH)_3$, 3300 $cm^{-1}$ for $(CH_3OH)_4$, 3240 $cm^{-1}$ for $(CH_3OH)_5$, and 3210 $cm^{-1}$ for $(CH_3OH)_6$ were observed. Our experimental results in general agree with those in previous experimental reports[6, 9, 21, 22, 25] and quantum-chemical computations;[9, 69, 70, 72–75] some representative results are listed in Table 3-1.

For $(CH_3OH)_2$, the two features of OH-stretching near 3675 and 3576 $cm^{-1}$ correspond to proton acceptor (PA) and proton donor (PD). Observed wavenumber of PD is consistent with those reported in other experiments, but that of PA is about 9 $cm^{-1}$ smaller than that reported previously.[9, 21, 22] Previously reported values are close to that of the monomer, likely the

observation was interfered by absorption of the monomer. The $\nu_{OH}$ of PA and PD were red-shifted by 8 $cm^{-1}$ and 107 $cm^{-1}$ from that of monomer, respectively, in agreement with shifts of –8 $cm^{-1}$ and –144 $cm^{-1}$ for conformer A of $(CH_3OH)_2$ from the band at 3664 $cm^{-1}$ of $CH_3OH$ in a $N_2$ matrix.[17] Observed shifts are also in satisfactory agreements with the theoretical anharmonic vibrational wavenumbers of –26 and –146 by Buck et al,[69] and –11 and –146 $cm^{-1}$ as predicted with the B3LYP/VPT2 and an ANO1 basis set in this work.

For $(CH_3OH)_3$, the OH-stretching band becomes much broader with a maximum near 3473 $cm^{-1}$. The anharmonic vibrational wavenumbers 3482, 3511, and 3519 $cm^{-1}$ predicted by Buck *et al*.[69] and the values 3345, 3408, and 3422 $cm^{-1}$ predicted in this work are all within the broad contour of this experimentally observed band. The absence of absorption near the free OH-stretching region ~3670 $cm^{-1}$ for $(CH_3OH)_n$, $n$ = 3–6 is consistent with reported computation results that indicate the most stable structure of $(CH_3OH)_n$, $n \geq 3$ to be cyclic.[23, 48, 69, 70, 73, 76, 77] The increased red shifts and width of OH-stretching fundamentals as $n$ increases might indicate that the cooperative effect[74, 78–80] is enhanced as the size of the cluster increases,[81] even though we cannot positively eliminate the possible contribution of power broadening in our experiments.

The CH-stretching region of methanol clusters between 2800 and 3050 $cm^{-1}$ is little studied because of the severe overlap of bands of each cluster. Hu *et al*. reported action spectra of protonated methanol clusters $(CH_3OH)_{n-1}H^+$ in the region 2500–3800 $cm^{-1}$ (Figure 3 of Ref. 48) and treated them as IR absorption spectra of $(CH_3OH)_n$. The absorption spectra derived in the present work are significantly different from the corresponding action spectra, especially for $(CH_3OH)_2$ and $(CH_3OH)_3$. Although most main features identified by Hu *et al*. are within 16 $cm^{-1}$ of our results, our results are expected to be more reliable because the mechanisms for loss and production of each cluster have been taken into account in our work; the results of Hu *et al*. are likely contaminated by those of higher clusters. The observed vibrational

wavenumbers in the CH-stretching region are compared in Table 3-2 with representative computational values reported in the literature.

For $(CH_3OH)_2$ in the region 2850–3050 $cm^{-1}$, each band of $CH_3OH$ splits into two components corresponding to PD and PA, consistent with those reported for $(CH_3OH)_2$ isolated in solid Ar or $N_2$.[15, 16] Assuming that the splitting between PA and PD in the CH-stretching region is small, we tentatively assign features at 2849 (PA) and 2823 (PD) $cm^{-1}$ as $\nu_3$, 2954 (PA) and 2934 (PD) $cm^{-1}$ as $\nu_9$, 3006 (PA) and 2984 (PD) $cm^{-1}$ as $\nu_2$, and the broad feature with maximal intensity near 2920 $cm^{-1}$ as unresolved combination and overtone bands of $\nu_4 + \nu_5$, $2\nu_4$, and $2\nu_5$. These values are consistent with results of $(CH_3OH)_2$ isolated in solid $N_2$; features near 2828.1, 2945.4, and 2987.3 $cm^{-1}$ are assigned as $\nu_3$, $\nu_9$, and $\nu_2$ of the PD, respectively, and those near 2853.9, 2970.7, and 3012.2 $cm^{-1}$ are assigned as the corresponding modes of the PA of $(CH_3OH)_2$.[16] The splitting between PA and PD for these three CH-stretching modes ($\nu_3$, $\nu_9$, and $\nu_2$) are 22, 21, and 22 $cm^{-1}$ in our experiments, in agreement with corresponding values of 25.8, 25.3, and 24.9 $cm^{-1}$ reported for $(CH_3OH)_2$ in solid $N_2$.

As shown in Table 3-2, the presented B3LYP/ANO1 harmonic vibrational frequencies of $(CH_3OH)_2$ and $(CH_3OH)_3$ are in good correspondence with the previous results of Mó *et al.*,[72] revealing the largest discrepancy of only 4 $cm^{-1}$ in the CH stretching region. No anharmonic results are available in previous literature. Although the predicted splitting for $\nu_3$, $\nu_9$, and $\nu_2$ of PA and PD (126, 59, and 40 $cm^{-1}$, respectively) of $(CH_3OH)_2$ are significantly different from our observed values, if we ignore the original assignments based on small splitting of PA and PD the predicted wavenumbers of these six lines are in satisfactory agreement with our experimental values. If we assume a good correspondence of experimental results to the anharmonic calculations, we might assign 2955 (PA) and 2765 (PD) $cm^{-1}$ as $\nu_3$, 2934 (PA) and 2838 (PD) $cm^{-1}$ as $\nu_9$, 3006 (PA) and 2984 (PD) $cm^{-1}$ as $\nu_2$. Large anharmonic corrections and significantly altered $\nu_2$, $\nu_3$, and $\nu_9$ splitting pattern for the dimer indicates that anharmonicity

constitutes an important factor to assign properly the observed vibrational spectra of methanol clusters.

In contrast to $(CH_3OH)_2$, bands in $(CH_3OH)_3$ become narrower and the splitting diminishes. We assign features at 2837, 2954 and 2987 $cm^{-1}$ to $\nu_3$, $\nu_9$ and $\nu_2$ of $(CH_3OH)_3$. This spectral observation is consistent with a prediction that the cyclic conformer is the most stable and is the major contributor of the observed spectrum. In a cyclic conformer, each $CH_3OH$ unit is both PD and PA. The B3LYP/VPT2/ANO1 calculations of the anharmonic vibrational wavenumbers for $\nu_3$, $\nu_9$ and $\nu_2$ of $(CH_3OH)_3$ also indicate splitting of only 17, 3, and 5 $cm^{-1}$, with the central lines at 2842, 2918, and 2970 $cm^{-1}$, respectively, which is consistent with our observation.

Spectra of $(CH_3OH)_n$, $4 \le n \le 6$ are similar to that of $(CH_3OH)_3$ except that the band widths increase with $n$, also supporting that the most stable form of these clusters is cyclic. Features shifted slightly from 2837 to 2834 to 2830 $cm^{-1}$ for $\nu_3$ and from 2987 to 2985 to 2983 $cm^{-1}$ for $\nu_2$; bands of $\nu_9$ become overlapped with other combination and overtone bands. The increased width might be partly due to the increased number of vibrational modes with slightly different wavenumbers, and partly due to the increased number of low-wavenumber vibrational modes that contribute to the combination and overtone bands.

Theoretical analysis by Mandado *et al.*[79] on the charge densities of the dimer and the trimer according to the AIM theory indicates that the methyl groups also play a significant role in the stabilization of these clusters. Gruenloh *et al.*[27] showed also that CH-stretching vibrations of the methyl groups in clusters $C_6H_6$-$(CH_3OH)_n$ ($n$ = 1–5) shift toward the red as $n$ increases due to the H-bonding arrangement for each methanol in the cluster.

Although the CH-stretching modes of methanol are not involved directly in the hydrogen-bonding of the cluster, our observation of significant variations in action spectra in this region indicates that the excitation energy of these modes flows rapidly into the interaction

network of H-bonding through energy redistribution and might result in cluster dissociation.

## 3.5 Conclusion

We investigated IR absorption in the 2700–3700 $cm^{-1}$ region of size-selected methanol clusters, $(CH_3OH)_n$ with $n \leq 6$, in a pulsed supersonic jet with the IR-VUV ionization TOF mass technique. The observed signals of $(CH_3OH)_nH^+$ correlate with concentrations of $(CH_3OH)_n$. Through careful processing of observed action spectra based on the mechanism for production and loss of each cluster due to predissociation, we derived a set of IR spectra of size-selected methanol clusters consistent under diverse experimental conditions. The spectra in the OH-stretching region are consistent with previous reports, except that the wavenumber of the proton donor of $(CH_3OH)_2$ is clearly identified at 3675 $cm^{-1}$. The spectra in the CH-stretching region are new. For $(CH_3OH)_2$ in the region 2800–3050 $cm^{-1}$, each absorption feature of $CH_3OH$ splits into two components that correspond to PD and PA, indicating that methanol dimer has a preferred open-chain structure. In contrast, for $(CH_3OH)_3$, the splitting diminishes and the bands become narrower, indicating a preferred cyclic structure as predicted by theory. For $(CH_3OH)_n$ with $n \geq 4$, the spectral pattern remains similar to those of $(CH_3OH)_3$ but the band widths are greater, supporting that the most stable structures are also cyclic as predicted theoretically. Although the CH-stretching modes are not directly involved in the hydrogen bonding of the cluster, the fact that absorption in the CH region also results in dissociation of clusters indicates that energy redistribution is rapid.

Table 3-1 Comparison of experimental IR absorption wavenumbers (in $cm^{-1}$) in the OH-stretching region with theoretical results.

| $(CH_3OH)_n$ | | Experiments | | | | |
|---|---|---|---|---|---|---|
| *n* | group | IR-VUV /TOF[a] | IR-VUV /TOF[b] | Cavity Ringdown | He scattering | FITR absorption |
| 1 | | 3683 | 3684 | — | — | 3686 |
| 2 | PA[d] | 3675 | 3679 | 3683.8 | 3684.1 | — |
| | PD[d] | 3576 | 3576 | 3574.4 | 3574.4 | 3575 |
| 3[e] | | 3473 | 3515 | 3503.7 | 3503.4 | 3502 |
| | | | | 3494.6 | | 3495 |
| | | | | 3473.2 | 3471.8 | 3474 |
| | | | | 3467.1 | | 3469 |
| | | | | 3432.1 | 3433.6 | 3434 |
| | | | | | | 3413 |
| 4 | | 3300 | 3339 | 3278.5 | | 3293 |
| 5 | | 3240 | 3302 | | | |
| reference | | this work | 48 | 9 | 21, 22 | 6 |

[a] From our derived absorption spectra. For *n* = 3–5, maxima of unresolved bands are listed. [b] Peaks observed in action spectra of protonated methanol clusters $(CH_3OH)_{n-1}H^+$; see text. [c] Anharmonic approximation using a perturbation method. [d] PA: proton acceptor, PD: proton donor. [e]Bands near 3469 and 3474 $cm^{-1}$ are assigned to the OH-stretching mode; other bands are attributed to sum, difference, or hot bands involving the OH-stretching and two umbrella modes of methyl group. See Ref. 7.

| Theory | | | | |
|---|---|---|---|---|
| harmonic | | | anharmonic | |
| B3LYP /6-31+G* | B3LYP /6-3111+G(d,p) | B3LYP/ ANO1 | Cluster PES[c] | B3LYP /VPT2/ANO1 |
| 3763 | 3846 | 3839 | 3682 | 3666 |
| 3759 | 3843 | 3834 | 3656 | 3655 |
| 3613 | 3691 | 3680 | 3536 | 3520 |
| 3535 | 3612 | 3597 | 3479 | 3422 |
| 3521 | 3 600 | 3587 | 3511 | 3408 |
| 3465 | 3546 | 3527 | 3482 | 3355 |
| 3429, 3392 | | | 3418 | |
| 3392, 3301 | | | 3401 | |
| 3405 | | | 3379 | |
| 3348 | | | 3368 | |
| 3392 | | | 3353 | |
| 3338 | | | 3346 | |
| 3259 | | | 3320 | |
| 70 | 72 | this work | 69 | this work |

Table 3-2 Comparison of experimental IR absorption wavenumbers (in $cm^{-1}$) in the CH-stretching region with theoretical results.

| | | Experiments | | | | | |
|---|---|---|---|---|---|---|---|
| $(CH_3OH)_n$ | | IR-VUV/TOF[a] | | | IR-VUV/TOF[b] | | |
| | | $\nu_3$ | $\nu_9$ | $\nu_2$ | $\nu_3$ | $\nu_9$ | $\nu_2$ |
| 1 | | 2845 | 2956 | 3007 | 2837 | 2956 | 3010 |
| 2[d] | PA[c] | 2849 | 2955 | 3006 | | | |
| | PD[c] | 2823 | 2934? | 2984 | | | |
| 3 | | 2837 | 2954 | 2987 | 2832 | 2954 | 2995 |
| 4 | | 2834 | 2951 | 2985 | 2839 | 2951 | 2996 |
| 5 | | 2830 | 2945 | 2983 | 2838 | 2945 | 2995 |
| reference | | this work | | | | 48 | |

[a] From our derived absorption spectra. [b] Peaks observed in action spectra of protonated methanol clusters $(CH_3OH)_{n-1}H^+$. [c] PA: proton acceptor. PD: proton donor. [d] Assignments are tentative; see text.

| Theory | | | | | | | | |
|---|---|---|---|---|---|---|---|---|
| harmonic | | | | | | anharmonic | | |
| B3LYP/6-311G(*d*,*p*) | | | B3LYP/ANO1 | | | B3LYP/VPT2/ANO1 | | |
| $\nu_3$ | $\nu_9$ | $\nu_2$ | $\nu_3$ | $\nu_9$ | $\nu_2$ | $\nu_3$ | $\nu_9$ | $\nu_2$ |
| | | | 2992 | 3036 | 3109 | 2891 | 2917 | 2972 |
| 3011 | 3069 | 3128 | 3013 | 3068 | 3125 | 2940 | 2935 | 2997 |
| 2973 | 3013 | 3091 | 2977 | 3015 | 3090 | 2814 | 2876 | 2957 |
| 2999 | 3050 | 3107 | 3002 | 3051 | 3105 | 2849 | 2921 | 2970 |
| 2995 | 3046 | 3106 | 2999 | 3047 | 3105 | 2842 | 2918 | 2970 |
| 2994 | 3044 | 3104 | 2997 | 3046 | 3102 | 2832 | 2918 | 2965 |
| 72 | | | this work | | | this work | | |

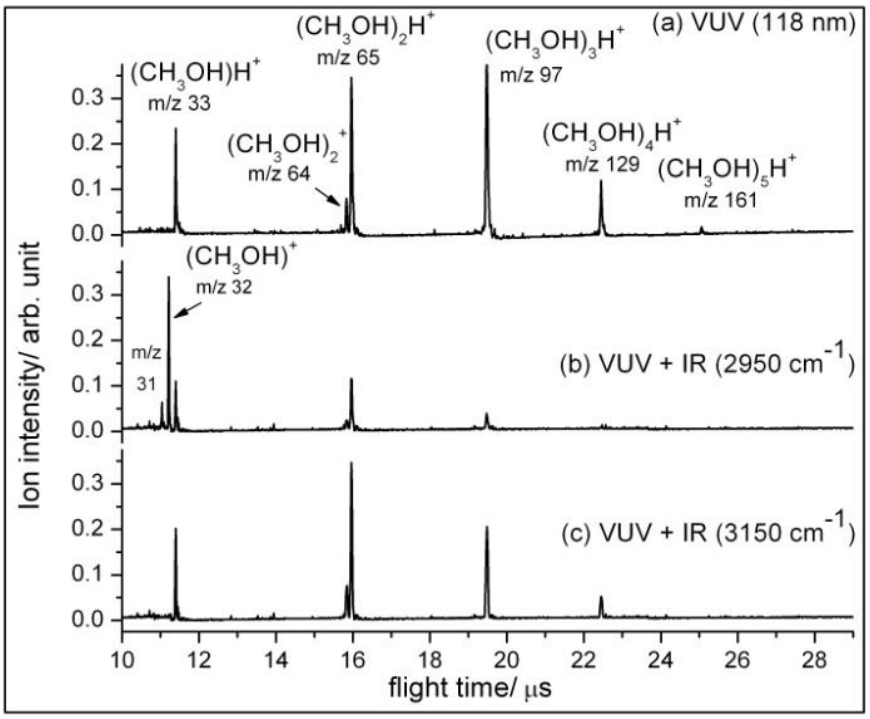


Figure 3-1 Time-of-flight mass spectra of a jet-cooled methanol cluster beam produced from a mixture of $CH_3OH$/He = (1/100) at a stagnation pressure of 850 Torr. (a) ionization at 118 nm; (b) IR irradiation at 2950 $cm^{-1}$ applied 200 ns before ionization at 118 nm; (c) IR irradiation at 3150 $cm^{-1}$ applied 200 ns prior to ionization at 118 nm. The *m*/*z* values for $(CH_3OH)_nH^+$ and $(CH_3OH)_n^+$ are indicated.

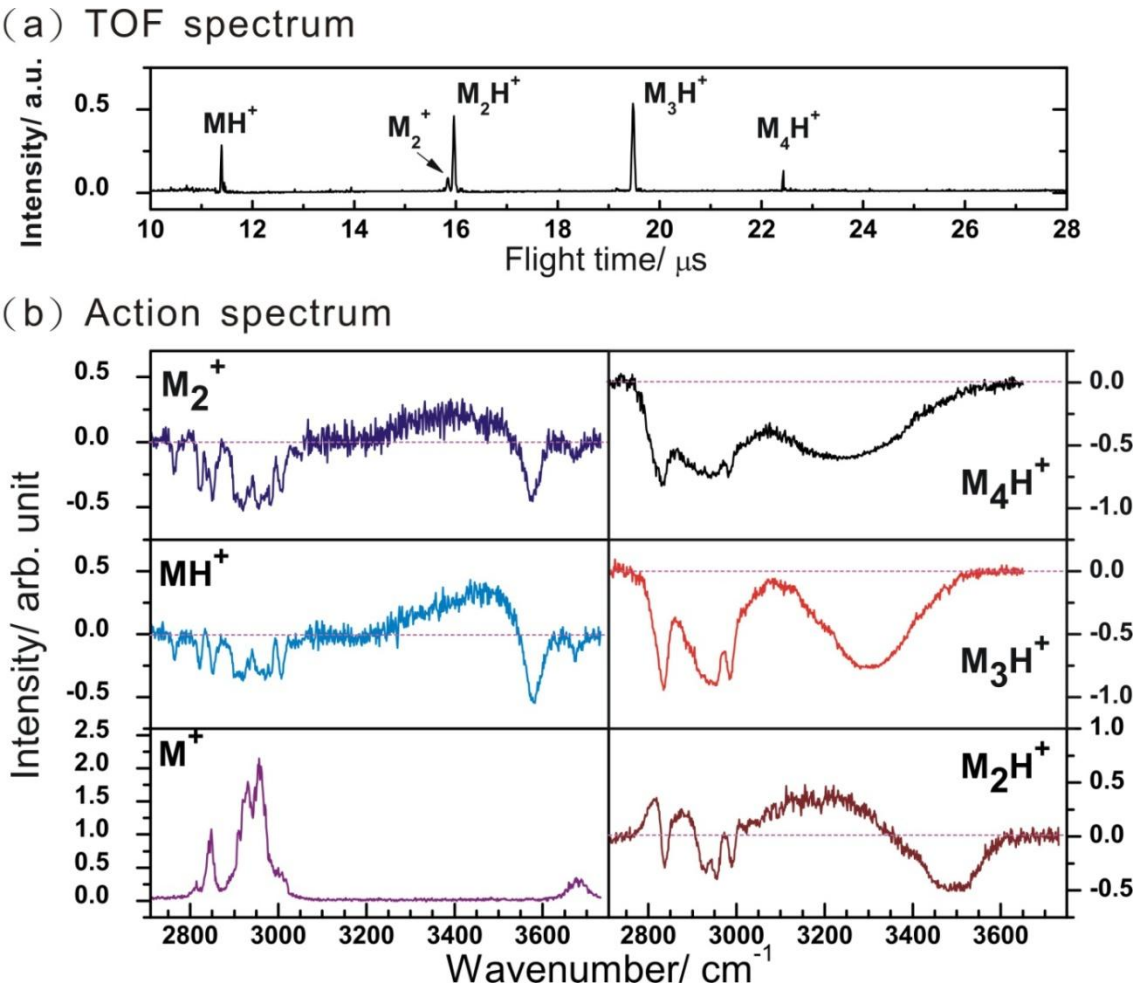


Figure 3-2 Time-of-flight mass spectra (a) and action spectra (b) of a jet-cooled methanol cluster beam produced from a mixture of $CH_3OH$/He = (5/1000) at a stagnation pressure of 800 Torr. The action spectra were recorded on monitoring the fractional variations in intensity of each mass channel as the wavelength of the IR laser was scanned.

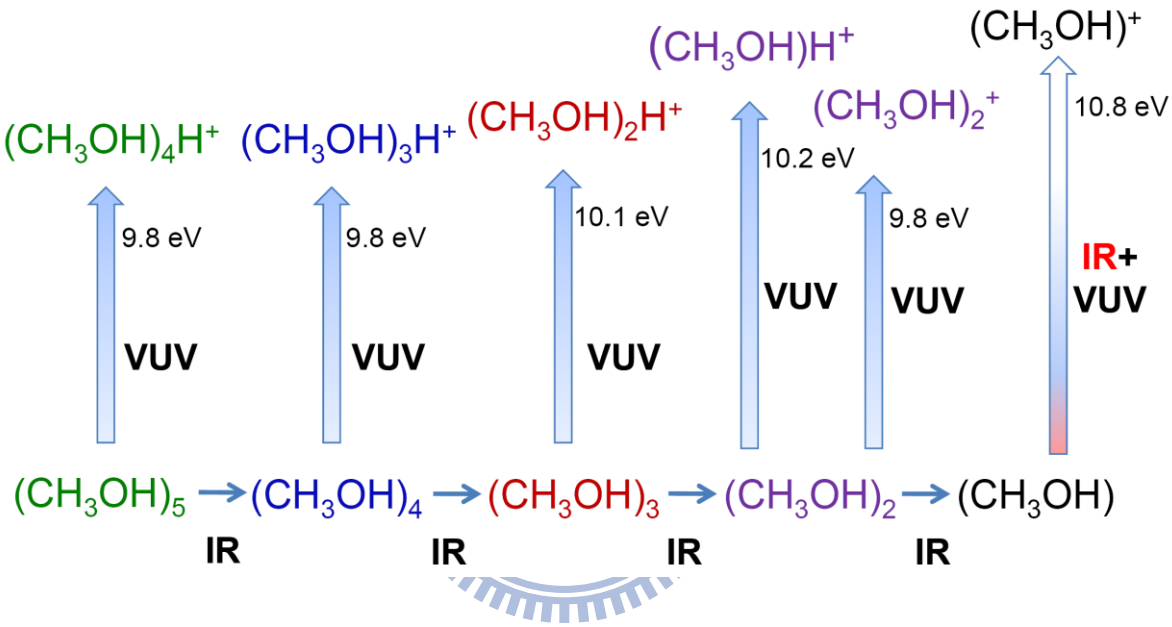


Figure 3-3 Reaction and ionization scheme of methanol clusters.

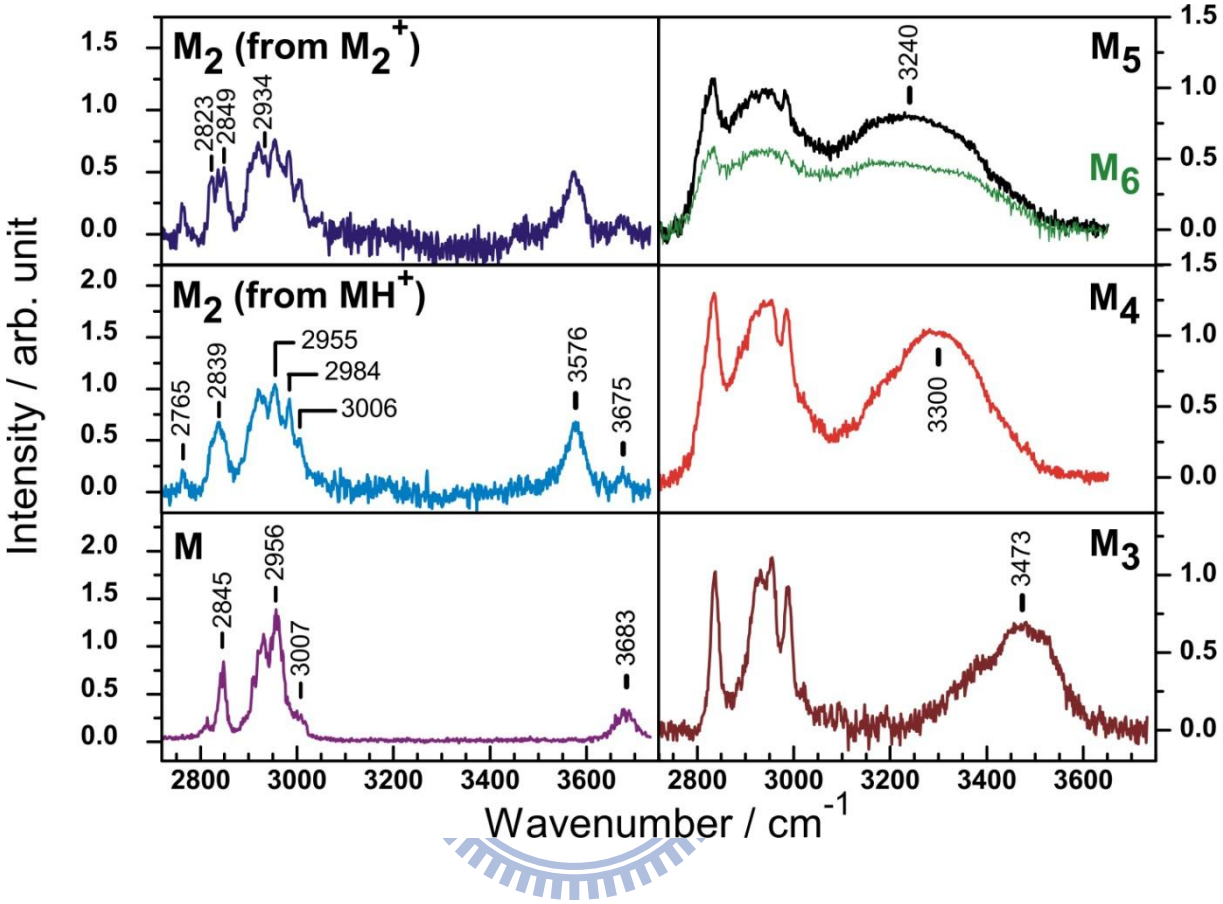


Figure 3-4 Infrared spectra of $(CH_3OH)_n$ for n =1–5 derived from action spectra shown in Figure 3-2 according to the dissociation and ionization mechanisms described in text. M indicates $CH_3OH$. The spectrum of $M_6$ was obtained in a separate experiment in which $(CH_3OH)_6$ has a higher concentration.

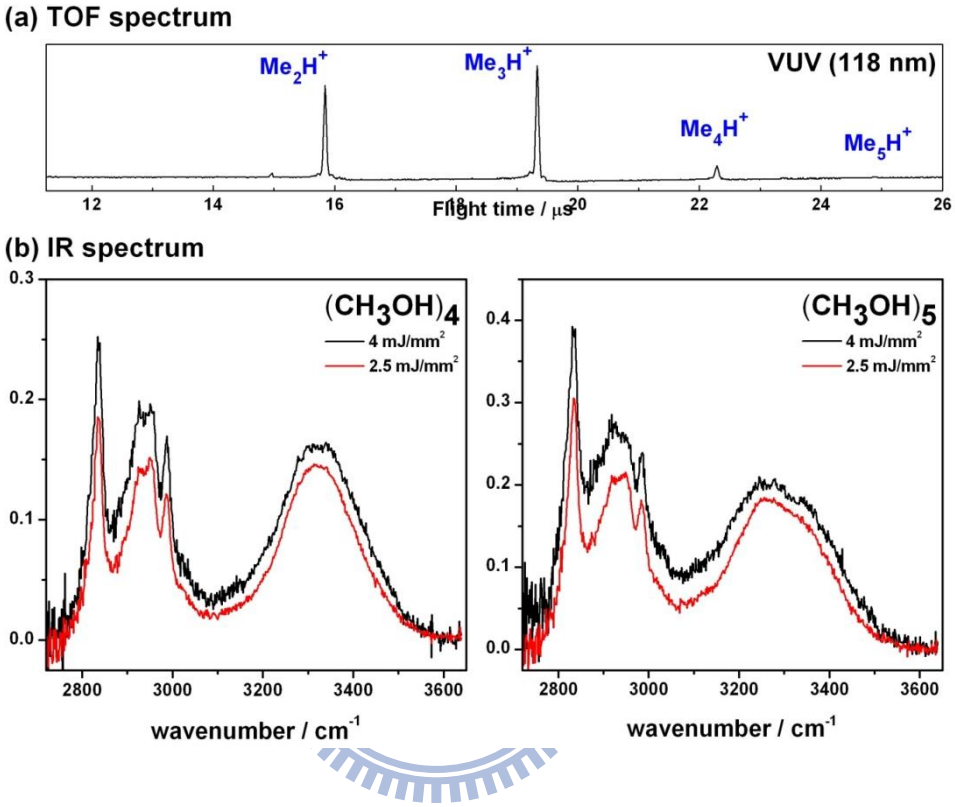


Figure 3-5 Time-of-flight mass spectra (a) of a jet-cooled methanol cluster beam, produced from a mixture of $CH_3OH$/He = (3/100) at a stagnation pressure of 1670 Torr, and IR spectra (b) of $(CH_3OH)_4$ and $(CH_3OH)_5$ obtained with the fluence of IR radiation at 4 and 2.5 mJ $mm^{-2}$.

## References


[1] U. Buck and F. Huisken, *Chem. Rev.* **100**, 3863 (2000).

[2] M. A. Suhm, *Adv. Chem. Phys.* **142**, 1 (2009).

[3] T. S. Zwier, *Annu. Rev. Phys. Chem.* **47**, 205 (1996).

[4] J. J. Scherer, J. B. Paul, A. O'Keefe and R. J. Saykally, *Chem. Rev*. **97**, 25 (1997).

[5] W. H. Robertson and M. A. Johnson, *Annu. Rev. Phys. Chem.* **54**, 173 (2003).

[6] T. Häber, U. Schmitt and M. A. Suhm, *Phys. Chem. Chem. Phys.* **1**, 5573 (1999).

[7] R. W. Larsen, P. Zielke, and M. A. Suhm, *J. Chem. Phys.* **126**, 194307 (2007).

[8] R. W. Larsen and M. A. Suhm, *J. Chem. Phys.* **125**, 154314 (2006).

[9] R. A. Provencal, J. B. Paul, K. Roth, C. Chapo, R. N. Casaes, R. J. Saykally, G. S. Tschumper, and H. F. Schaefer Ⅲ, *J. Chem. Phys.* **110**, 4258 (1999).

[10] R. A. Provencal, R. N. Casaes, K. Roth, J. B. Paul, C. N. Chapo, R. J. Saykally, G. S. Tschumper, and H. F. Schaefer Ⅲ, *J. Phys. Chem. A* **104**, 1423 (2000).

[11] F. J. Lovas, S. P. Belov, M. Yu. Tretyakov, W. Stahl, and R. D. Suenram, *J. Mol. Spectrosc.* **170**, 478 (1995).

[12] F. J. Lovas and H. Hartwig, *J. Mol. Spectrosc.* **185**, 98 (1997).

[13] P. Zielke and M. A. Suhm, *Phys. Chem. Chem. Phys*. **8**, 2826 (2006).

[14] S. Coussan, A. Loutellier, J. P. Perchard, S. Racine, A. Peremans, A. Tadjeddine, and W. Q. Zheng, *J. Chem. Phys*. **107**, 6526 (1997).

[15] S. Coussan, Y. Bouteiller, A. Loutellier, J. P. Perchard, S. Racine, A. Peremans, W. Q. Zheng, and A. Tadjeddine, *Chem. Phys*. **219**, 221 (1997).

[16] S. Coussan, A. Loutellier, J. P. Perchard, S. Racine, A. peremans, A. Tadjeddine, W. Q. Zheng, *Chem. Phys*. **223**, 279 (1997).

[17] J. P. Perchard, Z. Mielke, *Chem. Phys.* **264**, 221 (2001).

[18] U. Buck, *J. Phys. Chem*. **92**, 1023 (1988).

[19] U. Buck, X. J. Gu, M. Hobein, C. Lauenstein and A. Rudolph, *J. Phys. Chem*. **92**, 5561 (1988).

[20] U. Buck, X. J. Gu, M. Hobein, C. Lauenstein and A. Rudolph, *J. Chem. Soc. Faraday Trans*. **86**, 1923 (1990).

[21] F. Huisken, A. Kulcke, C. Laush, and J. M. Lisy, *J. Phys. Chem*. **95**, 3924 (1991).

[22] F. Huisken, M. Kaloudis, M. Koch, and O. Werhahn, *J. Chem. Phys*. **105**, 8965 (1996).

[23] C. Steinbach, M. Fárník, I. Ettischer, J. Siebers and U. Buck, *Phys. Chem. Chem. Phys*. **8**, 2752 (2006).

[24] M. Behrens, R. Fröchtenicht, M. Hartmann, J. G. Siebers, U. Buck, and F. C. Hagemeister, *J. Chem. Phys*. **111**, 2436 (1999).

[25] U. Buck, I. Ettischer, *J. Chem. Phys*. **108**, 33 (1998).

[26] R. N. Pribble, F. C. Hagemeister, and T. S. Zwier, *J. Chem. Phys*. **106**, 2145 (1997).

[27] C. J. Gruenloh, G. M. Florio, J. R. Carney, F. C. Hagemeister, and T. S. Zwier, *J. Phys. Chem. A* **103**, 496 (1999).

[28] T. Ebata, A. Fujii and N. Mikami, *Int. Rev. Phys. Chem.* **17**, 331 (1998).

[29] B. Brutschy, *Chem. Rev.* **100**, 3891 (2000).

[30] C. E. H. Dessent and K. Müller-Dethlefs, *Chem. Rev.* **100**, 3999 (2000).

[31] P. Escherick and A. Owyoung, *Chem. Phys. Lett.* **103**, 235 (1983).

[32] B. F. Henson, G. V. Hartland, V. A. Venturo and P. M. Felker, *J. Chem. Phys.* **91**, 2751 (1989).

[33] T. Ebata, T. Watanabe and N. Mikami, *J. Phys.Chem.* **99**, 5761 (1995).

[34] Y. Matsuda, T. Ebata and N. Mikami, *J. Chem. Phys.* **110**, 8397 (1999).

[35] S. T. Ceyer, P. W. Tiedemann, B. H. Mahan and Y. T. Lee, *J. Chem. Phys.* **70**, 14 (1979).

[36] Y. Matsuda, D. N. Shin and E. R. Bernstein, *J. Chem. Phys.* **120**, 4142 (2004).

[37] L. Belau, K. R. Wilson, S. R. Leone and M. Ahmed, *J. Phys. Chem. A* **111**, 10075 (2007).

[38] Y. Matsuda, N. Mikami and A. Fujii, *Phys. Chem. Chem. Phys*. **11**, 1279 (2009).

[39] H. K. Woo, P. Wang, K.-C. Lau, X. Xing, C. Chang and C. Y. Ng, *J. Chem. Phys.* **119**, 9333 (2003).

[40] M.-K. Bahng, X. Xing, S. J. Baek and C. Y. Ng, *J. Chem. Phys.* **123**, 084311 (2005).

[41] M.-K. Bahng, X. Xing, S. J. Baek, X. Qian and C. Y. Ng, *J. Phys. Chem. A* **110**, 8488 (2006).

[42] X.-M. Qian, A. H. Kung, T. Zhang, K. C. Lau and C. Y. Ng, *Phys. Rev. Lett.* **91**, 233001 (2003).

[43] H. K. Woo, P. Wang, K.-C Lau, X. Xing and C. Y. Ng, *J. Chem. Phys*. **120**, 1756 (2004).

[44] Y. Matsuda, M. Mori, M. Hachiya, A. Fujii and N. Mikami, *Chem. Phys. Lett.* **422**, 378 (2006).

[45] D. Sakai, Y. Matsuda, M. Hachiya, M. Mori, A. Fujii, and N. Mikami, *J. Phys. Chem. A* **112**, 6840 (2008).

[46] H. B. Fu, Y. J. Hu, and E. R. Bernstein, *J. Chem. Phys*. **124**, 024302 (2006).

[47] Y. J. Hu, H. B. Fu, and E. R. Bernstein, *J. Chem. Phys.* **125**, 154305 (2006).

[48] Y. J. Hu, H. B. Fu, and E. R. Bernstein, *J. Chem. Phys.* **125**, 154306 (2006).

[49] Y. J. Hu, H. B. Fu, and E. R. Bernstein, *J. Chem. Phys.* **125**, 154308 (2006).

[50] M. W. Williams and E. T. Arakawa, *Appl. Opt.* **18**, 1477 (1979).

[51] A. Duncanson and R. W. Stevenson, *Proc. Phys. Soc.* London **72**, 1001 (1958).

[52] A. D. Becke *J. Chem. Phys.* **98**, 5648 (1993).

[53] C. Lee, W. Yang, and R. G. Parr, *Phys. Rev. B* **37**, 785 (1988).

[54] I. Mills, in *Molecular Spectroscopy: Modern Research*, Eds.: K.N. Rao and C.W. Mathews (Academic Press, New York, 1972), p. 115.

[55] V. Barone, *J. Chem. Phys.* **122**, 014108 (2005).

[56] V. Barone, *J. Chem. Phys.* **120**, 3059 (2004).

[57] Frisch, M. J.; Trucks, G. W.; Schlegel, H. B. et al. Gaussian 09, Revision A.1, Gaussian Inc.: Pittsburgh, PA, 2003.

[58] J. Almlöf and P. R. Taylor, *J. Chem. Phys.* **86**, 4070 (1987).

[59] K. D. Cook, G. G. Jones, and J. W. Taylor, *Int. J. Mass Spectrom. Ion Phys*. **35**, 273 (1980).

[60] O. Kostko, L. Belau, K. R. Wilson, and M. Ahmed, *J. Phys. Chem.* A, **112**, 9555 (2008).

[61] M. Hachiya, Y. Matsuda, K.-I. Suhara, N. Mikami, and A. Fujii, *J. Chem. Phys*. **129**, 094306, (2008).

[62] F. Huisken and M. Stemmler, *J. Chem. Phys*. **98**, 7680 (1993).

[63] G. Vaidyanathan, M. T. Coolbaugh, W. R. Peifer, and J. F. Garvey, *J. Chem. Phys*. **94**, 1850 (1991).

[64] Y. J. Shi, S. Consta, A. K. Das, B. Mallik, D. Lacey, and R. H. Lipson, *J. Chem. Phys*. **116**, 6990 (2002).

[65] L.-H. Xu, X. Wang, T. J. Cronin, D. S. Perry, G. T. Fraser, A. S. Pine, *J. Mol. Spectrosc*. **185**, 158 (1997).

[66] X. Wang, D. S. Perry, *J. Chem. Phys.* **109**, 10795 (1998).

[67] S. Martrenchard, G. Grégoire, C. Dedonder-Lardeux, C. Jouvet and D. Solgadi, Phys. Chem. Com. **4**, 15 (1999).

[68] S.-T. Tsai, J.-C. Jiang, Y. T. Lee, A. H. Kung, S. H. Lin, and C.-K. Ni, *J. Chem. Phys*. **111**, 3434 (1999).

[69] U. Buck and J.-G. Siebers, and R. J. Wheatley, *J. Chem. Phys.* **108**, 20 (1998).

[70] F. C. Hagemeister, C. J. Gruenloh, and T. S. Zwier *J. Phys. Chem. A* **102**, 82 (1998).

[71] F. Dong, S. Heinbuch and J. J. Rocca, E. R. Bernstein, *J. Chem. Phys*. **124**, 224319 (2006).

[72] O. Mó and M. Yáñez, J. Elguero, *J. Chem. Phys.* **107**, 3592 (1997).

[73] M. V. Vener and J. Sauer, *J. Chem. Phys*. **114**, 2623 (2001).

[74] M. Masella, J. P. Flament, *J. Chem. Phys.* **108**, 7141 (1998).

[75] A. Bleiber, J. Sauer, *Chem. Phys. Lett*. **238**, 243 (1995).

[76] G. S. Tschumper, J. M. Gonzales, and H. F. Schaefer Ⅲ, *J. Chem. Phys.* **111**, 3027 (1999).

[77] M. M. Pires and V. F. DeTuri, *J. Chem. Theory Comput*. **3**, 1073 (2007).

[78] M. Masella, J. P. Flament, *Mol. Phys*. **95**, 97 (1998).

[79] M. Mandado, A. M. Graña, R. A. Mosquera, *Chem. Phys. Lett*. **381**, 22 (2003).

[80] A. Karpfen, *Adv. Chem. Phys*. **123**, 469 (2002).

[81] M. Rozenberg, A. Loewenschuss, and Y. Marcus, Phys. Chem. Chem. Phys. **2**, 2699 (2000).

# Chapter Four

# Infrared spectrum of mass-selected $CH_3S$ radical investigated with infrared + vacuum ultraviolet photoionization

## 4.1 Introduction

Oxidation of naturally occurring organic sulfur compounds such as dimethyl sulfide ($CH_3SCH_3$), dimethyl disulfide ($CH_3SSCH_3$), and methanethiol ($CH_3SH$) plays an important role in acid precipitation and climate modification[1–3]. As the methylthio (or thiomethoxy, $CH_3S$) radical is one of the key reactive intermediates in reactions relevant to modeling the atmospheric sulfur cycle,[4–8] unambiguous analysis of its spectra is important for monitoring the radical both in laboratories and in the atmosphere so as to understand its chemistry.

The ground electronic state $X\ ^2E$ of $CH_3S$ is subject to a Jahn-Teller distortion and spin-orbit coupling, which significantly influence the spectral and structural properties of $CH_3S$.[9–12] The energy of state $X\ ^2E_{1/2}$ is reported to be 256–264 $cm^{-1}$ greater than that of state $X\ ^2E_{3/2}$.[10–17] Several quantum-chemical calculations have predicted energies, geometries, and vibrational wave numbers of the $X\ ^2E$ and/or $A\ ^2A_1$ states of $CH_3S$.[18–25] Spectral investigations on gaseous $CH_3S$, including laser-induced fluorescence (LIF),[13錯誤! 尚未定義書籤。–15, 26, 27] electronic absorption [28–30] and emission,[31] microwave spectra,[32] photofragment yield,[33] four-wave mixing,[34, 35] fluorescence depletion,[36] and electron photodetachment of the $CH_3S^-$,[16, 17, 37, 38]

are extensive.

The first electronically excited state $A\ ^2A_1$ of $CH_3S$ correlates with $CH_3$ ($X\ ^2A_2''$) + S ($^1D$), but is crossed by three repulsive surfaces ($^4A_2$, $^4E$, and $^2A_2$) that correlate with the $CH_3$ ($X\ ^2A_2''$) + S ($^3P$) asymptote. These curve crossings induce various channels of predissociation in $CH_3S$ ($A\ ^2A_1$). A significant decrease in radiative lifetime was observed for vibrational levels of the $A$ state ~800 $cm^{-1}$ above the $A \leftarrow X$ origin.[15, 26, 39] Pushkarsky *et al.*[36] applied the fluorescence depletion technique to extend measurements of excited levels ~1490 $cm^{-1}$ above the $A \leftarrow X$ origin and reported that the predissociation of $CH_3S$ ($A\ ^2A_1$) was mode-selective, with C–S stretch ($\nu_3$) a promoting mode. Bise *et al.* recorded photofragment yield spectra of $CH_3S$ that was produced on laser photodetachment of a mass-selected beam of $CH_3S^-$;[33] they extended observation of vibronic bands of the $A \leftarrow X$ system to ~5240 $cm^{-1}$ above the origin and associated all features with vibrational progressions involving $\nu_2$ and $\nu_3$. Experiments using degenerate four-wave mixing[34] and two-color resonant four-wave mixing[35] further characterized states involving the $CH_3$ symmetric stretching ($\nu_1$) mode and confirmed the pronounced $\nu_3$ mode specificity for predissociation based on measurements of individual line widths. Experiments using photofragment translational spectroscopy showed that the H + $H_2CS$ product channel takes place for two vibronic levels of $CH_3S$ ($A\ ^2A_1$), $2^13^1$ and $2^13^2$; the dissociation mechanism is consistent with internal conversion of $CH_3S$ ($A\ ^2A_1$) to $CH_3S$ ($X\ ^2E$) followed by unimolecular dissociation.[40].

With $C_{3v}$ symmetry, the ground electronic state $CH_3S$ ($X\ ^2E$) has three vibrational modes ($\nu_1$–$\nu_3$) of $a_1$ symmetry and three degenerate vibrational modes ($\nu_4$–$\nu_6$) of e symmetry that is Jahn-Teller active. The normal modes of $CH_3S$, calculated with Hartree-Fock method, are depicted in Figure 4-1. The $a_1$ modes are described approximately as the $CH_3$ symmetric stretching ($\nu_1$), the $CH_3$ umbrella motion ($\nu_2$), and the C–S stretching ($\nu_3$) modes. The degenerate modes are the $CH_3$ asymmetric stretching ($\nu_4$), the $CH_3$ deformation ($\nu_5$), and the

HCS deformation ($\nu_6$) modes. While the true normal modes of each state of the molecule are linear combinations of these internal coordinate motions, the description with the internal coordinate is still useful to visualize the motion of the vibrational modes of the molecule. The Jahn-Teller interaction is expected to lift the degeneracy of modes $\nu_4$–$\nu_6$ of $X\ ^2$E, with splitting largest for $\nu_6$.

Some vibrational wavenumbers of state $X\ ^2$E were derived from dispersed fluorescence [13–15] and photoelectron spectra.[16, 17] Among those observations, only $\nu_2$ = 1313–1316 cm$^{-1}$ and $\nu_3$ = 727 ± 3 cm$^{-1}$ (ref.13, 15) were accurately determined; other vibrational assignments were tentative and showed large deviations in wavenumbers. For example, values of $\nu_1$ = 2774 cm$^{-1}$ and $\nu_4$ = 2706 cm$^{-1}$ derived previously from dispersed fluorescence[15] are much smaller than corresponding values of $CH_3O$ and those predicted for $CH_3S$ with quantum-chemical calculations.[11, 12, 24, 25] Schwartz *et al.* recorded a photoelectron spectrum of $CH_3S^-$ at 364 nm and reported that $\nu_3$ = 725 ± 15 cm$^{-1}$ and $\nu_1$ = 2960 ± 30 cm$^{-1}$.[17] Bahou and Lee[41] reported the infrared (IR) spectrum of $CH_3S$, produced on ultraviolet photolysis of three precursors isolated in solid *p*-$H_2$, and assigned features at 724.2 ($\nu_3$), 2898.4 ($\nu_4$), 1440.0 ($\nu_5$), 1056 and 771.1 cm$^{-1}$ ($\nu_6$), consistent with those predicted with a spin-vibronic Hamiltonian accounting for the anharmonic effects and the Jahn-Teller effects to the quartic term by Marenich and Boggs.[12] No IR spectrum of gaseous $CH_3S$ has been reported.

Because the radical of interest is generated typically from photolysis of a precursor which has a structure similar to the radical, its IR spectrum is often overlapped with the IR spectrum of the precursor or by-products. A spectral technique with mass selection is hence highly desirable for IR spectrum of free radicals free from interference of precursors. Vacuum ultraviolet (VUV) ionization with its photon energy slightly above the ionization threshold of the species of interest typically induces soft ionization without fragmentation. A combination of vibrational excitation and VUV photoionization with mass detection has been exploited to investigate the

vibrational spectra of size-selected neutral molecules and clusters, as discussed in a recent review.[42] Dissociation of a specific cluster with IR laser light decreases the concentration of this cluster which consequently depletes the corresponding ion signal upon ionization of the clusters with VUV light. The IR spectra of the cluster may be obtained by tuning the IR laser wavelength while monitoring the intensities of ion signals. Likely the dissociation also increases the concentration of smaller clusters, hence careful processing of the action spectra is necessary to derive reliable IR spectra of each cluster, as demonstrated for methanol clusters.[43] This ion-depletion method is unsuitable for IR spectra of free radicals because typically the free radicals do not dissociate upon irradiation of IR light.

Using a similar experimental setup, Ng and coworkers employed (1 + 1) IR-VUV photoionization (IR-VUV-PI) to investigate the vibrational spectrum of neutral molecules and cations.[44–50] The VUV photon energy was set to be slightly less than the ionization threshold of the species of interest and the enhancement in intensity of the ion signal upon additional IR irradiation was monitored while scanning the frequency of IR light. The method using IR-VUV-PI has been applied to stable molecules, but not to free radicals.

In the present work, we applied the IR-VUV-PI method to obtain the IR spectrum, in the range 2780–3270 $cm^{-1}$, of $CH_3S$ radical produced on photolysis of $CH_3SH$ at 248 nm. With the advantage of the mass selectivity, the IR spectrum of $CH_3S$ radical shows absorption bands with no interference from parent or byproducts. Our results provide direct evidence for the assignments of $\nu_1$ and $\nu_4$ modes of gaseous $CH_3S$.

## 4.2 Experiments

The apparatus used to perform single-photon VUV and IR-VUV photoionization spectroscopy are described in chapter two. Briefly, a pulsed supersonic jet was introduced

into the photoionization region of a time-of-flight (TOF) mass spectrometer. The ionization was achieved either with a single VUV photon or a combination of IR and VUV photons.

In the photoionization efficiency (PIE) measurements, the ion signals were monitored as the frequency of the VUV photon was tuned. In the IR-VUV-PI experiments, the ion signals were monitored as the frequency of the IR laser was tuned while keeping the frequency of the VUV light fixed at a value slightly smaller than the ionization threshold of the species of interest. In the present experiments, the wavenumber of the IR laser was tuned through the range 2650–3750 $cm^{-1}$ while the wavelength of the VUV laser was maintained at 134.84 nm (9.1952 eV, 74,165 $cm^{-1}$), ~223 $cm^{-1}$ below the ionization threshold of $CH_3S$ ($X\ ^2E_{1/2}$). The VUV laser pulse was delayed 30–100 ns with respect to the IR laser pulse. The energy of the IR light was measured concurrently as its wavenumber was tuned; the observed raw spectra were normalized with the intensity of the IR laser.

The tunable VUV laser light was generated through resonant four-wave mixing ($\omega_{VUV} = 2\omega_1 - \omega_2$) in a Kr gas cell using UV light at frequency $\omega_1$ corresponding to 47,046.43 $cm^{-1}$ (212.556 nm) to achieve the two-photon transition of Kr $4p^6(^1S_0) \rightarrow 4p^5(^2P^0_{3/2})5p(^2[1/2]_0)$ at 94,092.86 $cm^{-1}$ [51] and tunable visible light at frequency $\omega_2$ corresponding to the range 20,408–17,241 $cm^{-1}$ (490–580 nm). Both UV and visible beams were focused into the gas cell containing a mixture of Kr and Ar (1:3 at 50 Torr) with a $MgF_2$ lens ($f$ = 20 cm). The resulting VUV light in the range 73,685–76,852 $cm^{-1}$ (9.136–9.528 eV) was separated from the UV and visible beams through a convex $MgF_2$ lens ($f$ = 15 cm) before being introduced into the center of the ionization region. The UV light was generated from the second-harmonic output of a dye laser (Scanmate, Lambda Physik, bandwidth 0.7 $cm^{-1}$) and the visible light was produced from a second dye laser (Scanmate 2E, Lambda Physik, bandwidth 0.19 $cm^{-1}$). Both dye lasers were pumped by the 355-nm output of a Nd:YAG laser (Spectra Physics, PRO-270, 230 mJ $pulse^{-1}$, 10 Hz).

The tunable IR laser emission was generated with an optical parametric oscillator/amplifier (OPO/OPA) system (LaserVision, 8 mJ pulse$^{-1}$, resolution 1.6 cm$^{1}$, with a grating cavity) that was pumped with an Nd:YAG laser (Continuum, Powerlite 8000, 1064 nm, 440 mJ pulse$^{-1}$, 10 Hz, unseeded). The IR beam was focused onto the ionization region in a direction counter-propagating with the VUV beam.

A pulsed jet of 1 % $CH_3SH$ seeded in Ne was produced on supersonic expansion through a pulsed valve (Even-Lavie valve, 10 Hz) with a total stagnation pressure of 3.5 atm. The output of the KrF excimer laser at 248 nm was mildly focused to intersect the $CH_3SH$ jet ~2 mm from the nozzle tip to generate $CH_3S$ radicals. The gaseous jet was skimmed with a conical skimmer before being introduced into the photoionization region of the TOF mass spectrometer. The ionization region is located ~15 cm from the nozzle tip.

$CH_3S$ radicals were ionized in the ionization region to form $CH_3S^+$, which were extracted perpendicularly with a potential of 200 V and accelerated into a field-free tube of length 1 m. The accelerator and repeller plates of the ion optics were biased at 1500 V and 1700 V, respectively. Ions were subsequently detected with a microchannel plate (MCP, Burle Electro-Optics, 18 mm). After passing a preamplifier (EG&G ORTEC, Model 9306, bandwidth 1 GHz), the signal was recorded with a 14-bit digitizer (GaGe Instruments, Model CS8327, 100 MS/s) and also displayed on a digital oscilloscope.

The frequency of the dye laser was calibrated simultaneously with a wavemeter (WA 5500, Burleigh, 190–680 nm) and with a FeNe optogalvanic cell (Hamamatsu Photonics); the accuracy of wavenumber measurements is ~0.2 cm$^{-1}$. Concurrently with experiments, the frequency of the IR light was calibrated with the spectra of suitable reference gases ($CH_4$, $C_2H_2$) recorded with a photoacoustic cell; the accuracy of wavenumber measurements is ~1.6 cm$^{-1}$, mainly limited by the spectral width of the IR laser.

$CH_3SH$ (99.5 %) and Ne (99.995 %, Scientific Gas Products) were used without further

purification.

## 4.3 Results and Discussion

### 4.3.1 Photoionization Efficiency (PIE) Spectra of $CH_3S$

Fission of the S–H bond is the dominant primary process following direct excitation of $CH_3SH$ to state $1^1A''$ with light at 248 nm (40,322 $cm^{-1}$). The energy to dissociate the S–H bond, obtained on analysis of translational energy of photofragments, is $D_0°(CH_3S–H)$ = 30,250 ± 100 $cm^{-1}$.[52] The absorption cross section of $CH_3SH$ at 248 nm is $3.5\times10^{-19}$ $cm^2$ $molecule^{-1}$ at 296 K.[53] At 248 nm, most $CH_3S$ fragments are formed in their ground vibrational state, with a small fraction in state $v_3$ = 1; the concentration ratio of $CH_3S$ ($X\ ^2E_{3/2}$) to $CH_3S$ ($X\ ^2E_{1/2}$) was estimated to be ~2:1.[52]

$CH_3S$ radicals were softly ionized without fragmentation upon irradiation with VUV light near 133 nm. The PIE spectra after normalization with the incident VUV photon intensity are shown in Figure 4-1. A series of steps appear in Figure 4-1(a) that shows a PIE spectrum in region 9.14–9.38 eV (73,719–75,655 $cm^{-1}$) recorded with a scan step of 4 $cm^{-1}$. The small step at 9.165 eV (73,920 $cm^{-1}$) is ascribed to ionization from the vibrationally excited ($v_3$ = 1) level of $CH_3S$ ($X\ ^2E_{3/2}$).[54, 60] The following two step-like features are assigned to ionization transitions $CH_3S$ ($X\ ^2E_{1/2}$) → $CH_3S^+$ ($X\ ^3A_2$) and $CH_3S$ ($X\ ^2E_{3/2}$) → $CH_3S^+$ ($X\ ^3A_2$). Figure 4-1(b) and (c) are high-resolution PI spectra recorded with a scan step of 1 $cm^{-1}$ in regions 9.2440–9.2635 eV (74,558–74,715 $cm^{-1}$) and 9.218–9.234 eV (74,348–74,477 $cm^{-1}$), respectively. The ionization thresholds from states $^2E_{1/2}$ and $^2E_{3/2}$ of $CH_3S$ are determined as 9.2230 ± 0.0004 eV (74388 ± 3 $cm^{-1}$) and 9.2546 ± 0.0004 eV (74643 ± 3

$cm^{-1}$), respectively, from the intersections of two fitted lines. To determine the adiabatic ionization energies (*IE*) from states $^2E_{1/2}$ and $^2E_{3/2}$, we fitted the first-order derivatives of the spectra with Gaussian functions, as shown in the insets in Figure 4-1(b) and (c), to yield line centers at 9.2255 ± 0.0004 eV (74,408 ± 3 $cm^{-1}$) and 9.2570 ± 0.0004 eV (74663 ± 3 $cm^{-1}$), respectively; these energies are indicated with arrows in the figures. The errors in fitting and wavelength calibration are estimated to be 2 and 1 $cm^{-1}$, respectively. In a separate experiment we employed the same method to evaluate the *IE* of $CH_3SH$, the PIE spectrum and the first-order derivative spectra fitted with Gaussian function are shown in Figure 4-3. We derived an adiabatic *IE* of 9.4464 ± 0.0005 eV (76,190 ± 4 $cm^{-1}$) for $CH_3SH$ in agreement with the literature value of 9.446 ± 0.010 eV (76,187± 81 $cm^{-1}$).[55] Figure 4-2(a) shows a PI spectrum recorded with a scan step of 4 $cm^{-1}$ in the region 9.300–9.460 eV (75,010–76,300 $cm^{-1}$). Two series of step-like features are assigned to ionization transitions $CH_3S$ ($X\ ^2E_{1/2}$) → $CH_3S^+$ ($X\ ^3A_2$, $v_3$ = 1, 2) and $CH_3S$ ($X\ ^2E_{3/2}$) → $CH_3S^+$ ($X\ ^3A_2$, $v_3$ = 1, 2). The thresholds of the steps for $CH_3S$ ($X\ ^2E_{1/2}$, $^2E_{3/2}$,) → $CH_3S^+$ ($X\ ^3A_2$, $v_3$ = 1) are 9.314 ± 0.0005 eV (75,122 ± 4 $cm^{-1}$) and 9.345 ± 0.0005 eV (75,373 ± 4 $cm^{-1}$), respectively. The fitted maxima of the first derivatives of the spectra lie at 9.3168 ± 0.005 eV (75,145 ± 4 $cm^{-1}$) and 9.3479 ± 0.0005 eV (75,396 ± 4 $cm^{-1}$), respectively.

The adiabatic ionization energy of $CH_3S$ was predicted to be 9.25 eV with the G2 method.[22] Several authors reported the ionization energy (*IE*) of $CH_3S$.[56–60] Experimental values reported in recent years agree among themselves, [58–60] but small discrepancies exist. The adiabatic *IE* of 9.2570 ± 0.0004 eV (74,663 ± 3 $cm^{-1}$) for $CH_3S$($X\ ^2E_{3/2}$) determined in this work agrees with the value 9.262 ± 0.005 eV (74,705 ± 40 $cm^{-1}$) determined according to the half-rise point of the step by Ruscic and Berkowitz[58] who employed VUV photoionization and mass detection on $CH_3S$ radicals prepared from reactions of F atoms with $CH_3SH$ in a gas

cell. The *IE* of 9.2649 ± 0.001 eV (74,726 ± 8 $cm^{-1}$) for $CH_3S$ ($X\ ^2E_{3/2}$) obtained on comparison of simulated spectra with observed photoelectron spectra by Hsu and Ng[60] in the two-photon pulsed field ionization experiments is 63 $cm^{-1}$ greater than our value, beyond listed errors. The discrepancy might be partly because the energy reported by Hsu and Ng corresponds to the lowest possible transition. However, two most intense peaks reported by them lie at 74,710 and 74,734 $cm^{-1}$, only separated by –16 and 8 $cm^{-1}$ from the reported *IE*. Likely some discrepancy is due to calibration errors.

The spin-orbit splitting of $CH_3S$ ($X\ ^2E$) determined according to the energy difference between the *IE* of states $^2E_{3/2}$ and $^2E_{1/2}$ is 255 ± 3 $cm^{-1}$, which agrees with previous experimental values of 255.5[14] and 259.1[15] from fluorescence experiments and 257 ± 5 $cm^{-1}$ from threshold photoelectron experiments[60]. The C–S stretching ($\nu_3$) wavenumber of $CH_3S$ ($X\ ^2E_{3/2}$) determined from the interval between ionization transitions $CH_3S$ ($X\ ^2E_{3/2}$, $v = 0$) → $CH_3S^+$ ($X\ ^3A_2$) and $CH_3S$ ($X\ ^2E_{3/2}$, $\nu_3 = 1$) → $CH_3S^+$ ($X\ ^3A_2$) is 723 ± 4 $cm^{-1}$, which agrees with 727 ± 5 $cm^{-1}$ observed in dispersed fluorescence[15] and 724.4 $cm^{-1}$ observed in the IR spectrum of $CH_3S$ in a *p*-$H_2$ matrix.[41] The wavenumber for the C–S stretching ($\nu_3$) mode of $CH_3S^+$ determined from the interval between ionization transitions $CH_3S$ ($X\ ^2E_{3/2}$) → $CH_3S^+$ ($X\ ^3A_2$, $v = 0$) and $CH_3S$ ($X\ ^2E_{3/2}$) → $CH_3S^+$ ($X\ ^3A_2$, $\nu_3 = 1$) is 733 ± 3 $cm^{-1}$, which agrees with 700 ± 60 $cm^{-1}$ determined in the VUV photoionization experiments[58] and 733 ± 5 $cm^{-1}$ determined from the threshold photoelectron experiments.[59]

### 4.3.2 Time-of-flight mass spectrum

Figure 4-4(a) shows the time-of-flight (TOF) spectrum recorded on VUV ionization of the $CH_3SH$ supersonic jet at 134.84 nm (9.195 eV or 74,165$cm^{-1}$). At this wavelength,

$CH_3SH$ cannot be ionized because the *IE* of $CH_3SH$, 9.4464 ± 0.0005 eV (76190 ± 4 $cm^{-1}$), is much greater than the VUV photon energy. The intense line at *m*/*z* = 96 is due to $(CH_3SH)_2^+$; weaker features (not shown) at *m*/*z* 144, 192, and 240 are due to $(CH_3SH)_n^+$ (*n* = 3–5). A small signal with *m*/*z* = 94 (denoted $DMDS^+$) is due to $CH_3SSCH_3^+$ impurity. The small $CH_3SH^+$ signal might result from the fragmentation of $(CH_3SH)_n^+$ ($2 \le n \le 5$) in the acceleration region. Figure 4-4(b) was recorded on irradiation of $CH_3SH$ with IR light at 2905 $cm^{-1}$ and VUV light at 134.84 nm. Because the wavenumber of the IR light did not match any vibrational transition of $CH_3SH$ in the supersonic jet, even if the combined energy exceeds the *IE* of $CH_3SH$, the TOF spectrum remains unaltered from that of Figure 4-4(b). Figure 4-4(c) shows the TOF spectrum recorded on ionization at 9.18 eV of $CH_3SH$ in the supersonic jet that was irradiated at 248 nm before ionization. A small $CH_3S^+$ signal at *m*/*z* = 47 appeared, presumably due to ionization of $CH_3S$ ($X\ ^2E_{3/2}$) from vibrationally excited states. Figure 4-4(d) shows the TOF spectrum of the 248-nm irradiated jet of $CH_3SH$ induced by both IR (2905 $cm^{-1}$) and VUV (74,165 $cm^{-1}$) radiation. The $CH_3S^+$ was enhanced significantly because of resonant IR absorption of $CH_3S$ with total energy ~9.556 eV of the IR + VUV photons exceeding the *IE* of $CH_3S$.

### 4.3.3 IR-VUV spectrum of $CH_3S$

Figure 4-5(a) shows the IR-VUV photoionization spectrum of $CH_3S$ obtained on monitoring the increase in intensity of the $CH_3S^+$ signal while scanning the wavenumber of the IR light in regions 2790–3000 and 3200–3270 $cm^{-1}$; the spectrum was obtained on averaging 7 spectra recorded under similar experimental conditions. The enhanced signal of $CH_3S^+$ was due to (1+1) IR-VUV ionization of $CH_3S$ when the wavenumber of the IR light matched that of a vibrational transition of $CH_3S$ ($X\ ^2E$). The IR spectrum in Figure 4-5(a)

exhibits one intense band near 2904 $cm^{-1}$ and three weaker features near 2819, 2978, and 3241 $cm^{-1}$. Table 4-1 compares the wavenumbers of IR bands observed in this work with those observed for $CH_3S$ in a *p*-$H_2$ matrix [41] and the wavenumbers of vibrational transitions of $CH_3S$ ($X\ ^2E_{3/2}$ and $^2E_{1/2}$) predicted by Marenich and Boggs.[12] Two features at 2898.4 and 3210.0 $cm^{-1}$ were reported for absorption of $CH_3S$ isolated in solid *p*-$H_2$ in this region;[41] they are consistent with observed bands in this work, with matrix shifts –6 and –31 $cm^{-1}$, respectively. A weak band near 2813.0 $cm^{-1}$ tentatively assigned to $CH_3S$ isolated in solid *p*-$H_2$ is also consistent with our observation of a band near 2819 $cm^{-1}$. The band near 2978 $cm^{-1}$ observed in this work is new because this region was severely interfered by intense absorption of precursors ($CH_3SH$, $CH_3SCH_3$, $CH_3SSCH_3$) and byproduct $H_2CS$ in the matrix. The mass selection in this work successfully eliminated this problem of interference.

Marenich and Boggs performed extensive computations on the vibrational energy levels of $CH_3S$ using a spin-vibronic Hamiltonian including up to quartic Jahn-Teller terms and accounting for all important anharmonic effects.[11,12] The features below 2300 $cm^{-1}$ that were observed in the *p*-$H_2$ matrix agree with wavenumbers of transitions of $CH_3S$ ($X\ ^2E_{3/2}$) predicted by Marenich and Boggs,[12] as compared in Table 4-1 of Ref. 41. For the C–H stretching modes, the predicted frequencies for transitions $1^1(e)$, $4^1(a_1)$, and $4^1(e)$ of $CH_3S$ ($X\ ^2E_{3/2}$) are 2938, 3022, and 3026 $cm^{-1}$ and $1^1(e^*)$, $4^1(a_2)$, and $4^1(e^*)$ of $CH_3S$ ($X\ ^2E_{1/2}$) are 2942, 3023, and 3030 $cm^{-1}$. In this notation $n^v$, $n$ indicates vibrational mode $\nu_n$ involved in the transition from the ground vibrational state and the superscript $v$ indicates the vibrational quantum number of the upper state; the symmetry of the spin-vibronic levels is indicated in parentheses. For the non-degenerate (symmetry $a_1$) vibrational modes of states $CH_3S$ ($X\ ^2E_{3/2}$) and $CH_3S$ ($X\ ^2E_{1/2}$), the spin-vibronic symmetry is indicated as e and e*, respectively.

The intense feature at 2898.4 $cm^{-1}$ observed in solid *p*-$H_2$ is clearly associated with the $\nu_4$ mode of $CH_3S$ if one considers the theoretical prediction that this mode carries the most

intensity in C–H stretching. Quantum-chemically predicted harmonic vibrational wavenumbers on the C–H stretching modes are typically greater than experimental values by 3–5 % because of the large anharmonicity involved. When we scaled the three bands $1^1$, $4^1$(a), and $4^1$(e) predicted by theory with a factor of 2898.4/3022 = 0.959, we derived line positions at 2818, 2898, and 2902 $cm^{-1}$ for $CH_3S$ ($X\ ^2E_{3/2}$) and 2821, 2899, and 2906 $cm^{-1}$ for $CH_3S$ ($X\ ^2E_{1/2}$). These lines are indicated as sticks in Figure 4-5 (b), in which the statures of sticks are proportional to the predicted IR intensities and lines of $CH_3S$ ($X\ ^2E_{1/2}$) are half as intense as the corresponding lines of $CH_3S$ ($X\ ^2E_{3/2}$) to reflect the reported relative populations upon photolysis of $CH_3SH$ at 248 nm. [52, 60] We are unable to distinguish these small differences (1–4 $cm^{-1}$) in vibrational wavenumbers between states $^2E_{3/2}$ and $^2E_{1/2}$; these differences might increase slightly the width of each observed band. The wavenumber for the $\nu_1$ mode after scaling, 2818–2821 $cm^{-1}$, is nearly identical to the peak position of the observed band at 2819 $cm^{-1}$. This agreement supports the assignment of the band near 2819 $cm^{-1}$ to the $\nu_1$ mode of $CH_3S$.

The bands near 2978 and 3241 $cm^{-1}$ are consistent with bands near 2960 ± 30 and 3225 ± 30 $cm^{-1}$ reported by Schwartz *et al*. from their photoelectron spectra of $CH_3S^-$; these bands were assigned to transitions to the $\nu_1 = 1$ levels of $CH_3S$ ($X\ ^2E_{3/2}$ and $^2E_{1/2}$).[17] These bands are beyond the range (2402 $cm^{-1}$) predicted by Marenich and Boggs[12] for the overtone and combination transitions of $CH_3S$. We tentatively assigned these two features near 2978 and 3241 $cm^{-1}$ as transitions $3^1 5^1 6^1$(e) and $3^1 5^1 6^1$(a). For simplicity, we only discuss the transitions of $CH_3S$ ($X\ ^2E_{3/2}$) for these two features.

The wavenumber of the band near 2978 $cm^{-1}$ is 748–733 $cm^{-1}$ larger than the two $5^1 6^1$(e) transitions predicted at 2230 and 2245 $cm^{-1}$ by Marenich and Boggs, with these separations near the vibrational wavenumber 742 $cm^{-1}$ predicted for $\nu_3$ of $CH_3S$. Similarly, the

wavenumber of this band is 1438 $cm^{-1}$ larger than the $3^16^1(a_1)$ transition predicted at 1540 $cm^{-1}$; the separation is near vibrational wavenumbers 1436 and 1463 $cm^{-1}$ predicted for $5^1(a_1)$ and $5^1(e)$. An assignment of $3^15^16^1(e)$ for this band hence seems reasonable. Other possible assignments, such as $2^16^2$ or $5^16^2$, show less satisfactory agreement. The expected two closely spaced components of $3^15^16^1(e)$ based on those of $5^16^1(e)$ transitions predicted at 2230 and 2245 $cm^{-1}$ might also explain the larger width with multiple peaks observed for this feature near 2962 and 2978 $cm^{-1}$.

The wavenumber of the band near 3241 $cm^{-1}$ is 1065–1040 $cm^{-1}$ larger than the $3^15^1(a_1)$ and $3^15^1(e)$ transitions predicted at 2176 and 2201 $cm^{-1}$, with these separations near the vibrational wavenumber 1105 $cm^{-1}$ predicted for the $6^1(e)$ transition of $CH_3S$. Similarly, the wavenumber of this band is 1366 $cm^{-1}$ larger than the $3^16^1(e)$ transition predicted at 1844 $cm^{-1}$; the separation is near vibrational wavenumbers 1436 and 1463 $cm^{-1}$ predicted for $5^1(a_1)$ and $5^1(e)$. An assignment of this band to another component of $3^15^16^1$ (likely in symmetry a) hence seems reasonable, but an alternative assignment $2^13^16^1(e)$ cannot be positively excluded because $2^1$ is predicted to be 1358 $cm^{-1}$, only 78 $cm^{-1}$ smaller than $5^1(a_1)$.

Using the SPECVIEW program,[61] we compared the rotational contour observed for the $\nu_1$ band with those simulated with rotational parameters $A''$ = 5.67943 and $B''$ = 0.44958 derived from the fluorescence spectrum[14] and $A'/A''$ = 0.9901 and $B'/B''$ = 1.001 derived from the B3LYP/cc-pVTZ calculations. The spectrum simulated with $J_{max}$= 30, $T$ = 25 K, and a Gaussian line shape with full width 1.6 $cm^{-1}$ at half maximum agrees satisfactorily with experimental observation.

The enhancement of $CH_3S^+$ ion signals upon IR irradiation on the $\nu_1$ and $\nu_4$ modes of $CH_3S$ is smaller than one expects. This might be due to a smaller ionization yield for the vibrationally excited state of $CH_3S$. In our ionization scheme, vibrationally excited $CH_3S$ can

only be ionize into $CH_3S^+$ in its ground vibrational state because of the smaller energy of the VUV photons employed. One would expect that the Franck-Condon factors for transitions from states involving excited $\nu_1$ and $\nu_4$ modes of $CH_3S$ to $CH_3S^+$ in its ground vibrational state be smaller than that for transitions from the ground vibrational state of $CH_3S$ to the ground vibrational state of $CH_3S^+$ because the C–H bond lengths of $CH_3S$ and $CH_3S^+$ are similar. The major difference in structures of $CH_3S$ and $CH_3S^+$ is the C–S bond length; therefore one might expect significant enhancements in ion signal of $CH_3S^+$ from excitation of the $\nu_3$ mode of $CH_3S$. This might explain why the features near 2978 and 3241 $cm^{-1}$, assigned to transitions $3^1 5^1 6^1$(e) and $3^1 5^1 6^1$(a), were observed with intensities only slightly smaller than those of features near 2819 and 2904 $cm^{-1}$ assigned as transitions $1^1$ and $4^1$, respectively.

## 4.4 Conclusion

Analysis of the photoionization efficiency spectra of $CH_3S$ provides a refined value of the adiabatic ionization energies 9.2570 ± 0.0004 eV (74,663 ± 3 $cm^{-1}$) for $CH_3S$ ($X\ ^2E_{3/2}$) and 9.2255 ± 0.0004 eV (74,408 ± 3 $cm^{-1}$) for $CH_3S$ ($X\ ^2E_{1/2}$), with spin-orbit splitting of 255 ± 4 $cm^{-1}$ in agreement with previous reports.

In the IR-VUV-PI measurement, mass-selected absorption bands of $CH_3S$ near 2819 and 2904 $cm^{-1}$ were observed and assigned as transitions $1^1$ and $4^1$ from the ground vibrational state, respectively, based on comparison with transition wavenumbers predicted by Marenich and Boggs[12] with a spin-vibronic Hamiltonian accounting for the anharmonic effects and Jahn-Teller effects to the quartic term and those observed for $CH_3S$ in solid *p*-$H_2$.

[41] The additional features near 2978 and 3241 $cm^{-1}$ are consistent with bands near 2960 ± 30 and 3225 ± 30 $cm^{-1}$ observed in the photoelectron spectrum of $CH_3S^-$;[17] these bands were previously assigned to transitions to the $\nu_1$ states of $CH_3S$ ($X\ ^2E_{3/2}$) and $CH_3S$ ($X\ ^2E_{1/2}$), respectively. We tentatively assigned these features near 2978 and 3241 $cm^{-1}$ to transitions $3^1 5^1 6^1$(e) and $3^1 5^1 6^1$(a) from the ground vibrational state of $CH_3S$ based on vibrational wavenumbers predicted for the corresponding lower states of $CH_3S$ by Marenich and Boggs.[12]

Observed features are in agreement with lines at 2898.4 and 3210.0 $cm^{-1}$ observed for $CH_3S$ isolated in a *p*-$H_2$ matrix. Clear identification of additional bands near 2819 and 2978 $cm^{-1}$ demonstrates the advantage of the IR-UV-PI method with mass-selective detection to obtain IR spectrum of free radicals free from interference by their precursors or byproducts. Though technically demanding, the IR-UV-PI technique is expected to be developed into a powerful tool for spectral studies of free radicals in the infrared region.

Table 4-1 Vibrational wavenumbers (in $cm^{-1}$) of $CH_3S$ observed experimentally and predicted quantum-chemically.

| Transition | calculations | | *p*-$H_2$ | IR-VUV-PI |
|---|---|---|---|---|
| | $X\ ^2E_{3/2}$ | $X\ ^2E_{1/2}$ | matrix | |
| $1^1$ | 2938 | 2942 | 2813.0? | 2819 |
| $4^1(a_1)$ | 3022 | 3023 | 2898.4 | 2904[b] |
| $4^1$(e) | 3026 | 3030 | | 2904[b] |
| $3^1 5^1 6^1$(e) [a] | | | | 2962[c] |
| | | | | 2978[c] |
| $3^1 5^1 6^1$(a)[a] | | | 3210.0 | 3241 |
| Reference | 12 | | 41 | This work |

[a] Tentative assignments.

[b] Overlapped bands.

[c] Multiple components.

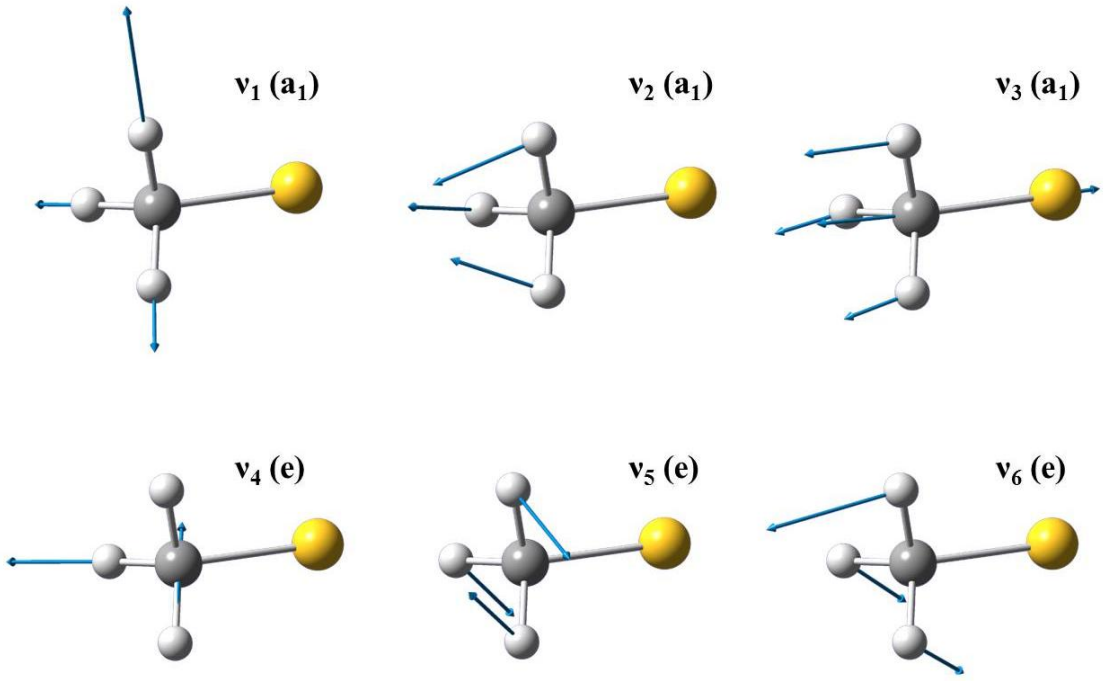


Figure 4-1 Normal modes of the $CH_3S$ radicals. The $a_1$ modes are described approximately as the $CH_3$ symmetric stretching ($\nu_1$), the $CH_3$ umbrella motion ($\nu_2$), and the C–S stretching ($\nu_3$) modes. The degenerate e modes are the $CH_3$ asymmetric stretching ($\nu_4$), the $CH_3$ deformation ($\nu_5$), and the HCS deformation ($\nu_6$) modes.

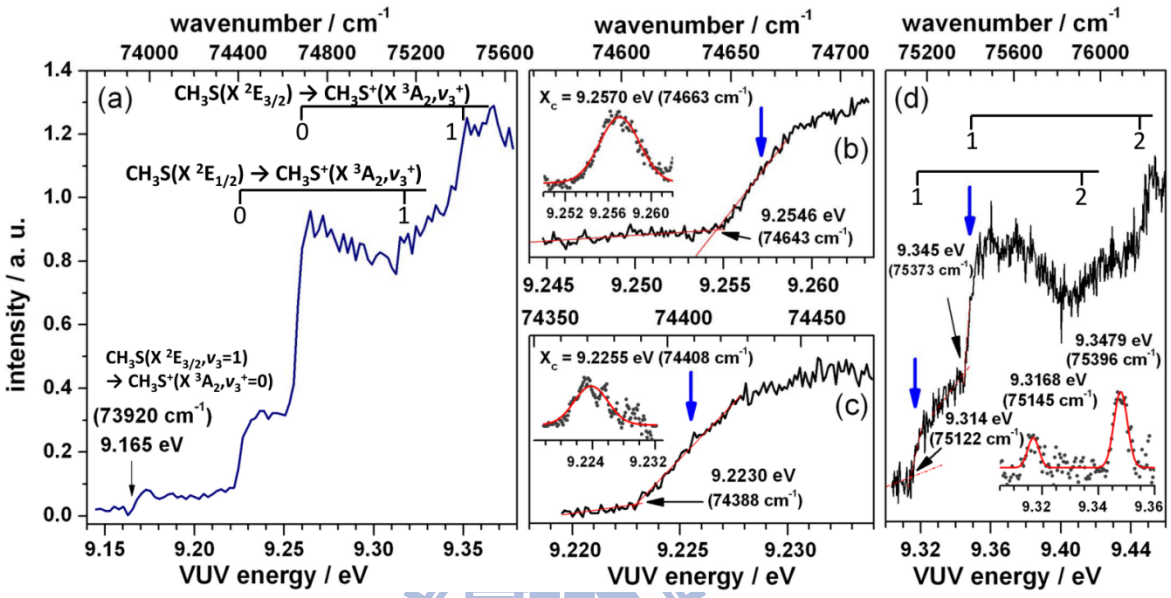


Figure 4-2 Photoionization efficiency spectra of $CH_3S$ (a) in region 9.14–9.38 eV (73,719–75,655 $cm^{-1}$) recorded with scan step 4 $cm^{-1}$, (b) in region 9.2440–9.2635 eV (74,558–74,715 $cm^{-1}$) with scan step 1 $cm^{-1}$, (c) in region 9.218–9.234 eV (74,348–74,477 $cm^{-1}$) with scan step 1 $cm^{-1}$, and (d) in region 9.30–9.46 eV (75,010–76,300 $cm^{-1}$) with scan step 4 $cm^{-1}$. The insets are first-order derivative spectra fitted with Gaussian functions. The energies of the maxima thus derived are indicated with thick blue arrows. The threshold energies are indicated with thin black arrows.

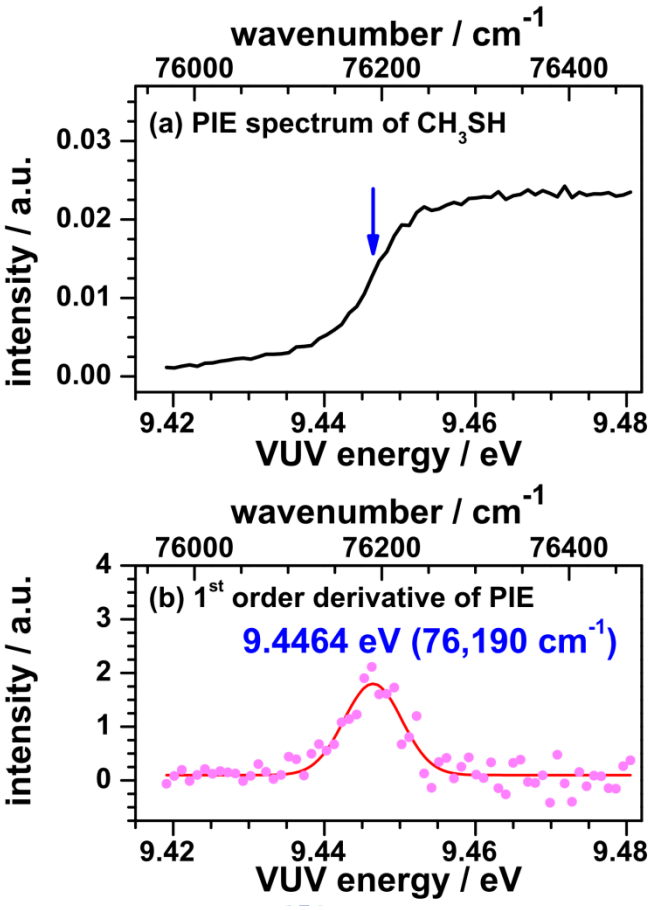


Figure 4-3 (a) Photoionization efficiency spectra of $CH_3SH$ in region 9.415–9.482 eV, and (b) its first-order derivative spectra fitted with Gaussian function.

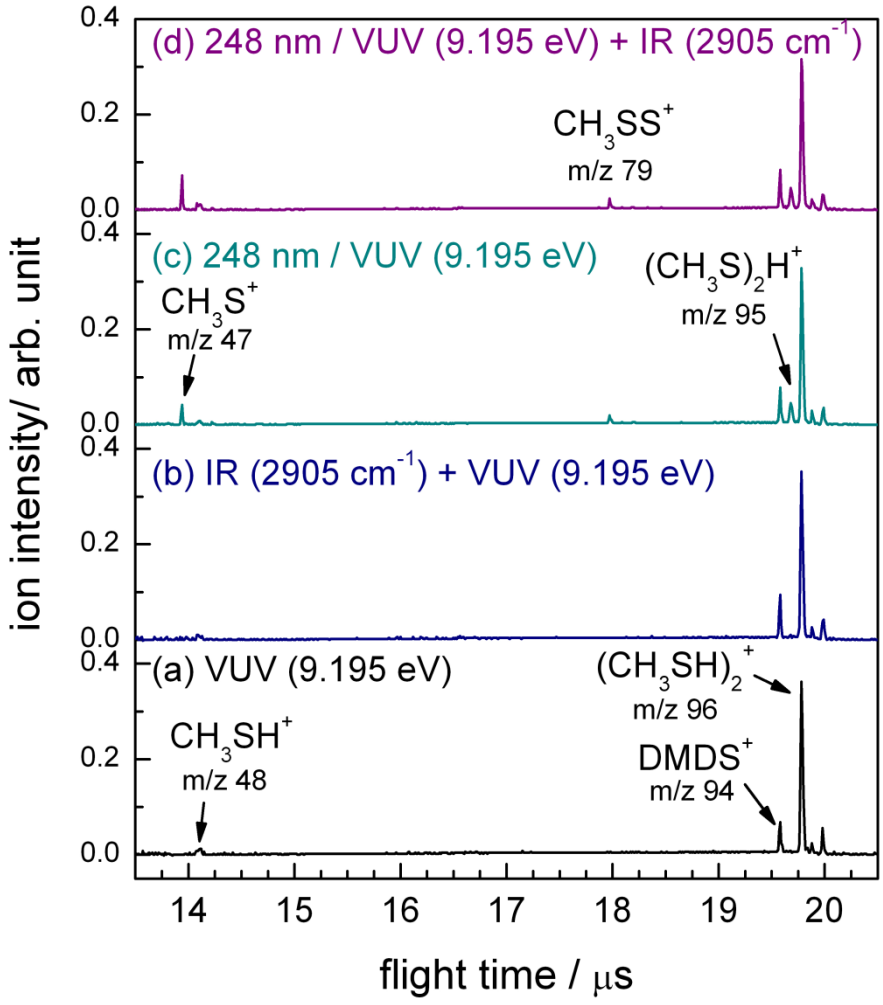


Figure 4-4 Time-of-flight spectra of a supersonic jet of Ne containing 1 % $CH_3SH$. (a) ionization with VUV light at 134.84 nm (9.195 eV, 74,165$cm^{-1}$), (b) ionization with VUV light at 134.84 nm and IR light at 2905 $cm^{-1}$ applied 200 ns before VUV light, (c) the jet was irradiated with light at 248 nm before ionization with VUV light at 134.84 nm, and (d) the jet was irradiated with light at 248 nm before ionization with VUV light at 134.84 nm and IR light at 2905 $cm^{-1}$ applied 200 ns before VUV light. $DMDS^+$ indicate $CH_3SSCH_3^+$.

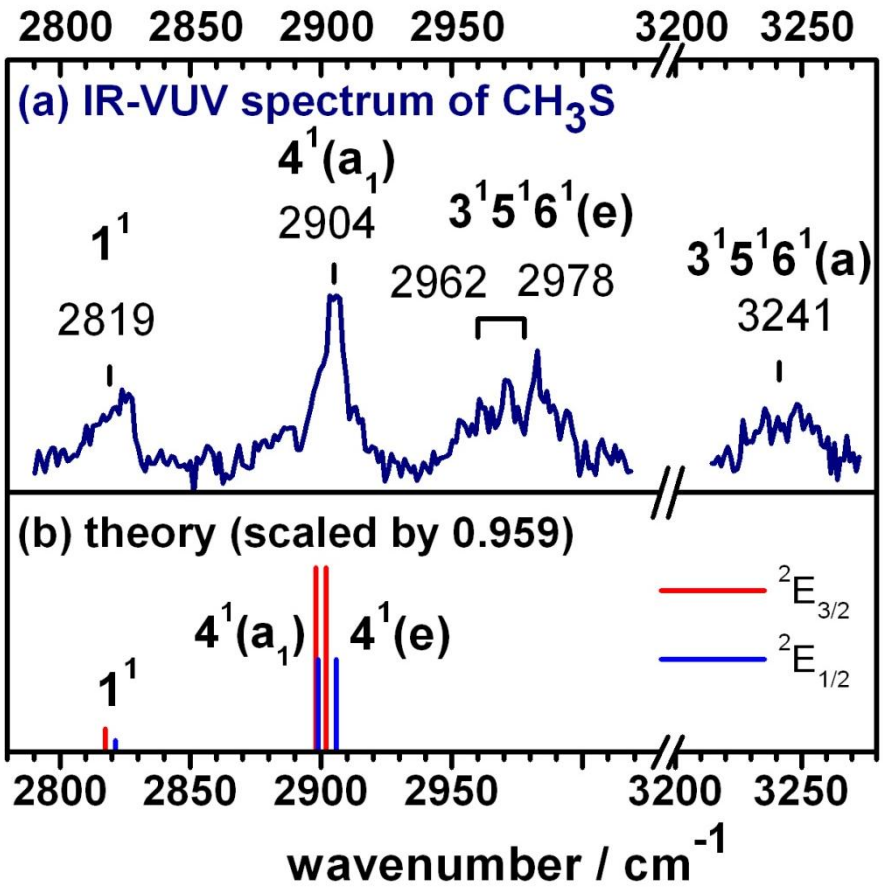


Figure 4-5 Comparison of IR spectra in regions 2790–3020 and 3200–3270 $cm^{-1}$ observed in IR-VUV photoionization experiments with the stick spectrum predicted quantum-chemically. (a) The change in intensity of the $CH_3S^+$ signal was monitored while the wavenumber of the IR laser was tuned; the wavelength of the VUV laser was maintained at 134.84 nm. (b) Stick diagram of transition wavenumbers predicted in Ref. 12; the wavenumbers are scaled by 0.959 and the statures reflect predicted relative IR intensities. Vibrational transitions from $CH_3S$ ($X\ ^2E_{3/2}$) are indicated in red and those from $CH_3S$ ($X\ ^2E_{1/2}$) are in blue, with half stature to reflect likely population relative to $CH_3S$ ($X\ ^2E_{3/2}$) upon photolysis of $CH_3SH$ at 248 nm.

## References


[1] R. J. Charlson, J. E. Lovelock, M. O. Andreae, and S. G. Warren, Nature **326**, 655 (1987).

[2] T. S. Bates, B. K. Lamb, A. Guenther, J. Dignon, and R. E. Stoiber, J. Atmos. Chem. **14**, 315 (1992).

[3] G. P. Ayers, J. M. Cainey, H. Granek, and C. Leck, J. Atmos. Chem. **25**, 307 (1996).

[4] A. R. Ravishankara, Y. Rudich, R. Talukdar, and S. B. Barone, Philos. Trans. R. Soc. London, Ser. B **352**, 171(1997).

[5] G. S. Tyndall and A. R. Ravishankara, Int. J. Chem. Kinet. **23,** 483 (1991).

[6] J. M. C. Plane, in: E. S. Saltzman and W. J. Cooper (Eds.), Biogenic Sulfur in Environment, American Chemical Society, Washington, DC, 1989.

[7] S. P. Urbanski and P. H. Wine, in: Z. B. Alfassi (Ed.), S-Centered Radicals, John Wiley & Sons, New York, 1997.

[8] I. Barnes, J. Hjorth, and N. Mihalopoulos, Chem. Rev. **106,** 940 (2006).

[9] T. A. Barckholtz and T. A. Miller, Int. Rev. Phys. Chem. **17**, 435 (1998).

[10] G. D. Bent, J. Chem. Phys. **92,** 1547 (1990).

[11] A. V. Marenich and J. E. Boggs, J. Phys. Chem. A **108,** 10594 (2004).

[12] A. V. Marenich and J. E. Boggs, J. Chem. Theory Comput. **1**, 1162 (2005).

[13] M. Suzuki, G. Inoue and H. Akimoto, J. Chem. Phys. **81**, 5405 (1984).

[14] Y.-C. Hsu, X. Liu, and T. A. Miller, J. Chem. Phys. **90**, 6852 (1989).

[15] S.-Y. Chiang and Y.-P. Lee, J. Chem. Phys. **95**, 66 (1991).

[16] B. K. Janousek, and J. I. Brauman, J. Chem. Phys. **72**, 694 (1980).

[17] R. L. Schwartz, G. E. Davico, and W. C. Lineberger, J. Electron Spectrosc. Relat. Phenom. **108**, 163 (2000).

[18] G. D. Bent, J. Chem. Phys. **89**, 7298 (1988).

[19] Michael S. Schuurman, Daniel E. Weinberg, and R. Yarkony, J. Chem. Phys. **127**, 104309 (2007).

[20] R. Fournier and A. E. Depristo, J. Chem. Phys. **96**, 1183 (1992).

[21] C.-W. Hsu, C.-L. Liao, Z.-X. Ma, P. J. H. Tjossem, and C. Y. Ng, J. Chem. Phys. **97**, 6283 (1992).

[22] L. A. Curtiss, R. H. Nobes, J. A. Pople, and L. Radom, J. Chem. Phys. **97**, 6766 (1992).

[23] Q. Cui and K. Morakuma, Chem. Phys. Lett. **263**, 54 (1996).

[24] R. D. El Bouzaidi, A. El Hammadi, A. Boutalib and M. El Mouhtadi, J. Mol. Struct. (Theochem) **497**, 197 (2000).

[25] S.-W. Chiu, W.-K. Li, W.-B. Tzeng, and C. Y. Ng, J. Chem. Phys. **97,** 6557 (1992).

[26] G. Black and L. E. Jusinski, J. Chem. Phys. **85**, 5379 (1986).

[27] P. Misra, X. Zhu, and H. L. Bryant, Jr. Pure Appl. Opt. **4**, 587 (1995).

[28] A. B. Callear, J. Connor, and D. R. Dickson, Nature **221**, 1238 (1969).

[29] A. B. Callear and D. R. Dickson, Trans. Faraday Soc. **66**, 1987 (1970).

[30] C. Anastasi, M. Broomfield, O. J. Nielson, and P. Pagsberg, Chem. Phys. Lett. **182** 643 (1991).

[31] K. Ohbayashi and H. Akimoto, I. Tanaka, Chem. Phys. Lett. **52,** 47 (1977).

[32] Y. Endo, S. Saito and E. Hirota, J. Chem. Phys. **85**, 1770 (1986).

[33] R. T. Bise, H. Choi, H. B. Pedersen, D. H. Mordaunt, and D. M. Neumark, J. Chem. Phys. **110**, 805 (1999).

[34] C.-P. Liu, Y. Matsuda, and Y.-P. Lee, J. Chem. Phys. **119**, 12335 (2003).

[35] C.-P. Liu, S. A. Reid, and Y.-P. Lee, J. Chem. Phys. **122**, 124313 (2005).

[36] M. B. Pushkarsky, B. E. Applegate, and T. A. Miller, J. Chem. Phys. **113**, 9649 (2000).

[37] P. C. Engelking, G. B. Ellison, and W. C. Lineberger, J. Chem. Phys. **69**, 1826 (1978).

[38] S. Moran and G. B. Ellison, J. Phys. Chem. **92,** 1794 (1988).

[39] Y.-Y. Lee, S.-Y. Chiang, and Y.-P. Lee, J. Chem. Phys. **93**, 4487 (1990).

[40] X. Zheng, Y. Song, J. Wu, and J. Zhang, Chem. Phys. Lett. **467**, 46 (2008).

[41] M. Bahou and Y.-P. Lee, J. Chem. Phys. **133**, 164316 (2010).

[42] Y. Matsuda, N. Mikami, and A. Fujii, Phys. Chem. Chem. Phys. **11**, 1279 (2009).

[43] H.-L. Han, C. Camacho, H. A. Witek, and Y.-P. Lee, J. Chem. Phys. **134**, 144309 (2011).

[44] P. Wang, X. Xing, K.-C. Lau, H. K. Woo, and C. Y. Ng, J. Chem. Phys. **121**, 7049 (2004).

[45] X. Xing, B. Reed, M. K. Bahng, P. Wang, H. K. Woo, S. J. Baek, C. S. Lam, and C. Y. Ng, Chin. J. Chem. Phys. **21**, 193 (2008).

[46] H. K. Woo, P. Wang, K.-C. Lau, X. Xing, C. Chang, and C. Y. Ng, J. Chem. Phys. **119**, 9333 (2003).

[47] M.-K. Bahng, X. Xing, S. J. Baek, and C. Y. Ng, J. Chem. Phys. **123**, 084311 (2005).

[48] M.-K. Bahng, X. Xing, S. J. Baek, X. Qian, and C. Y. Ng, J. Phys. Chem. A **110**, 8488 (2006).

[49] X. Xing, M.-K. Bahng, B. Reed, C. S. Lam, K.-C. Lau, and C. Y. Ng, J. Chem. Phys.

**128**, 094311 (2008).

[50] H. K. Woo, P. Wang, K.-C Lau, X. Xing, and C. Y. Ng, J. Chem. Phys. **120**, 1756 (2004).

[51] F. Brandi, W. Hogervorst, and W. Ubachs, J. Phys. B: At. Mol. Opt. Phys. **35**, 1071 (2002).

[52] S. H. S. Wilson, M. N. R. Ashfold, and R. N. Dixon, J. Chem. Phys. **101**, 7538 (1994).

[53] G. L. Vaghjiani, J. Chem. Phys. **99**, 5936 (1993).

[54] J. Segall, Y. Wen, R. Singer, M. Dulligan, and C. Wittig, J. Chem. Phys. 99, 6600 (1993).

[55] S. Nourbakhsh, K. Norwood, H.-M. Yin, C.-L. Liao, and C. Y. Ng, J. Chem. Phys. **95**, 946 (1991).

[56] T. F. Palmer and F. P. Lossing, J. Am. Chem. Soc. **84**, 4661 (1962).

[57] S. Nourbakhsh, K. Norwood, G.-Z. He, and C. Y. Ng, J. Am. Chem. Soc. **113**, 6311 (1991).

[58] B. Ruscic and J. Berkowitz, J. Chem. Phys. 97, 1818 (1992).

[59] X. J. Zhu, M. F. Ge, J. Wang, Z. Sun, and D. X. Wang, Angew. Chem. Int. Ed. **39**, 1940 (2000).

[60] C.-W. Hsu and C. Y. Ng, J. Chem. Phys. **101**, 5596 (1994).

[61] SpecView: Simulation and Fitting of Rotational Structure of Electronic and Vibronic Bands. V. L. Stakhursky, T. A. Miller, 56th Molecular Spectroscopy Symposium. http://www.chemistry.ohio-state.edu/~vstakhur

# Chapter Five

# Vibrational Stark Spectral Studies of DMANB Doped in a PMMA Film

## 5.1 Introduction

4-(dimethylamino)benzonitrile (DMABN) known to exhibit a dual fluorescence behavior in a polar solvent,[1, 2] is also a model compound of a system of electronic donor and acceptor that undergoes an intramolecular charge transfer (ICT) from a locally excited (LE) state to an ICT state following photo-excitation.[3] Two possible structures of the ICT state of DMABN are depicted in Figure 5-1(a). In the twisted intramolecular charge transfer (TICT) model, the ICT state is formed by twisting the dimethylamino group from being planar into being perpendicular to the benzene plane. The planar intramolecular charge transfer (PICT) model suggests a quinoidal planar resonance structure for the ICT state. Figure 5-1(b) shows a scheme illustrating the processes and states in the photophysics of DMABN involving a twisted intramolecular charge transfer mechanism. In this mechanism, a DMABN molecule is excited to a locally excited state, and gives a TICT state in polar environment by twisting the dimethylamino group. The dual fluorescence of DMABN in a polar solvent is explained as an overlap of fluorescence bands due to the LE and TICT states. A mechanism for planar intramolecular charge transfer is expected to involve a smaller gap of energy between two singlet excited states for the ICT reaction. Both the TICT and PICT have been applied to explain the dual fluorescence behavior of DMABN;[3–5] this topic is subject to much debate.

Ohta *et al.* measured the electric-field-induced change in electronic absorption, fluorescence, and phosphorescence spectra of DMABN doped in PMMA.[5] Though DMABN was confined in a rigid medium, which prevents a large amplitude conformational change, the ICT process is still possible when the PICT model is applicable. These authors examined the effects of the electric field on LE and ICT states. The accelerated ICT and decreased quantum yield of phosphorescence of DMABN subjected to a large external electric field indicated an enhanced photoinduced intramolecular charge transfer due to the electric field. The alteration of molecular polarizability ($\Delta\alpha$) and electric dipole moment ($\Delta\mu$) between LE/CT states and the ground state were obtained.

Stark spectra imply the difference in spectra of a sample induced with an external electric field. These spectra are analyzed to obtain the dependence upon electric field of energy levels of the excited state and transition dipoles of the associated transition. Electronic Stark spectra exhibit the effect of a field on an electronic transition, providing unique information on the differences in electric dipole moment and molecular polarizability between the ground state and the excited state.[6]

The vibrational Stark effect (VSE)[7] describes the changes in the infrared spectrum due to an electric field. As vibrational modes have widely varying Stark effects, this phenomenon is useful to separate a vibrational band from overlapping bands. One might elucidate the structures of polyatomic molecules in condensed phases using VSE. Vibrational Stark spectra, also called IR electro-absorption spectra,[8] are also useful in the study of the physics of molecular vibrations, including the anharmonicity of vibrational modes and chemical bonds perturbed with an electric field.[9, 10] This means is sensitive means to probe to external electric field in a locally structured system.[11] Vibrational Stark spectra provide information about the electric properties of molecules in liquids that are otherwise difficult to access.[12, 13] With a knowledge of the sensitivity of a vibrational frequency to an electric field – i.e. the Stark tuning

rate, the VSE serves to measure the variation of the electric field at a specific site of a protein, which results from mutations of amino acids in proteins or conformational alterations.[14, 15] The quantitative information about an electric field effect derived form the measured Stark shifts may be directly comparable with the results of electrostatics calculations.

The difference in spectra due to Stark effect typically involves small signals. For example, absorption of the C≡N stretching mode of acetonitrile only differ by 0.25 % at the wavenumber of absorption maximum (2213 $cm^{-1}$) under an applied field of 1 MV $cm^{-1}$.[7] Other samples have an even smaller Stark effect that leads to smaller difference in signals. Since a sample commonly breaks electrically at less than 1 MV $cm^{-1}$, which limits the maximal applicable voltage, and thus consequently limits the size of the signal. Hence, it is necessary to achieve low noise levels of detection. Andrew and Boxer compared the noise level in FT-IR difference measurements using DC-field detection, AC-field detection and step-scan detection methods.[16] They demonstrated that measuring vibrational Stark spectra in the IR region on an FT-IR using a DC-field method in a rapid-scan mode yields a performance superior to that with either the synchronized AC-field detection or the step-scan methods. The small noise is achieved on averaging many data points over many scans and on multiplexing.

I constructed a system for infrared electroabsorption system that is capable of measuring infrared absorption induced with an electric field with a detectivity as small as $4 \times 10^{-6}$ in the mid-infrared region (900–4500 $cm^{-1}$) using a DC electric field and an IR interferometer in its normal rapid-scan mode. In the present work, I investigated the effect of external electric field on IR absorption spectra of 4-(N,N-dimethylamino) benzonitrile (DMABN) in a film of poly(methyl methactylate) (PMMA) near 295 K. The electric-field-induced change in each vibrational line is reproduced with a superposition of the IR absorption spectrum, and its first and second derivatives, indicating that the electric dipole moments and the molecular polarizabilities of the upper and lower states of DMABN differ from those of PMMA. I

evaluated the difference of dipole moments, $\Delta\mu$, of the C≡N stretching mode of DMABN and of the C=O stretching mode of PMMA. Both the positive transition polarizabilities of these two vibrational modes and effect on orientation induced by the electric field contribute significantly to the Stark line shape.

## 5.2 Theory

### 5.2.1 Effect of Electric Field on Absorption Spectra

A vibrational stark spectrum, ΔA, is the variation of an IR spectrum under the influence of an applied electric field:

$$\Delta A = A(F \neq 0) - A(F = 0) \quad (1)$$

The effects of an electric field on a molecular vibration arise from the interaction of the electric field with the difference in dipole moment of the vibration and in molecular polarizability between the ground state and an excited state; those properties are expected to cause a small frequency shift in the absorption spectrum. The frequency shift of a molecular transition, $\Delta\nu$ (in $cm^{-1}$), due to an external electric field, $\vec{F}$, is given by

$$\Delta\nu = -\frac{1}{hc}(\Delta\vec{\mu}\cdot\vec{F} + \vec{F}\cdot\Delta\alpha\cdot\vec{F}/2) \quad (2)$$

in which $h$ is the Planck constant and $c$ is the speed of light. $\Delta\vec{\mu}$ and $\Delta\alpha$ are the differences in dipole moment of the vibration and in molecular polarizability, respectively, between the ground state (g) and an excited state (e); i.e., $\Delta\vec{\mu} = \mu_e - \mu_g$ and $\Delta\alpha = \alpha_e - \alpha_g$. The sign of $\Delta\alpha$ is typically, but not invariable, greater in the excited state than in the ground state. The two terms in Eq. (2) are also known as the linear and quadratic Stark effects,

respectively.

For an isotropic and immobilized sample, the application of an electric field produces line broadening due to the change in dipole moment, in which $\Delta\vec{\mu}$ is oriented parallel or antiparallel to the electric field and the transition energy is shifted to greater or lesser energy; and the Stark spectrum has the shape of a second derivative of the absorption spectrum. This condition is illustrated in Figure 5-2 for a symmetric Gaussian line. If the change in molecular polarizability is significant, the presence of electric field produces a line shift, so that the Stark spectrum has the shape of the first derivative of an absorption spectrum, as shown in Figure 5-2. All these effects might occur simultaneously, the Stark spectrum, ΔA(ν), may be expressed as a sum of the zeroth, first, and second derivatives of the absorption spectrum A(ν):[18]

$$\Delta A(\nu) = (f\boldsymbol{F})^2 \left\{ a' A(\nu) + b' \nu \frac{d[A(\nu)]}{d\nu} + c' \nu \frac{d^2[A(\nu)]}{d\nu^2} \right\}, \tag{3}$$

in which $f$ is a correction factor for the local field, $\boldsymbol{F}$ is the externally applied field, and $a'$, $b'$, and $c'$ are coefficients of the zeroth, first and second derivatives. The factor $a'$ depends on the transition polarizability and hyperpolarizability that reflects the influence of the electric field on the transition moment, $\vec{M} : \vec{M}(\vec{F}) = \vec{M} + A \cdot \vec{F} + \vec{F} \cdot B \cdot \vec{F}$, in which $A$ and $B$ are tensors for the transition polarizability and transition hyperpolarizability, respectively. Coefficient $a'$ hence yields the alteration of absorption intensity. The coefficient $b'$ and $c'$ are expressed in these forms:

$$b' = \frac{\Delta\bar{\alpha}/2 + (\Delta\alpha_M - \Delta\bar{\alpha})(3\cos^2\chi - 1)/10}{hc}, \tag{4}$$

$$c' = (|\Delta\vec{\mu}|)^2 \frac{\left[5 + (3\cos^2\xi - 1)(3\cos^2\chi - 1)\right]}{30h^2c^2}, \tag{5}$$

in which $\Delta\bar{\alpha}$ denotes the trace of $\Delta\alpha$, $\Delta\bar{\alpha}=\left(\frac{1}{3}\right)Tr(\Delta\alpha)$. $\Delta\alpha_M$ is the diagonal component of with respect to the direction of the transition moment, i.e., $\Delta\alpha_M=(\vec{M}\cdot\Delta\alpha\cdot\vec{M})/|\vec{M}|^2$. $\chi$ is the experimental angle between the direction of ***F*** and the electric vector of the probing light. $\xi$ is the molecule-fixed angle between the direction of $\Delta\vec{\mu}$ and $\vec{M}$. The magnitudes of $\Delta\vec{\mu}$ and $\xi$ are obtainable from Stark spectra recorded at multiple values of $\chi$ that are fitted to a sum of the derivatives of the absorption spectrum. At a magic angle, $\chi$ = 54.7°, at which $3\cos^2\chi-1=0$, the coefficients $b'$ and $c'$ become simplified as

$$b'=\frac{\Delta\bar{\alpha}}{2hc}, \text{ and} \tag{6}$$

$$c'=\frac{|\Delta\vec{\mu}|^2}{6h^2c^2}. \tag{7}$$

According to these equations, the value of magnitudes of $\Delta\vec{\mu}$ and $\Delta\bar{\alpha}$ can be directly obtained, to be shown in next section. For one-dimensional vibrational modes such as C≡N and C=O stretching modes, the angle between the transition moment and $\Delta\vec{\mu}$ is approximate $0^\circ$ (=$\xi$).[7] With experimental angle $\chi$ set to 90°, the magnitude of $\Delta\vec{\mu}$ is extracted directly from the coefficient of the second derivative ($3\cos^2\xi-1=2$, $3\cos^2\chi-1=-1$), as

$$|\Delta\mu|=(10h^2c^2c')^{1/2}. \tag{8}$$

Because the sample experiences an internal electric field that depends on the dielectric properties of the environment, the correction factor $f$ for the local field has to be used to correct for the difference between the externally applied field and the internal field. This correction can be modeled in various ways, a simpler approach uses the Lorentz field correction for the internal field, i. e. $f$ = (ε + 2) /3, in which ε is the dielectric constant of the

material.[17] However, *f* is inaccurate with this simple model, the reported values of $|\Delta\mu|$ and $\Delta\bar{\alpha}$ are thus in units of Debye/*f* and Å $^3$/*f*$^2$, respectively, in order to take the uncertainties in f into account.

It is worth notingthat the Stark effect theory[18] is based on several simplified assumptions:

(1) For individual molecules subjected to the electric field, the absorption band of a given electronic transition only shifts in the frequency, but does not change its shape. The change of the band shape is the result of the ensemble average over the molecules experiencing different Stark shifts.

(2) The angular distribution of molecules without the external field is isotropic.

(3) The field perturbations to the individual transitions are small compared to their line widths and intensities, that is, the absorption features are much broader than the Stark shift.

(4) The applied field is not strong enough to induce orientational realignment, i.e., $\mu F / kT << 1$.

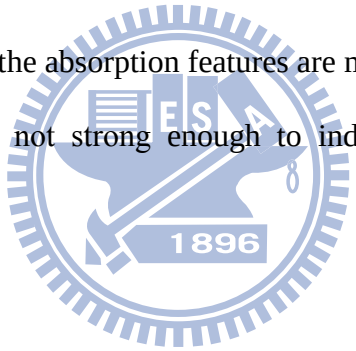

### 5.2.2 Derive Values of $|\Delta\mu|$ and $\Delta\bar{\alpha}$

The Stark spectrum fitted with Eq. (3) gives the fitting coefficients: $A_{fit}$, $B_{fit}$, and $C_{fit}$.

$$B_{fit} = b' \cdot (fF)^2 \cdot \left( \frac{-1}{\text{cm}^{-1}} \right) \tag{9}$$

at the magic angle, $\chi$ = 54.7°,

$$\Delta\bar{\alpha} = 2hc\cdot b' = -2\frac{B_{fit}}{(f\boldsymbol{F})^2}\cdot(\mathrm{cm}^{-1})\cdot(6.626\times10^{-34}\ \mathrm{J\cdot s})\cdot(2.998\times10^{8}\ \mathrm{m\cdot s^{-1}}) \tag{10}$$

$$= -2\frac{B_{fit}}{(f\,\mathrm{F_{value}})^2}\cdot\left(\frac{\mathrm{cm}}{\mathrm{MV}}\right)^2\cdot\mathrm{J\cdot m}\cdot(\mathrm{cm}^{-1})\cdot(19.86\times10^{-26})$$

$$= -35.7\cdot\frac{B_{fit}}{(\mathrm{F_{value}})^2}\ \mathring{\mathrm{A}}^3\Big/f^2$$

in which

$$\left(\frac{\mathrm{cm}}{\mathrm{MV}}\right)^2\cdot\mathrm{J\cdot m}\cdot(\mathrm{cm}^{-1}) = 10^{-14}\ \mathrm{C\cdot m^2\cdot V^{-1}} = 10^{-14}\cdot\left(\frac{10^6}{4\pi\varepsilon_0}\right)\cdot(10^8)^3\ \mathring{\mathrm{A}}^3 = 8.99\times10^{25}\ \mathring{\mathrm{A}}^3.$$

$$C_{fit} = c'\cdot(f\boldsymbol{F})^2\cdot\frac{2}{(\mathrm{cm}^{-1})^2} \tag{11}$$

at a magic angle,

$$|\Delta\mu|^2 = 6h^2c^2\cdot\frac{C_{fit}}{(f\boldsymbol{F})^2}\cdot\frac{(\mathrm{cm}^{-1})^2}{2} \tag{12}$$

$$|\Delta\mu| = \sqrt{3}\cdot hc\cdot\frac{\sqrt{C_{fit}}}{(f\boldsymbol{F})}(\mathrm{cm}^{-1})$$

$$= \frac{\sqrt{3\cdot C_{fit}}}{(f\,\mathrm{F_{value}})}\left(\frac{\mathrm{cm}}{\mathrm{MV}}\right)\cdot(\mathrm{cm}^{-1})\cdot(6.626\times10^{-34}\ \mathrm{J\cdot s})\cdot(2.998\times10^{8}\ \mathrm{m\cdot s^{-1}})$$

$$= \frac{\sqrt{3\cdot C_{fit}}}{(f\,\mathrm{F_{value}})}\cdot(19.86\times10^{-32})(\mathrm{C\cdot m})$$

$$= 0.103\cdot\frac{\sqrt{C_{fit}}}{(\mathrm{F_{value}})}\ \mathrm{D}\Big/f$$

in which J = C V, 1 D (Debye) = $3.336\times10^{-30}$ C m.

For C≡N and C=O stretching modes, with the assumption of one-dimensional motion, the angle between the transition moment and $\Delta\vec{\mu}$ is approximate 0° (=$\xi$).[7] With $\chi$ = 90°,

$$|\Delta\mu| = \sqrt{5}\cdot hc\cdot\frac{\sqrt{C_{fit}}}{(f\boldsymbol{F})}(\mathrm{cm}^{-1}) = 0.133\cdot\frac{\sqrt{C_{fit}}}{(\mathrm{F_{value}})}\ \mathrm{D}\Big/f\ .$$

The data analysis of Stark spectra is described in appendix A.

## 5.3 Material and Methods

### 5.3.1 Sample Preparation

4-(N, N-dimethylamino) benzonitrile (DMABN, Aldrich), poly(methyl methacrylate) (PMMA, MW=75,000, Aldrich), and solvent toluene (Aldrich) was used without further purification. Figure 5-3 shows the chemical structure of DMABN and PMMA. Sample preparation for DMABN doped in a PMMA film is described in the following procedures. First, 250 mg of PMMA was dissolved in 5 ml of toluene before being heated at 40 ℃ and stirred for 8 hr to ensure PMMA was fully dissolved. In, a separate solution, 183 mg of DMABN was dissolved in 5 ml of toluene, followed by adding into the PMMA solution to prepare a solution containing 50 mol % of DMABN in PMMA. The solution was then sonicated for 1 hr to ensure DMABN was well dispersed. The first electrode film was made by vacuum vapor deposition of Nickel (Ni) on $CaF_2$ plate (30 mm in diameter, 1.5 mm in thickness) with a deposition rate of 0.5 Å /s. The thickness of the electrode is about 80 Å. A small amount of solution was casted on the Ni surface of the $CaF_2$ plate and was spin coated with a spin speed of 500 rpm for 10 s and 2000 rpm for 60 s, followed by baking at 323 K for 30 min, and dried at room temperature under $N_2$ for 12 hr. The thickness of the polymer film was typically 0.5 μm. Subsequently, a $SiO_2$ layer (thickness ~100 nm) was deposited on the polymer film by the electron-beam deposition technique, followed by evaporation of the top Ni electrode (thickness ~150 Å). Finally, make cables with silver paste at the edge of Ni films. Figure 5-4 shows a schematic of the structure of the sample. The thicknesses of Ni, $SiO_2$, and polymer films were measured by a thin film thickness microscope (MP100-M, Mission Peak Optics).[19] The first layer of Nickel typically has a resistance of about 300 Ω across the surface on the $CaF_2$ plate, whereas the second layer of Nickel has a resistance of

about 1 kΩ due to roughness of the polymer layer.

### 5.3.2 Rapid Scan FTIR

The field-induced changes in IR absorption spectra were recorded on an interferometer (a Bruker VERTEX 80v, mirror scan velocity = 20 kHz, HgCdTe detector, cooled with liquid $N_2$. Figure 5-5(a) shows a schematic of the experiment apparatus. By feeding the external TTL pulses from the trigger interface module (E525/Z, Bruker) into the pulse generator (DG 535, Stanford Research) as a trigger, the external voltage cycle that comprises of rectangular waves of positive, zero, and negative voltage is generated by the DG535, followed by amplifying through a high voltage amplifier (HA-800); the output voltage was synchronized with the scan of the interferometer. A sequence of commands to control the timing of the measurement is described in the appendix B. We alternatively applying positive and negative voltages in turn to the sample is useful both to avoid an accumulation of charge in the sample and also to prevent sample poling. The $CaF_2$ plate, was placed in the sample holder, was put in the sample chamber where IR light passes through the center of the $CaF_2$ plate. The sample holder was set on a rotatory stage that served to vary the angle between the direction of the applied electric field and the electric vector of the excitation light. The size of beam spot on the $CaF_2$ plate was in the range of 2 to 6 mm. Two layers of the Ni film transmitted 5–10 % of incident light throughout the mid IR region. The nickel electrodes were connected to the voltage amplifier.

The Stark spectra were measured by applying the DC method and recording the spectra with the FTIR in its normal rapid-scan mode with resolution 1 $cm^{-1}$ (the greatest resolution of FTIR is 0.08 $cm^{-1}$). Figure 5-5(b) shows the time chart for data collecting. Using the DC method, ten rapid scans were made with the field off, then 10 scans with a positive voltage

applied to the sample, and then a negative voltage applied to the sample. Each pulse of applied voltage has a duration of about 10 s. Alternative interferogram scans of the cycle with and without applied field were repeated at least 200 times, i.e., 200 loops. At the end, the interferograms with field-on and off were averaged and Fourier transformed. The Stark spectrum was obtained by taking the logarithm of the field-on and field-off spectra as according to the following equation,

$$\log\left(\frac{I_{V=o}}{I_{V=V}}\right)=\log\left(\frac{I_{background}}{I_{V=V}}\times\frac{I_{V=o}}{I_{background}}\right)=\log\left(\frac{I_{background}}{I_{V=V}}\right)-\log\left(\frac{I_{background}}{I_{V=0}}\right) \quad (9)$$
$$=A_{V=V}-A_{V=0}=\Delta A$$

All measurements were performed near 298 K under evacuated conditions. For all samples, the spectra were recorded for at least two different applied fields. In all experiments, I used an unpolarized infrared source. The electric field was applied typically at the normal incidence ($\chi$ = 90°) and the magic angle ($\chi$ = 54.7°) relative to the direction of electric field of the infrared light. To obtain a Stark spectrum with adequate ratio of signal- to- noise, I applied the electric field to the sample parallel ($\chi$ = 90°) to the IR beam so that unpolarized light was applicable.

## 5.4 Results and Discussion

Figure 5-6 shows the IR absorption spectrum and vibrational Stark spectrum of PMMA in the region1100–3250 $cm^{-1}$. The IR spectrum was normalized with the absorption maximum. The IR spectrum of PMMA is studied. The observed IR spectrum is similar to that in previous reports.[20–23] The IR spectrum show a sharp and intense line at 1732 $cm^{-1}$, which is assigned to be the C=O asymmetric stretching mode. The broad features in the region 2800 to 3050

$cm^{-1}$ are associated with C–H stretching modes. The $CH_2$ bending and wagging modes are found in the range 1300–1500 $cm^{-1}$. The broad line ranging from 1050–1260 $cm^{-1}$ is assigned to the C-O-C (ester bond) stretching vibration, skeletal stretching coupled with internal C-H deformation.[22] As shown in the vibrational Stark spectrum (with $\chi = 90°$) in Figure 5-6(b), the C=O stretching mode exhibits the largest magnitude of the field-induced change and gives a shape similar to the first derivative of the absorption spectrum. Figure 5-7 shows the amplitude of the VSE of the C=O stretching mode as a function of strength of the applied electric field. The shape of the vibrational Stark spectrum remains unchanged with the field in the range 0.75–1.25 MV $cm^{-1}$. Moreover, the intensity (peak height) of Stark signal with applied field at 0.75 and 0.875 MV $cm^{-1}$ were observed to be proportional to the square of the strength of the applied electric field as expected.[6] However, the Stark signal at 1.25 MV $cm^{-1}$ is leveling off, this might be due to sample degradation. Figure 5-8 shows the vibrational Stark spectrum of PMMA in the range 1000–1475 $cm^{-1}$ at three applied fields. The field-induced signal increases with increasing strength of electric field, the intensity of Stark signals at 1147 and 1239 $cm^{-1}$ (marked * in Figure 5-8(a)) were observed to be proportional to the square of the strength of the applied electric field. The complex band structure from various vibrational modes in this region makes the analysis difficult.

Figure 5-9 shows the IR absorption spectrum and vibrational Stark spectrum (with $\chi = 90°$) of DMABN doped in a PMMA film in the region 1050–3300 $cm^{-1}$. Relative with Figure 5-6(a), the IR spectrum in Figure 5-9(a) shows additional lines at 2213, 1609, 1526, and 1370 $cm^{-1}$, ascribable to C≡N stretching, phenyl C=C stretching ($\nu_{8a}$), phenyl C=C stretching ($\nu_{19a}$), and phenyl-N stretching modes, respectively.[24] These vibrational lines indicate characteristic field dependence on the strength of electric field as shown in Figure 5-9(b). The shape of the vibrational Stark spectrum of the C≡N stretching band is similar to that of the first derivative

of the absorption spectrum, whereas the zeroth and second derivative components are dominant for the phenyl C=C stretching and the phenyl-N stretching modes. It is worth noting that, although the C≡N stretching and the phenyl C=C stretching modes have only small absorbance, both them have significant field-induced signal in Stark spectrum. This effect demonstrates the advantage of the VSE to observe weak absorption from buried lines. Figure 5-10(a) shows the vibrational Stark spectra, under magic angle condition, collected with 200 and 700 loops. The amplitude of the Stark signals in the spectrum taken with 700 loops is only half that in in the spectrum taken with 200 loops. Figure 5-10(b) shows the residual spectrum obtained on subtracting the spectrum for 200 loops with that for 700 loops that doubled. The shape of the vibrational Stark spectrum temporally invariant implies that the decreased signal might be due to the degradation of the Ni electrode films after protracted measurement. That the transmittance of the infrared light increases after the measurement indicates also that some Ni film might be vaporized because of the applied voltage. The noise amplitude in the spectrum recorded with 700 loops is half that in the spectrum recorded with 200 loops. This ratio of signal-to-noise is hence similar for the two spectra. Figure 5-11 compares the vibrational Stark spectra recorded under the condition of normal incidence and the magic angle. Although the two spectra cannot be quantitatively compared, the Stark signals with the angular ( $\chi$ ) dependence can still enable qualitative observations.

Figure 5-12 shows the vibrational Stark spectrum and contributions of each component (zeroth, first, second derivatives) of PMMA for the C=O stretching mode under the condition of normal incidence. Figure 5-13 shows vibrational Stark spectrum and contributions of each component for DMABN doped in a PMMA film in the C≡N stretching region under the condition of normal incidence. These lines are satisfactorily reproduced with a linear combination of the absorption spectrum and its first and second derivatives. The $|\Delta\mu|$ values

of the C=O stretching and C≡N stretching modes are evaluated to be 0.016 ± 0.003 and 0.012 ± 0.005 D/*f*, respectively. The magnitude of $|\Delta\bar{\alpha}|$ for C=O stretching and C≡N stretching modes are evaluated to be 0.19 ± 0.004 and 2.33 ± 0.02 $Å^3/f^2$, respectively.

As C=O stretching and C≡N stretching vibrations may be regarded as one-dimensional motion systems, the corrections for the Stark signal with various angle χ angles are insensitive to the one-dimensional systems for small rotation angles and unpolarized light.[7] According to the measurements of χ-dependence by Boxer *et al.*, with an assumption of the maximum possible ξ angle of 90 ° and the maximum sample rotation angle χ of 20 °, the correction in factor *c′* is derived to be 13 %, contributing to a 7 % error in the calculation of the magnitude of $\Delta\vec{\mu}$.[7] Figure 5-14 and Figure 5-15 shows the vibrational Stark spectrum and the simulated spectrum of DMABN doped in PMMA for the C=O stretching and the C≡N stretching modes with experimental angle χ = 54.7°. The $|\Delta\mu|$ values of the C=O stretching and C≡N stretching are evaluated to be 0.013 ± 0.001 and 0.013 ± 0.004 D/*f*, respectively. The magnitude of $|\Delta\bar{\alpha}|$ for the C=O stretching and the C≡N stretching modes are evaluated to be 0.099 ± 0.001 and 0.730 ± 0.001 $Å^3/f^2$, respectively. The evaluated $|\Delta\mu|$ values from the VSE spectra measured at the condition of magic angle are close to those values from the VSE spectra measured at the condition of normal incidence angle. However, for the C=O stretching and the C≡N stretching modes, the evaluated $|\Delta\bar{\alpha}|$ values measured at the condition of magic angle are 52 % and 31 % of those measured at the condition of normal incidence angle, respectively.

Since the zeroth derivative term in Eq. (3) is ascribed to the change in absorption intensity arising from the deviation of the transition dipole from the isotropic distribution due to alignment and orientation of the molecules along the field direction.[25] When the zeroth

component in the normal incident case is much larger than that in the magic angle case, indicates that the field-induced orientational effect is not negligible.[26] As the Stark spectra in the C=O stretching and the C≡N stretching regions have a major contribution from the first derivative term, these vibrations are considered to have a significant large $|\Delta\bar{\alpha}|$ value, which might result from the field-induced orientation of the dopant molecule and of the polar groups in the polymer matrix. Chowdhury *et al.*[27] found that the PMMA samples dried for 24 h at room temperature have a first-derivative contribution that is about ten times larger than that of the samples heated at 150 ℃ for 5 min. Consequently, the measured polarizability change ($\Delta\bar{\alpha}$) obtained for unheated sample was about ten times larger than that for heated sample. The measured $\Delta\bar{\alpha}$ for a glued PMMA and a heated PMMA are 564 and 60 $Å^3$, respectively. Heating effect on $|\Delta\vec{\mu}|$ is negligible small. This result shows that unheated PMMA has less rigidity, which leads to the dominance of the field-induced dipolar orientation effect. In our results, the large first-derivative contribution observed in the vibrational spectrum of PMMA, especially for the C=O stretching and the C-O-C stretching modes, is thus explained as an effect of orientation induced by the electric field.

In the present work, DMABN molecules are regarded as being randomly distributed in a PMMA film. As the glass transition temperature of PMMA (387 K) is much above room temperature, the transitional and rotational motions on DMABN in PMMA are expected to be restricted, but the degree of restriction in PMMA might depend on the concentration of DMABN and on the interaction between DMABN and PMMA, which is not well studied. Chowdhury *et al.*[27] found that the measured values of $\Delta\bar{\alpha}$ and $\Delta\vec{\mu}$ for a doped-dye molecule (Coumarin 153) varied with the temperature of the polymer matrix. Their results show that decreasing the temperature of the polymer matrix leads to a significant decrease in the measured $\Delta\bar{\alpha}$ and a slight increase in the measured $\Delta\vec{\mu}$. For example, the measured

$\Delta\bar{\alpha}$ of Coumarin 153 doped in a PE matrix at 298 and 77 K are 374 and 26 Å$^3$, respectively, and the measured $\Delta\vec{\mu}$ are 4.4 and 5.3 D, respectively. Temperature effect on $|\Delta\vec{\mu}|$ is less significant than that on $|\Delta\bar{\alpha}|$. The values for $\Delta\bar{\alpha}$ of a dye molecule in polyvinyl chloride (PVC) and in organic glasses at 77 K show a minimum because of a diminished effect of orientation induced by the field. The electro-absorption spectrum of DMABN doped in PMMA film in the region 25,000–40,000 cm$^{-1}$ recorded by Yoshizawa *et al.*[5] shows a shape of the first derivative of the absorption spectrum, indicating that the field-induced orientation effect on a DMABN molecule is significant. The measured $|\Delta\vec{\mu}|$ and $|\Delta\bar{\alpha}|$ of the C≡N stretching mode are compared in Table 5-1 with values reported in Ref. 7. The magnitudes of $|\Delta\vec{\mu}|$ and $|\Delta\bar{\alpha}|$ for the C≡N stretching mode of aromatic nitriles were reported to be in the range of 0.1 to 0.5 D/*f* and 0.02 to 0.9 Å$^3$/*f*$^2$. In the present work, the measured $|\Delta\bar{\alpha}|$ for the C≡N stretching mode is significantly larger than the values obtained for aromatic nitriles in the organic glasses at 77 K,[7] and the measured $|\Delta\vec{\mu}|$ for C≡N stretching mode is slightly smaller than the values obtained for aromatic nitriles in organic glasses at 77 K, both conditions are explained in terms of a thermal motion that induces the orientation in the presence of ***F***.

## 5.5 Conclusion

A system for vibrational Stark spectroscopy that is capable of detection of relative changes induced with electric field with great sensitivity as small as $4 \times 10^{-6}$ in the mid-infrared region has been implemented. The spectra were measured by using a DC electric

field and recording with a FTIR in its normal rapid-scan mode. With this system, the effect of external electric field on IR absorption spectra of 4-(N,N-dimethylamino) benzonitrile (DMABN) in a film of poly(methyl methactylate) (PMMA) have been investigated. The difference in the dipole moment $\Delta\mu$, for the C=O stretching mode at 1732 $cm^{-1}$ of PMMA and for the C≡N stretching mode at 2213 $cm^{-1}$ of DMABN are determined to be 0.016 and 0.012 D/*f*, respectively, and the difference in the molecular polarizabilities $|\Delta\alpha|$, are determined to be 0.19 and 2.33 $Å^3/f^2$, respectively. Moreover, the large changes in polarizability of the C=O stretching and the C-O-C stretching modes of PMMA might indicate the presence of ***F*** affect significantly the molecular orientation on side chains. The effect on orientation induced by electric field might further induce a dielectric polarizability that yields large polarizability change. As the Stark signal is sensitive to the molecular motion, even for molecule doped in a polymer at a temperature below its glass-transition temperature. It is thus necessary to apply a cryostat with immersion of a sample in liquid nitrogen[28] to perform a quantitative evaluation of $|\Delta\bar{\alpha}|$ and $|\Delta\vec{\mu}|$ for molecules in a rigid cage.

Table 5-1 Comparison of vibrational Stark effect data of the C≡N stretching mode with literature values.

| compound | $\bar{\nu}$ (cm$^{-1}$) | $\lvert\Delta\vec{\mu}\rvert$ (D/*f*) | $\lvert\Delta\bar{\alpha}\rvert$ (Å$^3$/*f*$^2$) |
|---|---|---|---|
| DMABN[a] | 2213 | 0.012 ± 0.005 | 2.33 ± 0.02 |
| benzonitrile[b] | 2227.8 | 0.0361 | 0.65 |
| 1,2-dicyanobenzene[b] | 2235.3 | 0.0263 | 0.60 |
| 1,3-dicyanobenzene[b] | 2236.3 | 0.0330 | 0.71 |
| 1,4-dicyanobenzene (A)[b] | 2231.7 | 0.0196 | 0.89 |
| 1,4-dicyanobenzene (S)[b] | 2243.7 | 0.0125 | 0.43 |
| 2-Cl-benzonitrile[b] | 2232.1 | 0.0306 | 0.35 |
| 3-Cl-benzonitrile[b] | 2232.7 | 0.0318 | 0.23 |
| 4-Cl-benzonitrile[b] | 2230.6 | 0.0348 | 0.26 |
| 4-methoxybenzonitrile[b] | 2223.5 | 0.0497 | 0.02 |

[a] This work. 4-(N,N-dimethylamino) benzonitrile doped in a PMMA film. Spectrum was measured at 298 K.

[b] From Table 2 in Ref. 7. Compounds were dissolved in 2-MeTHF solvent, at 74 K.

(a)

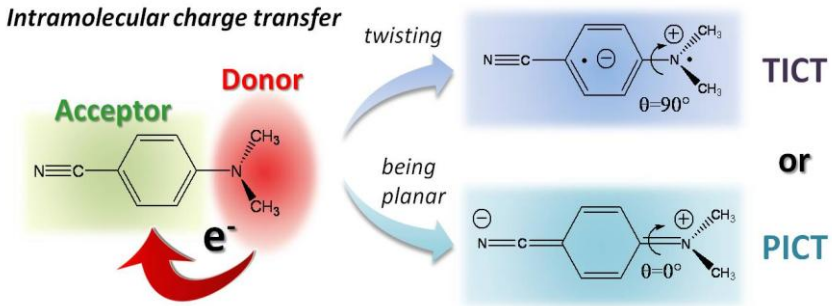


(b)

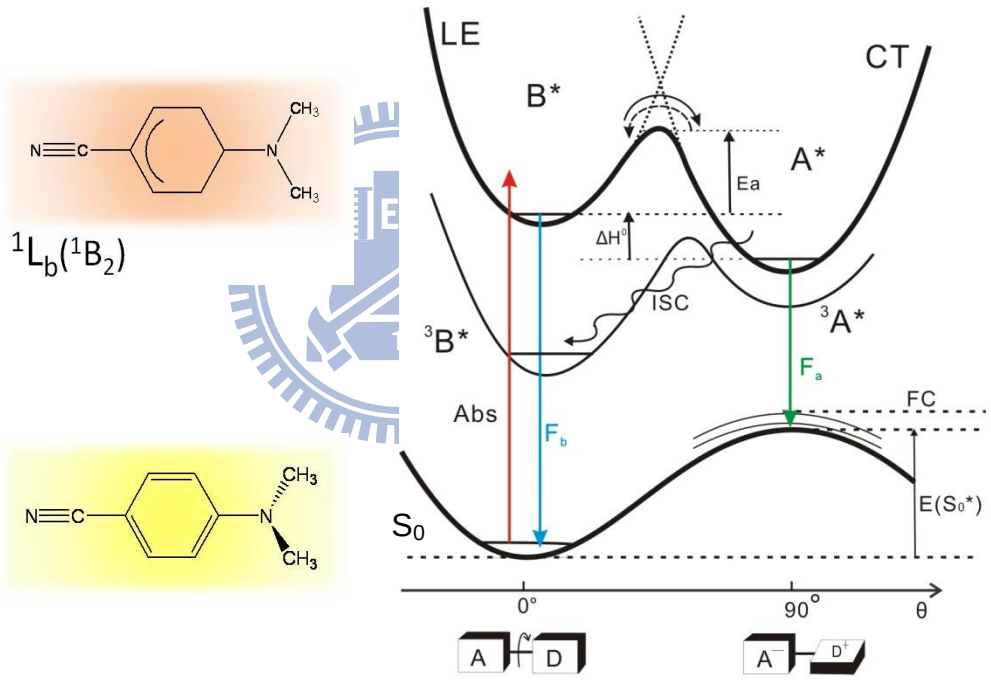


Figure 5-1 (a) Two possible mechanisms of intramolecular charge transfer process. The structures of twisted intramolecular charge transfer (TICT) state and the planar intramolecular charge transfer (PICT) state are shown. (b) Schematic illustration of the processes and states involved in the photophysics of DMABN according to the mechanism of twisted intramolecular charge transfer.

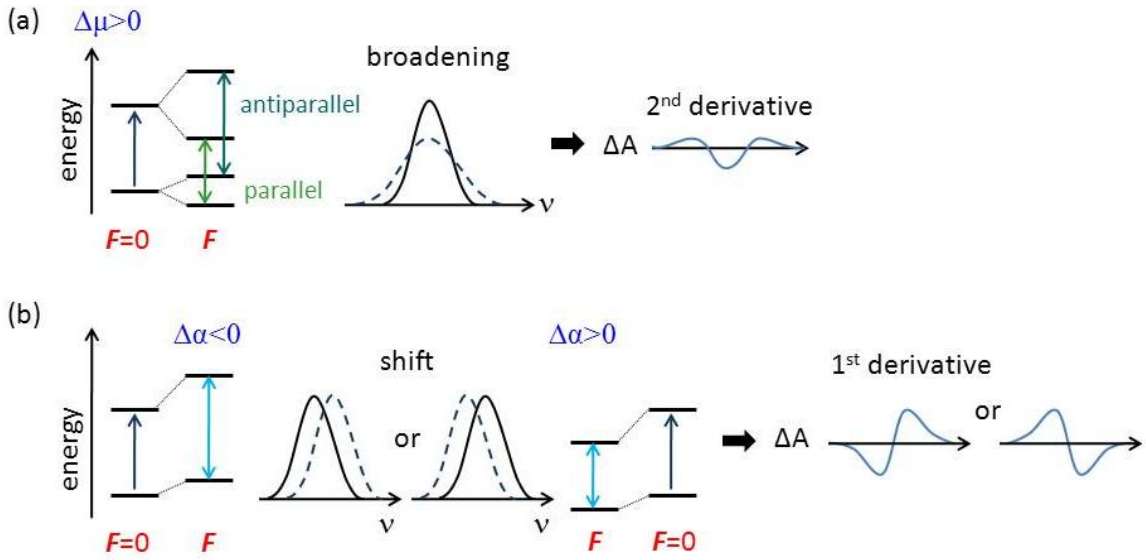


Figure 5-2 Schematic illustration of effects of an applied electric field on the shape of an absorption line. (a) Molecules of which $\Delta\vec{\mu}$ (shown here for $\Delta\vec{\mu}>0$) is oriented parallel or antiparallel to the electric field ***F*** have their transition energy shifted to smaller or greater energy, respectively. The consequence for the absorption spectrum (solid and dashed lines denote the spectrum without and with an applied electric field) is shown on the right: some orientational subpopulations are shifted to smaller energy, some to greater energy, and some remain the same, resulting in a broadened band. The Stark spectrum has a second derivative line shape as shown. (b) The applied field induces a dipole moment that is typically in the direction of the applied field, regardless of the orientation of the molecule. The absorption energy shifts towards smaller or greater energy depending on $\Delta\alpha>0$ or $\Delta\alpha<0$, and a line in the Stark spectrum has a positive or negative first-derivative shape.

**PMMA**

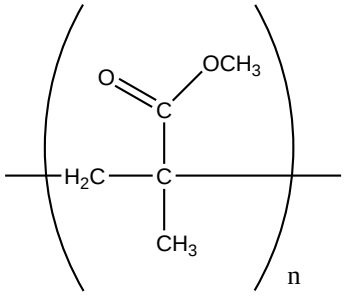


**DMABN**

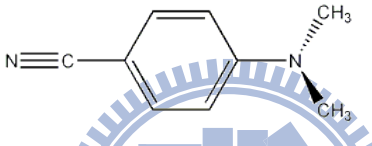


Figure 5-3 Chemical structures of PMMA and DMABN.

(a) (b)

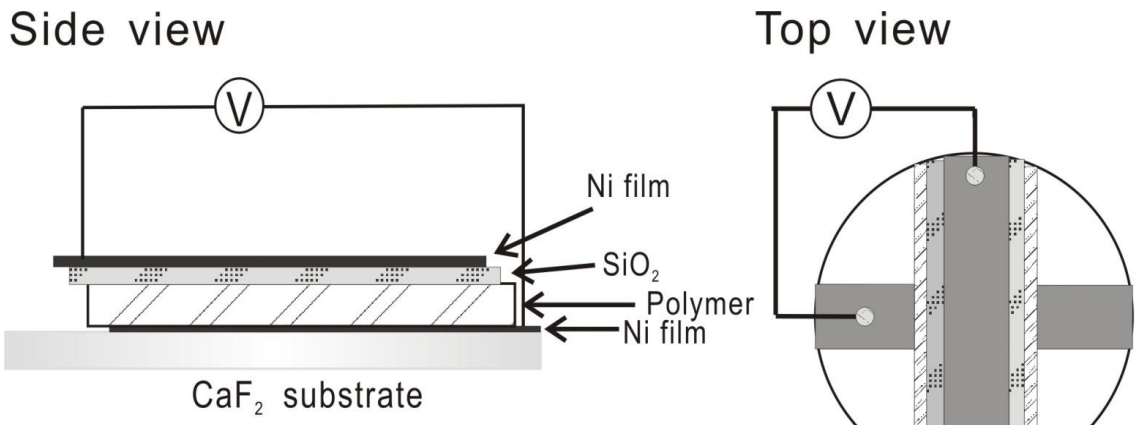


Figure 5-4 Schematic illustration of the device. (a) The side view. (b) The top view.

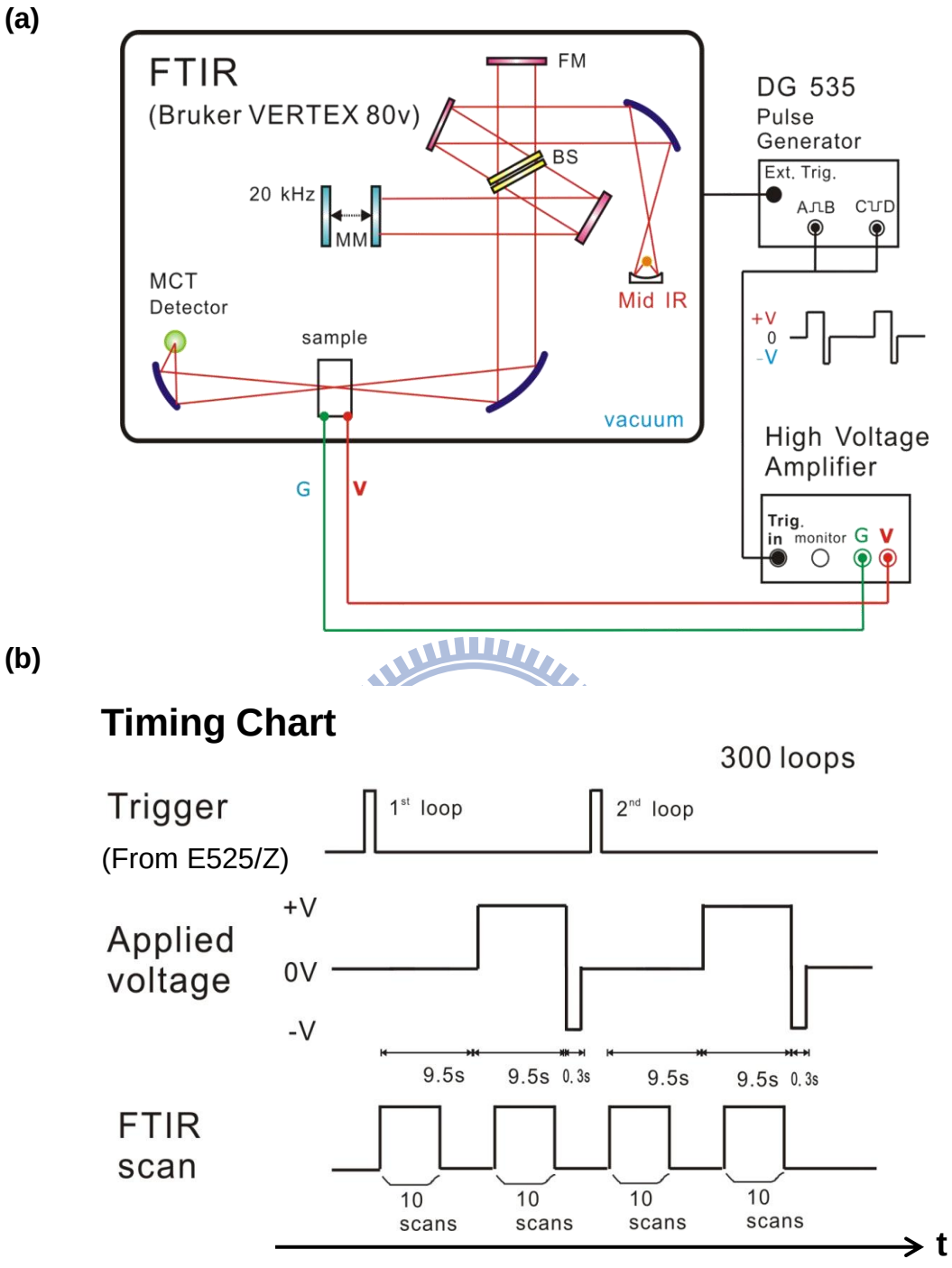


Figure 5-5 (a) Experimental setup for vibrational Stark spectroscopy. BS, FM, and MM represent the KBr beamsplitter, fixed mirror, and moving mirror, respectively. (b) Timing chart for the measurement using the DC electric field method in rapid-scan mode.

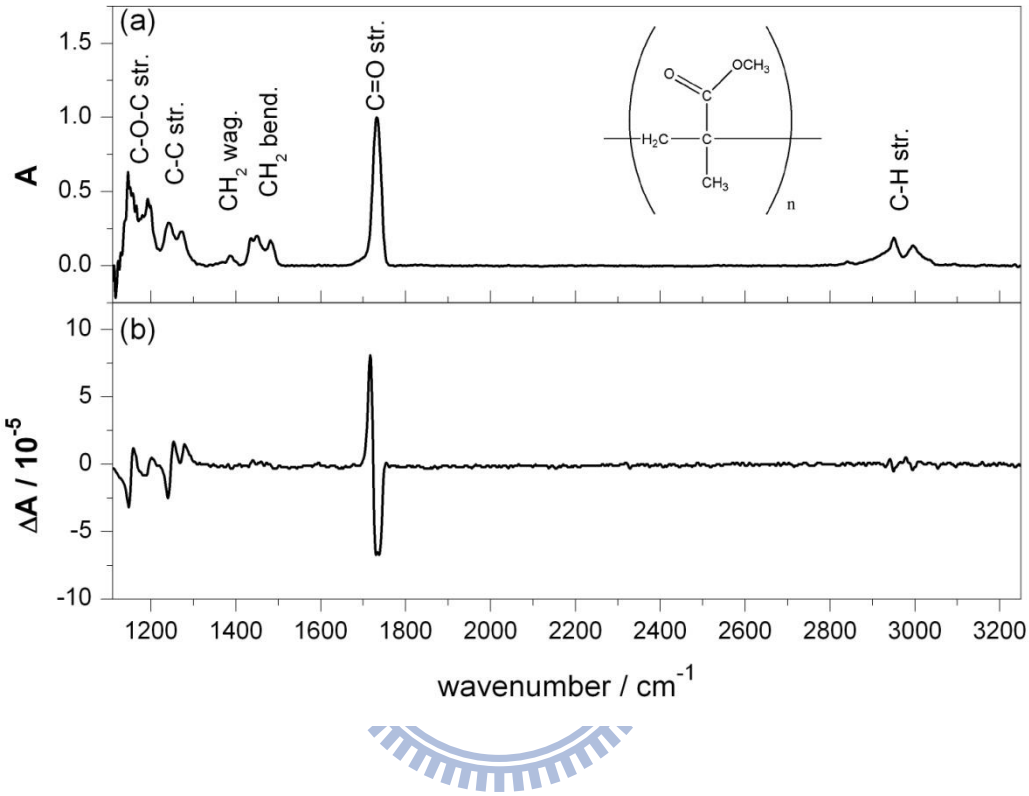


Figure 5-6 (a) IR absorption spectrum and (b) vibrational Stark spectrum of PMMA ($\chi$ = 90°). The applied electric field is 0.875 MV $cm^{-1}$.

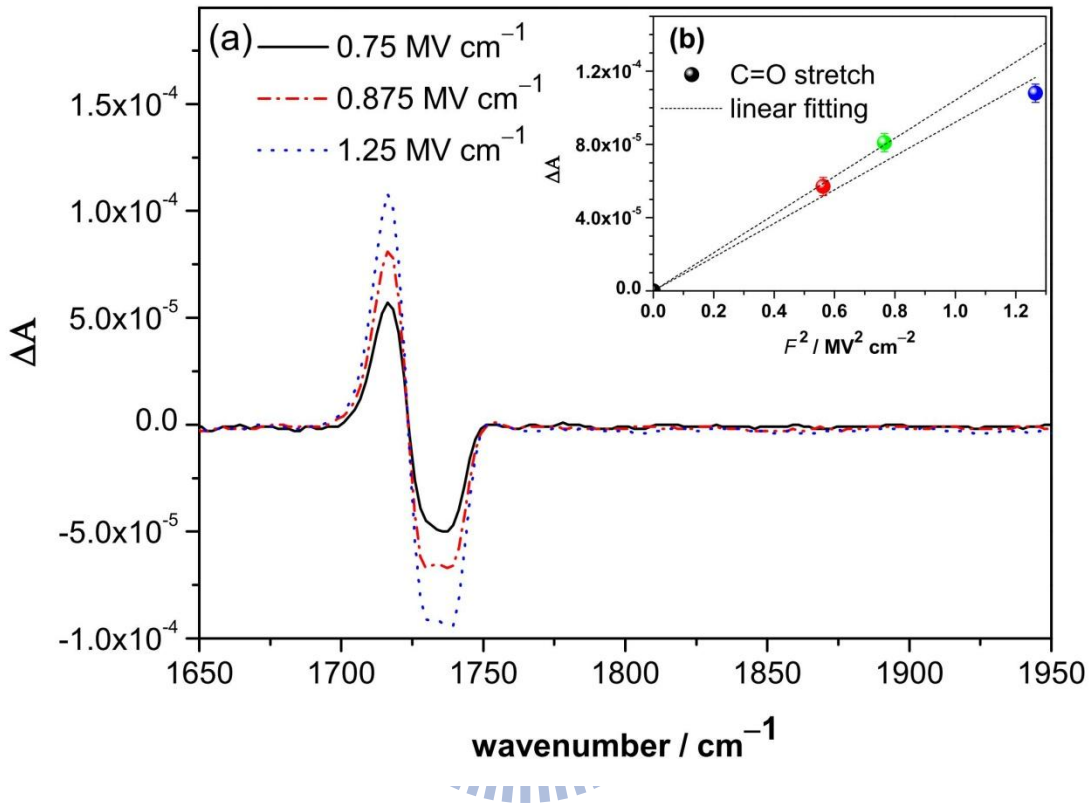


Figure 5-7 (a) Vibrational Stark spectrum of PMMA in the C=O stretching region at three applied fields ($\chi$ = 90°), **F** = 0.75, 0.875, and 1.25 MV cm$^{-1}$. (b) The peak height of Stark signal as a function of the square of the applied electric field.

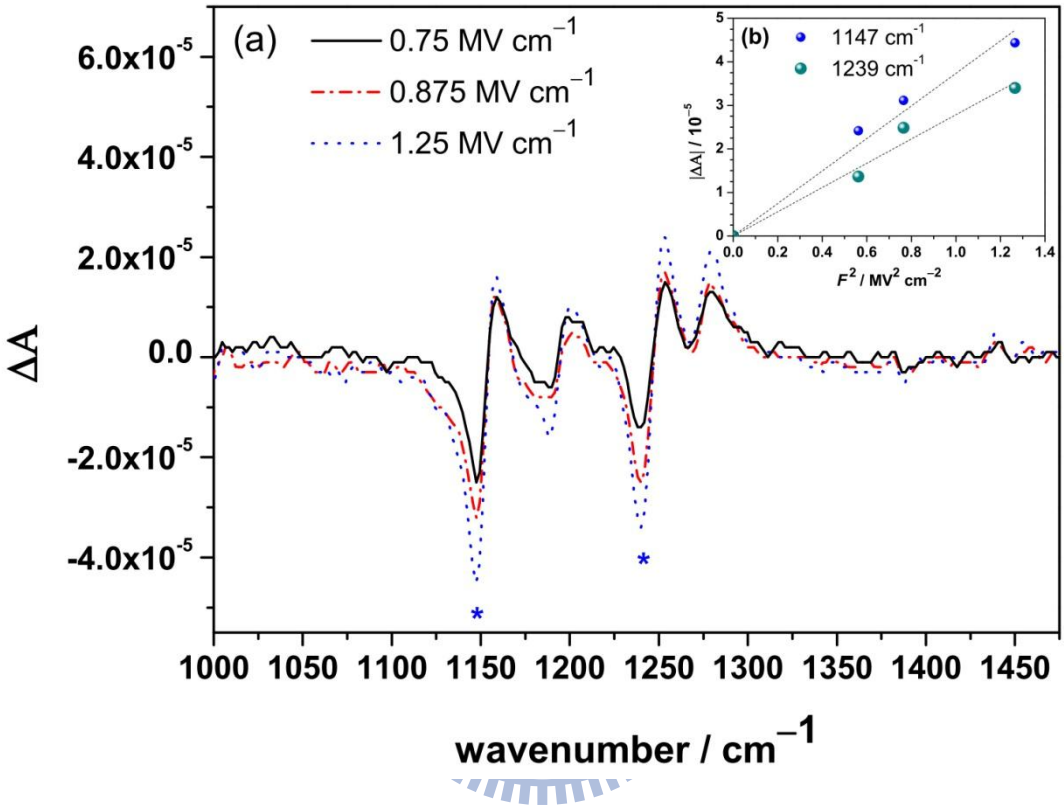


Figure 5-8 (a) Vibrational Stark spectrum of PMMA in the C-O-C and C-C stretching region at three applied field ($\chi$ = 90°), **F** = 0.75, 0.875, and 1.25 MV cm$^{-1}$. (b) The peak height of Stark signals at 1147 and 1239 cm$^{-1}$ (marked * in (a)) as a function of the square of the applied electric field.

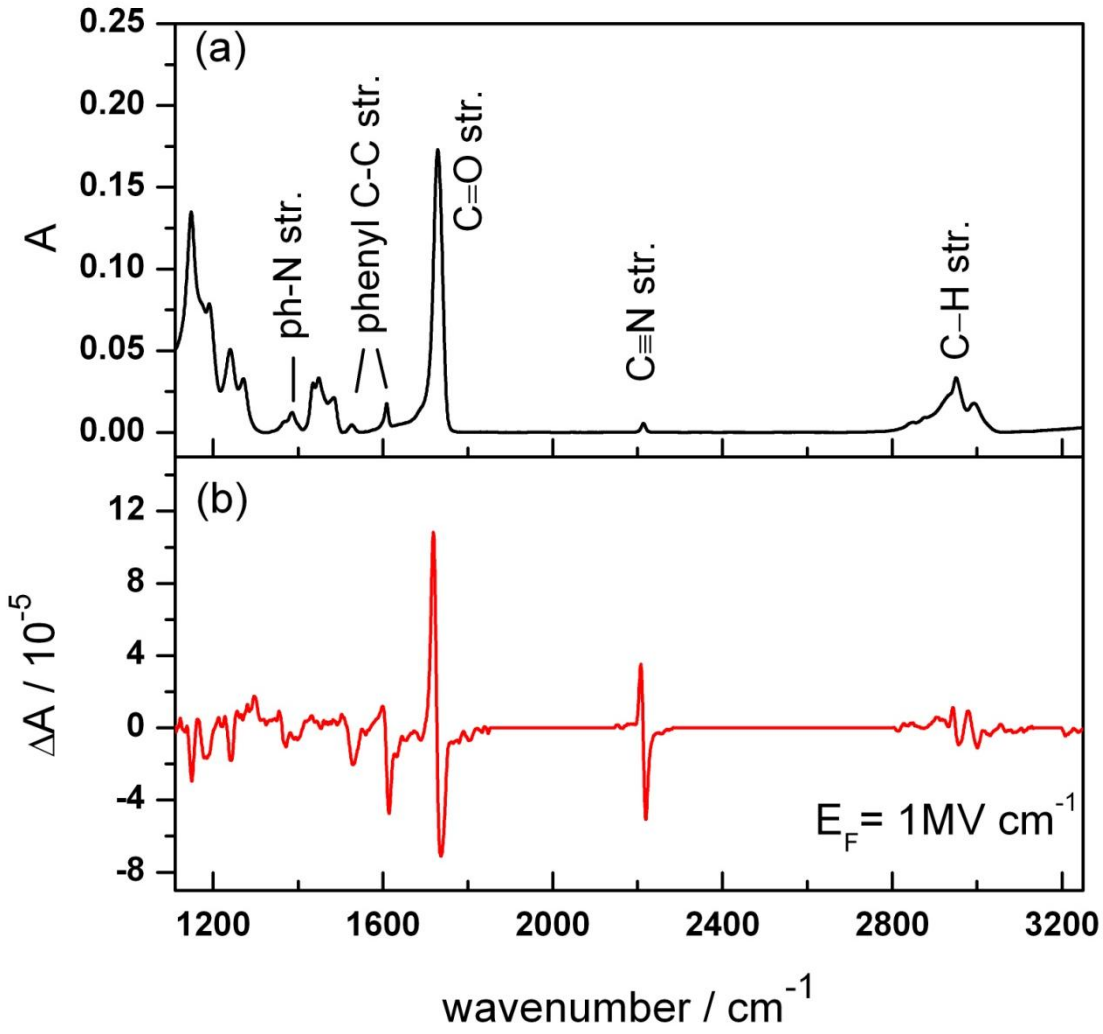


Figure 5-9 (a) IR absorption spectrum and (b) vibrational Stark spectrum of DMABN doped in a PMMA film ($\chi$ = 90°). DMABN:PMMA=1:2. The applied electric field is 1.0 MV $cm^{-1}$.

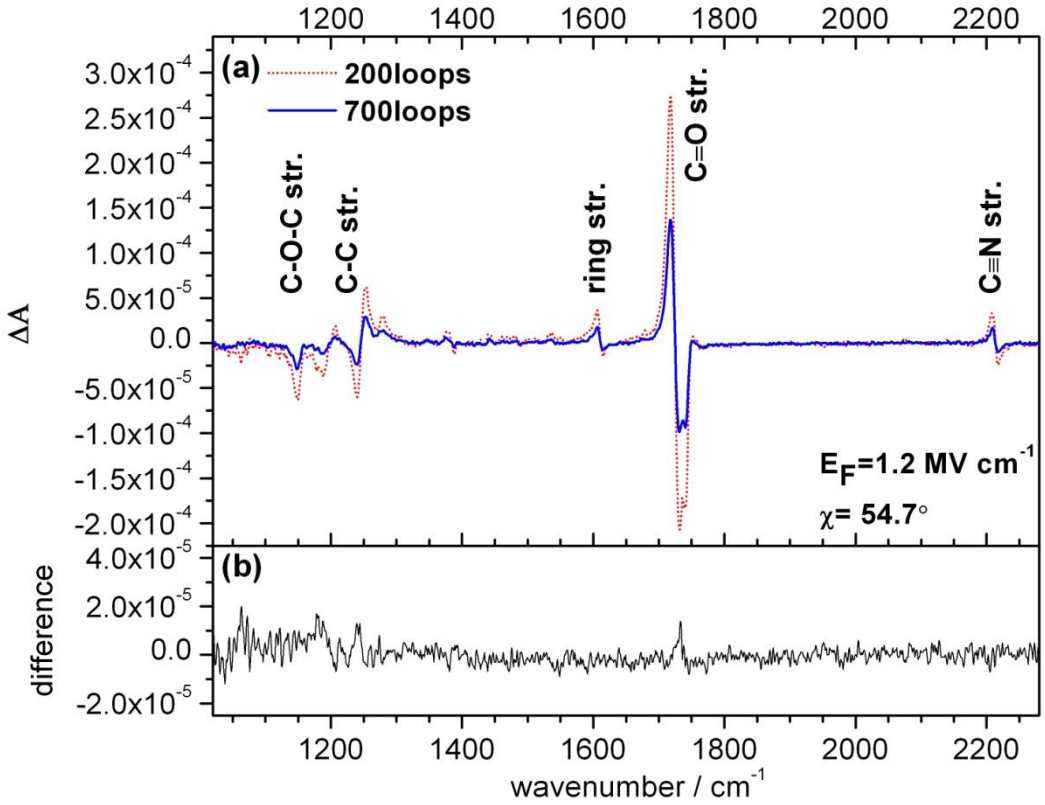


Figure 5-10 (a) Vibrational Stark spectra, under the condition of the magic angle, collected with 200 and 700 loops. The applied electric field is 1.2 MV $cm^{-1}$. (b) The residual spectrum obtained on subtracting the spectrum for 200 loops from the twice spectrum for 700 loops.

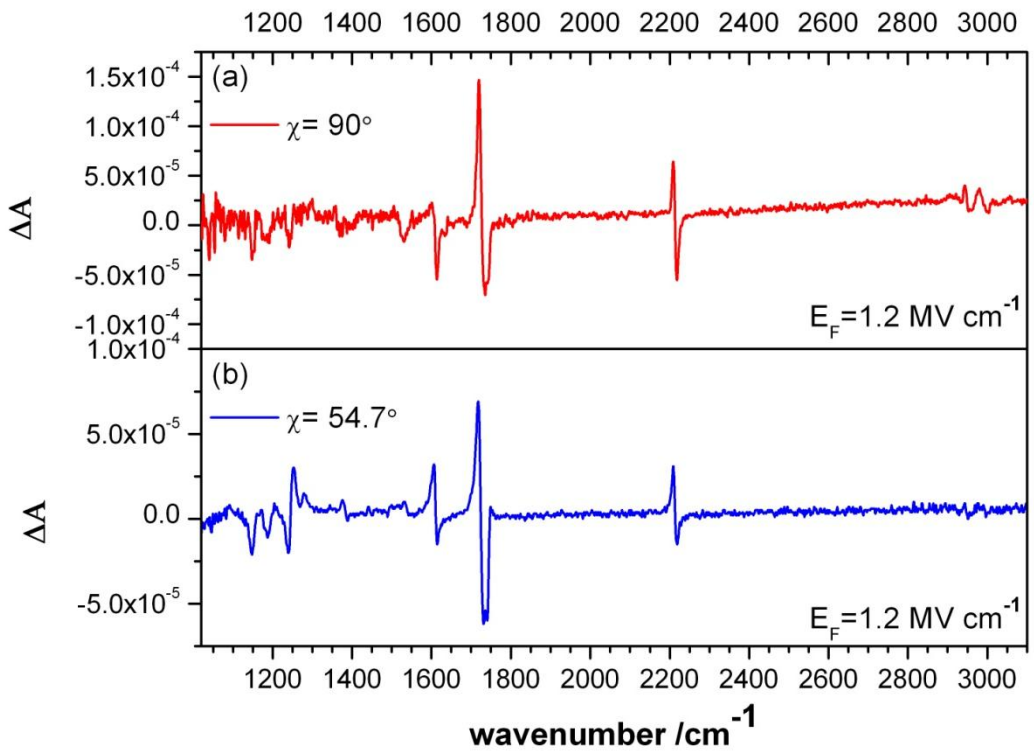


Figure 5-11 Vibrational Stark spectra of DMABN doped in a PMMA film. (a) $\chi$ = 90° and (b) $\chi$ = 54.7°. The applied electric field is 1.2 MV $cm^{-1}$.

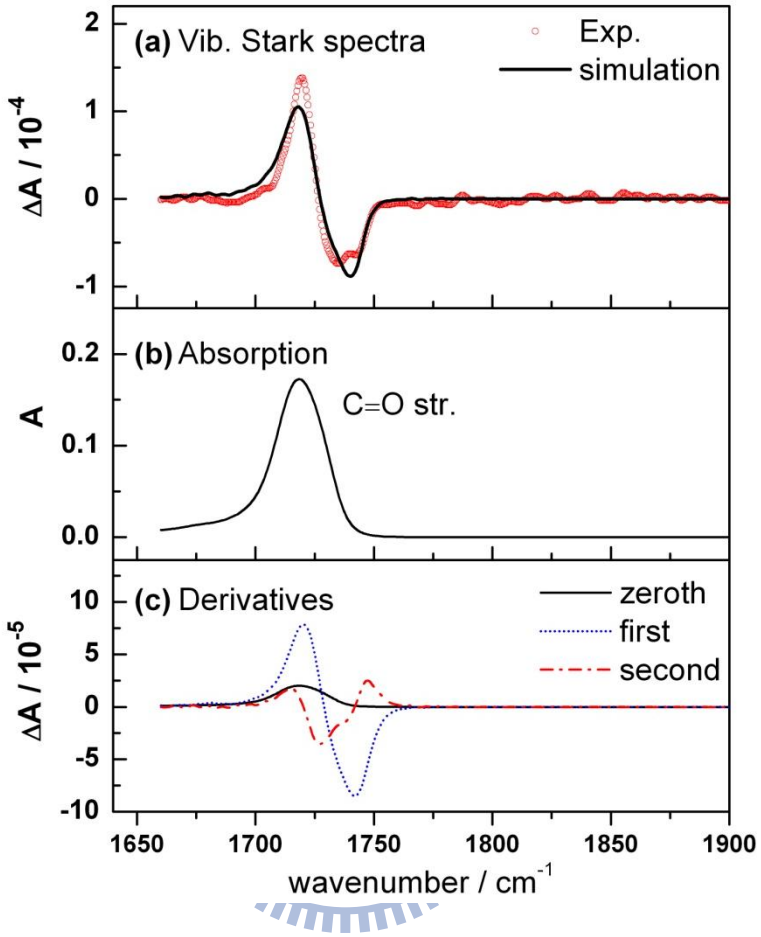


Figure 5-12 (a) Comparison of vibrational Stark spectrum (field on minus field off) and simulated spectrum of PMMA for the C=O stretching mode ($\chi$ = 90°). The applied electric field is 1.0 MV $cm^{-1}$. The red circles represent the data; solid line represents a fit. (b) Absorption spectrum of PMMA. (c) Solid, dot, and dashed dot lines are contributions of the zeroth-, first- and second- derivatives.

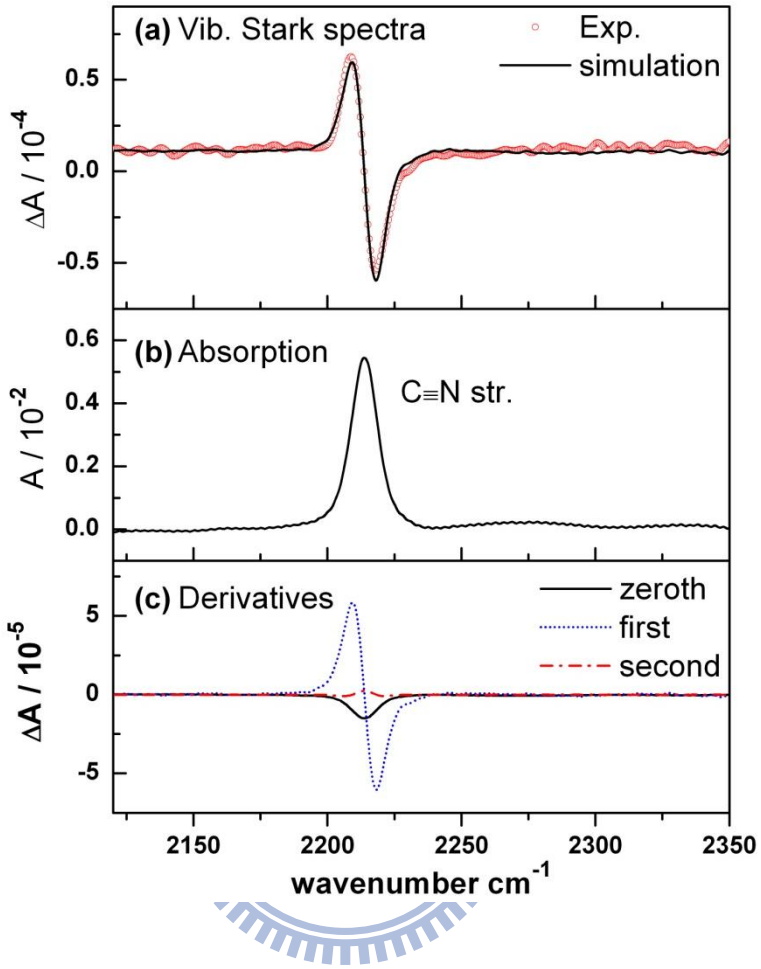


Figure 5-13 (a) Comparison of vibrational Stark spectrum and simulated spectrum of DMABN for the C≡N stretching mode ($\chi$ = 90°). The applied electric field is 1.0 MV $cm^{-1}$. The red circles represent the data; solid line represents a fit. (b) Absorption spectrum of DMABN. (c) Solid, dot, and dashed dot lines are contributions of the zeroth-, first- and second- derivatives.

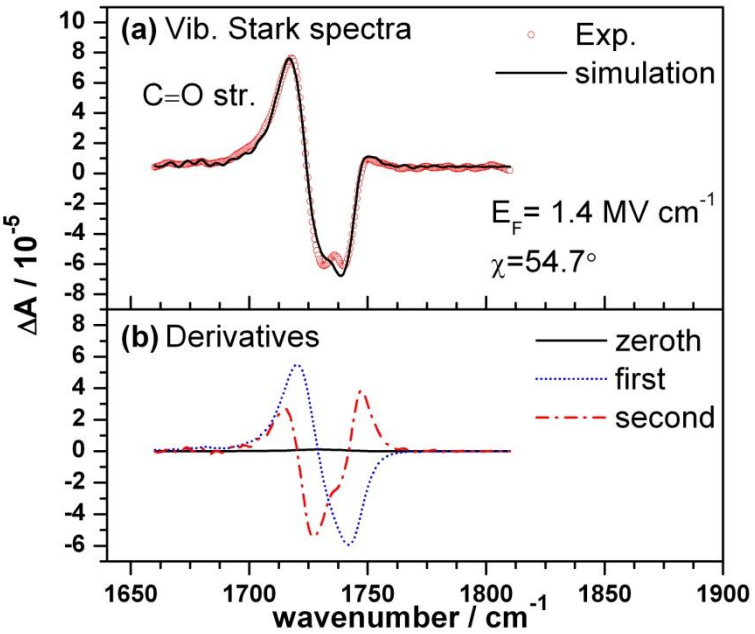


Figure 5-14 (a) Comparison of vibrational Stark spectrum and simulated spectrum of PMMA for the C=O stretching mode ($\chi$ = 54.7°). The applied electric field is 1.4 MV $cm^{-1}$. The red circles represent the data; solid line represents a fit. (b) Absorption spectrum of PMMA. (c) Solid, dot, and dashed dot lines are contributions of the zeroth-, first- and second- derivatives.

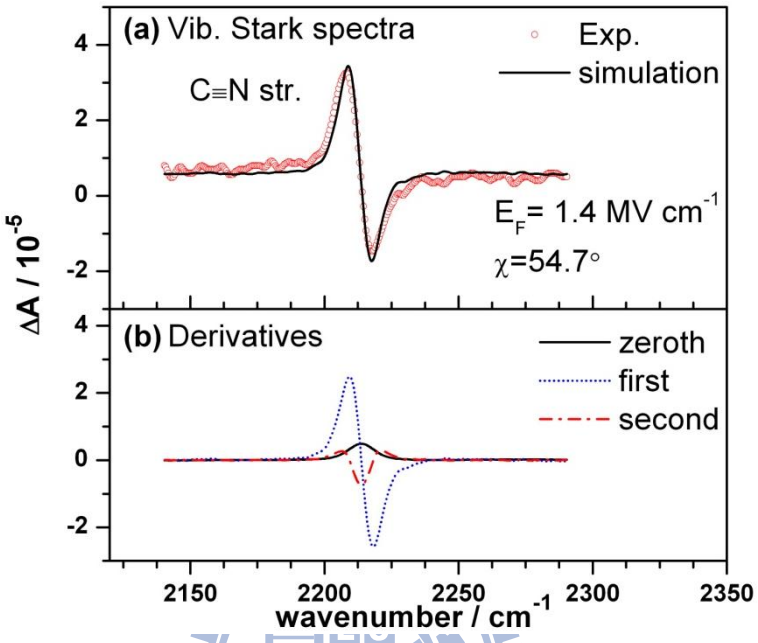


Figure 5-15 (a) Comparison of vibrational Stark spectrum and simulated spectrum of DMABN for the C≡N stretching mode ($\chi$ = 90°). The applied electric field is 1.4 MV cm$^{-1}$. The red circles represent the data; solid line represents a fit. (b) Absorption spectrum of PMMA. (c) Solid, dot, and dashed dot lines are contributions of the zeroth-, first- and second- derivatives.

## References


[1] E. Lippert, Angew. Chem. **73**, 695 (1961).

[2] K. Rotkiewicz, K. H. Grellmann, and Z. R. Grabowski, Chem. Phys. Lett. **19**, 315 (1973).

[3] Z. R. Grabowski and K. Rotkiewicz, Chem. Rev. **103**, 3899 (2003).

[4] S. Techert and K. A. Zachariasse, J. Am. Chem. Soc. **126**, 5593 (2004).

[5] T. Yoshizawa, Y. Iwaki, N. Osaka, T. Nakabayashi, K. A. Zachariasse, and N. Ohta, J. Phys. Chem. B **108**, 19132 (2004)

[6] G. U. Bublitz and S. G. Boxer, Annu. Rev. Phys. Chem. **48**, 213 (1997).

[7] S. S. Andrews and S. G. Boxer, J. Phys. Chem. A **104**, 11853 (2000).

[8] T. Nakabayashi and N. Ohta, Chem. Lett. **34**, 1194 (2005).

[9] N. S. Hush and J. R. Reimers, J. Phys. Chem. **99**, 15798 (1995).

[10] S. S Andrews and S. G. Boxer, J. Phys. Chem. A ***106***, 469 (2002).

[11] E. S. Park, S. S. Andrews, R. B. Hu, and S. G. Boxer, J. Phys. Chem. B **103**, 9813 (1999).

[12] H. Hiramatsu and H. Hamaguchi, Appl. Spectrosc. **58**, 355 (2004).

[13] I-C. Lee, H. Hamaguchi, and S. Shigeto, Chem. Phys. Lett. **466**, 144 (2008).

[14] I. T. Suydam and S. G. Boxer, Biochemistry **42**, 12050 (2003).

[15] I. T. Suydam, C. D. Snow, V. S. Pande, and S. G. Boxer, Science **313**, 200 (2006).

[16] S. S Andrews and S. G. Boxer, Applied Spectroscopy **55**, 1161 (2001).

[17] C. J. F. Böttcher and P. Bordewijk, Theory of Electric Polarization, Vol. 1, Elsevier, Amsterdam (1978).

[18] W. Liptay, in *Excited States*, edited by E. C. Lim (Academic, New York, 1974), Vol. 1, p. 129

[19] The MP100-M Thin Film Thickness Measurement System, Mission Peak Optics, http://www.missionpeakoptics.com/MP1.htm.

[20] S. Ramesh, K. H. Leen, K. Kumutha, and A. K. Arof, Spectrochimica Acta A **66** 1237 (2007).

[21] E. D. Emmons, R. G. Kraus, S. S. Duvvuri, J. S. Thompson, and A. M. Covington, J. Poly. Sci. B **45**, 358 (2007)

[22] O. N. Tretinnikov and K. Ohta, Macromolecules **35**, 7343 (2002).

[23] D. I. Bower and W. F. Maddams, The vibrational spectroscopy of polymers, Cambridge

Solid State Science Series, Cambridge, New York, 1992.

[24] H. Okamoto, J. Phys. Chem. A **104**, 4182 (2000).

[25] M. S. Mehata, T. Iimori, T. Yoshizawa, and N. Ohta, J. Phys. Chem. A **110**, 10985 (2006).

[26] E. Jalviste and N. Ohta, J. Chem. Phys. **121**, 4730 (2004).

[27] A. Chowdhury, S. A. Locknar, L. L. Premvardhan, and L. A. Peteanu, J. Phys. Chem. A **103**, 9614 (1999).

[28] S. S. Andrews and S. G. Boxer, Rev. Sci. Inst. **71**, 3567 (2000).

# Appendix A

For the absorption spectrum did not have overlapping bands, the numerical derivatives of the measured absorption spectrum were used to fit the VSE data, providing separate fit coefficients for each band according to the following equation.

$$\Delta A(\nu) = (fF)^2 \left\{ a' A(\nu) + b' \nu \frac{d[A(\nu(\nu)]}{d\nu} + c' \nu \frac{d^2[A(\nu(\nu)]}{d\nu^2} \right\}$$

We apply the multiple linear regression to study the relationship between the zeroth-, first-, and second- derivatives of absorption spectrum and the VSE spectrum by using a model of the following form. $y = \beta_0 + A_{fit}\, x_1 + B_{fit}\, x_2 + C_{fit}\, x_3$, in which $\beta_0$ is the constant term, $A_{fit}$, $B_{fit}$, and $C_{fit}$ are the fitting coefficients, $y$ is the VSE spectrum $\Delta A(\nu)$, and $x_1 = A(\nu)$, $x_2 = \nu \frac{d[A(\nu(\nu)]}{d\nu}$, $x_3 = \nu \frac{d^2[A(\nu(\nu)]}{d\nu^2}$.

We use Origin program to perform multiple linear regression to obtain the fitting coefficients. Parameters are estimated using a weighted least-square method. Figure A-1 and Figure A-2 show the results of fitting for C=O stretching modes of PMMA and C≡N stretching modes of DMABN at the condition of normal incidence and magic angle.

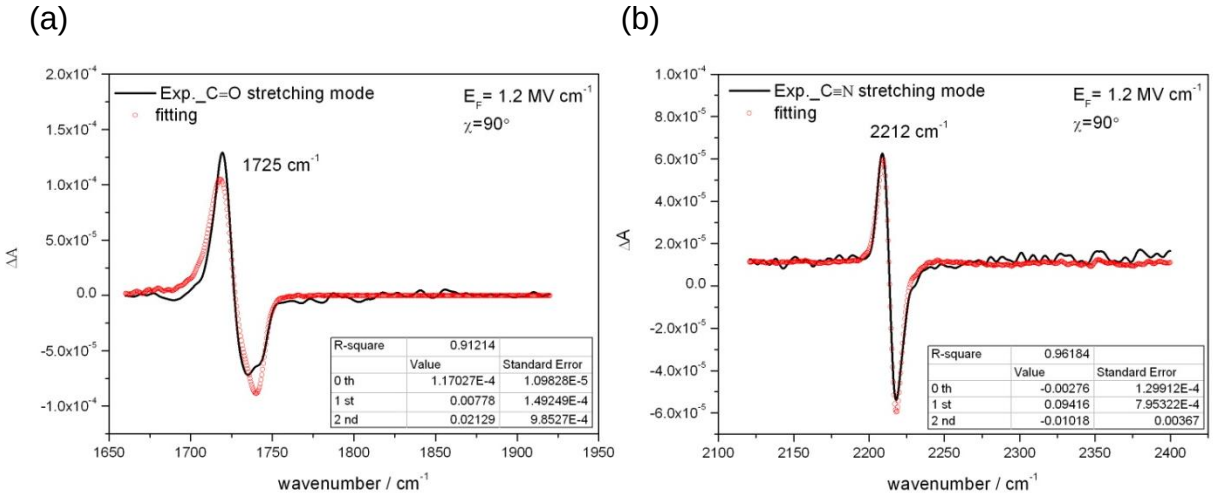


Figure A-1 Comparison of the VSE spectrum and the simulated spectrum of DMABN doped in a PMMA film for the (a) C=O and (b) C≡N stretching modes. (χ = 90°). The applied electric field is 1.2 MV $cm^{-1}$.

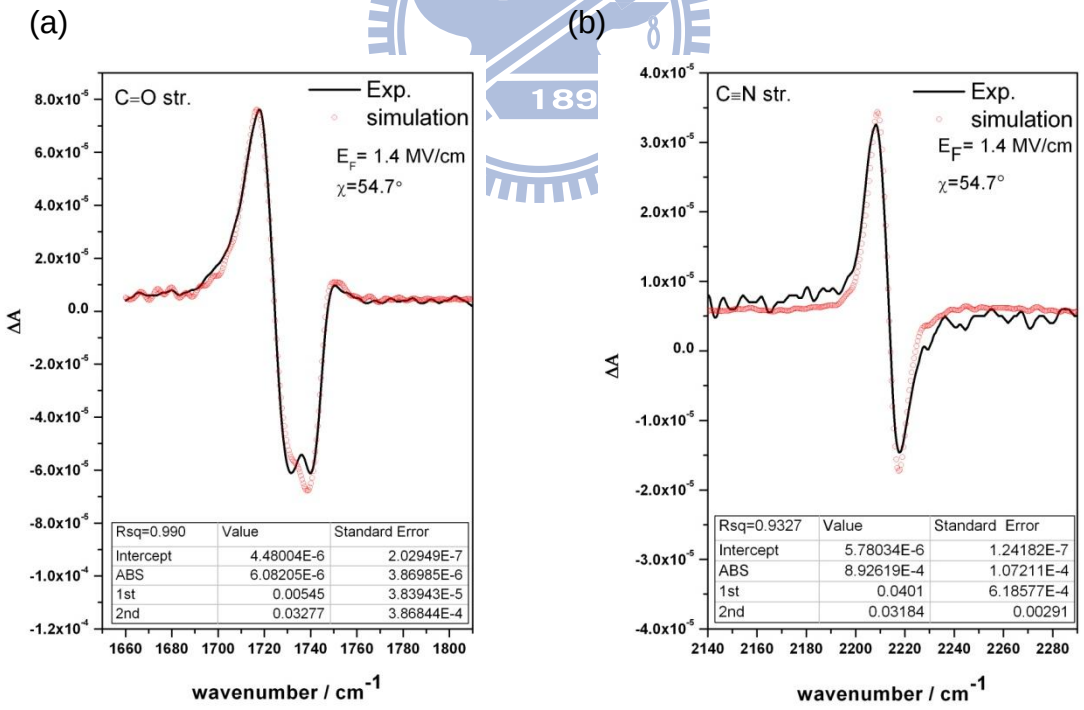


Figure A-2 Comparison of the VSE spectrum and the simulated spectrum of DMABN doped in a PMMA film for the (a) C=O and (b) C≡N stretching modes. (χ = 54.7°). The applied electric field is 1.4 MV $cm^{-1}$.

# Appendix B

## Rapid Scan Method

1. A sequence of timing commands for a rapid scan measurement is given as follows,

```
Start loop 200
    Set output high 1
    Wait 20
    Set output low 1
    Wait 500
    Set output high 3
    Wait 20
    Set output low 3
    Set buffer 2
    Measure 10
    Set output high 3
    Wait 20
    Set output low 3
    Wait 500
    Set output high 3
    Wait 20
    Set output low 3
    Set buffer 3
    Measure 10
    Set output high 3
    Wait 20
    Set output low 3
    Wait 1500
End loop
```

2. The explanation of each command is given in the following table.

| Command | Explanation |
|---|---|
| Start Loop n | The start of a loop. All commands enclosed between the commands Start Loop and End Loop will be repeated n times. |
| End Loop | The end of a loop. |
| Set Output “High“ | This command causes the spectrometer to send a high voltage trigger signal to the external trigger box E525/Z and sets the voltage to +5V at the specific trigger signal line. |
| Set Output “Low“ | This command sets the voltage to 0V at the specific trigger signal line. |
| Wait (ms) | Delays the execution of the subsequent command by the specified period (in milliseconds). |
| Set Buffer | Specifies the memory area that is to be accessed. |
| Measure N Scans | Starts the measurement with N scans. |

3. The external trigger box (E525/Z) with is used as a trigger device for rapid scan experiments.

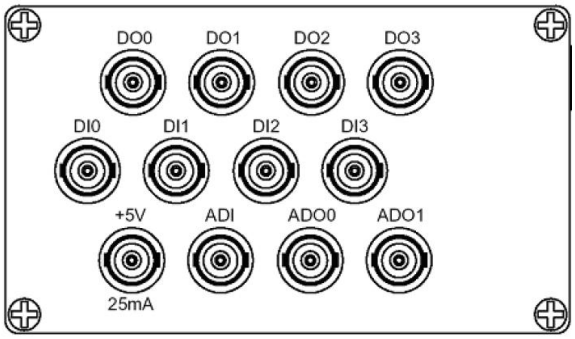


The following table shows the assignments of the trigger signal lines to the BNC connectors at the external trigger box.

| Trigger signal line address | BNC connector at the external trigger box |
|---|---|
| 1 | DO0 |

| | |
|---|---|
| 2 | DO1 |
| 3 | DO2 |
| 4 | DO3 |

4. The timing setting of pulse generator DG 535 is given as follows,

$A = T_0 + 9.5\ S$

$B = A + 9.5\ S$

$C = B + 0\ S$

$D = D + 0.3\ S$

DG 535 was triggered by the output signal from DO0 connector of the E525/Z.

5. The following timing chart shows the timing of output signals from DO0 and DO2 connectors of the E525/Z, of output voltage from DG535 pulse generator, and of FTIR measurements.